Gas Crossover in Polymer Electrolyte Membrane Water Electrolysis:

Experimental Studies on Hydrogen and Oxygen Crossover and Improved Mitigation Strategies

Von der Fakultät für Elektrotechnik und Informatik

der Gottfried Wilhelm Leibniz Universität Hannover

zur Erlangung des akademischen Grades

Doktorin rerum naturalium

(abgekürzt: Dr. rer. nat)

genehmigte Dissertation

von Frau

Agate Martin (geb. Broda), M. Sc.

2022

Danksagung

Die folgende Dissertationsschrift ist das Ergebnis meiner Zeit als wissenschaftliche Mitarbeiterin am Institut für Elektrische Energiesysteme im Fachgebiet Elektrische Energiespeichersysteme an der Leibniz Universität Hannover. Vorweg möchte ich mich bei allen bedanken, die zum Gelingen dieser Arbeit beigetragen haben.

Zuallererst möchte ich mich bei Prof. Dr.-Ing. Richard Hanke-Rauschenbach für die Möglichkeit bedanken, in einem solch zukunftsrelevanten Themengebiet mitarbeiten zu dürfen. Es hat mir viel Freude bereitet, das Fachgebiet in den letzten Jahren wachsen zu sehen und mit so vielen Wasserstoff-Enthusiasten zusammenzuarbeiten.

Großen Dank verdienen Prof. Dr. rer. nat. Nadja Bigall für die Übernahme des Korreferats und Prof. Dr.-Ing. Lutz Hofmann für die Übernahme des Vorsitzes der Prüfungskommission.

Bei Dr.-Ing. Boris Bensmann möchte ich mich besonders für die stetige Betreuung meiner Arbeit, die vielen langen Diskussionen und sein offenes Ohr für Probleme aller Art, bedanken. Vielen Dank für die gewissenhaften Durchsichten meiner Publikationen und dieser Schrift. Bei Dr.-Ing. Patrick Trinke bedanke ich mich ebenfalls für die Begleitung meiner Arbeit in den letzten Jahren. Die Zusammenarbeit mit euch beiden hat maßgeblich zum Erfolg meiner Promotion beigetragen.

Ich bedanke mich darüber hinaus bei Lena Bühre, die mich nicht nur im Labor, sondern auch bei der Vorbereitung von Vorträgen und der Durchsicht meiner Dissertationsschrift unterstützt hat. Natürlich habe ich die restliche Elektrolyse-Gruppe nicht vergessen: Vielen Dank für die fachlichen (und auch weniger fachlichen) Diskussionen und für die gesellige Zusammenarbeit im Labor. Ich hoffe, euch gehen niemals die Ideen für die Benennung der ISE-Zellen aus. Auch bei den verbliebenen Kollegen des Fachgebiets bedanke ich mich für die netten Gespräche in den Kaffeepausen und die vielen lustigen Erinnerungen an die IfES-Traditionen, wie das tägliche Wall Ball Turnier. Ich wünsche euch allen viel Erfolg auf euren Wegen, wo auch immer sie euch hinführen.

Zum Schluss bedanke ich mich herzlichst bei meinen Freunden und meiner Familie für die emotionale Unterstützung in den letzten Jahren. Der allergrößte Dank geht an meinen Mann Denis, der immer sehr geduldig mit mir war, durchweg an mich mich geglaubt hat, mich in Zeiten mit wenig Zuversicht angespornt hat und Erfolge mit mir gefeiert hat.

Danke!

Kurzfassung

Für die Steigerung der Wettbewerbsfähigkeit der Polymerelektrolytmembran-Wasserelektrolyse (PEM-WE) für die nachhaltige Wasserstoffproduktion, müssen diese sicher und effizient betrieben werden und eine hohe Langlebigkeit aufweisen. Der Crossover der Produktgase Wasserstoff und Sauerstoff durch die Membran wirkt sich auf jede dieser Anforderungen aus, weshalb ein ganzheitliches Verständnis dieses Phänomens notwendig ist, um Lösungs- oder Vermeidungsstrategien zu entwickeln. Im Rahmen dieser Arbeit werden der Crossover von Sauerstoff und Wasserstoff experimentell untersucht.

Im ersten Teil der Arbeit wird die Untersuchung von Gestaltungs- und Betriebsparametern auf den Wasserstoff-Crossover vertieft, was insbesondere für den sicheren Betrieb und die Effizienz relevant ist. Dabei stellt sich heraus, dass sich eine starke Zellkomprimierung zwar positiv auf das elektrische Betriebsverhalten auswirkt, jedoch gleichzeitig der Wasserstoffverlust durch Crossover erhöht wird. Dies wird damit erklärt, dass der Übergang von gelösten Wasserstoff in den gasförmigen Zustand mit zunehmender Komprimierung gehemmt wird, wodurch die gelöste Wasserstoffkonzentration zunimmt und schließlich die Triebkraft für den Wasserstoff-Crossover verstärkt wird. Darüber hinaus wird gezeigt, dass sich der funktionelle Zusammenhang zwischen dem Wasserstoff-Crossover und der Stromdichte bei hohen Stromdichten anders verhält, als es aus gängigen Modellansätzen zu erwarten ist.

Im zweiten Teil liegt der Fokus auf der Quantifizierung des Sauerstoff-Crossovers, da dieser Materialdegradation auslöst und somit die Langlebigkeit des Elektrolyseurs verringert. Um die Rekombination von Sauerstoff und Wasserstoff zu vermeiden, werden Platin-freie Katalysatoren an der Kathode eingesetzt. Es wird gezeigt, dass mit rekombinationsträgen Katalysatoren mehr Sauerstoff im Kathodenproduktgas nachgewiesen wird. Allerdings ist dennoch davon auszugehen, dass ein unbekannter Anteil vom permeierten Sauerstoff rekombiniert, wodurch die Quantifizierung des tatsächlichen Sauerstoff-Crossovers nach wie vor eine Herausforderung bleibt.

Der dritte Teil dieser Arbeit beschäftigt sich mit der Gestaltung einer Rekombinationszwischenschicht aus Platin in der Membran, mit welcher der Wasserstoffanteil im Anodengas gezielt reduziert wird und somit die Bildung von explosiven Gasgemischen vermieden wird. Es zeigt sich, dass die Positionierung der Zwischenschicht in der Nähe der Anode, im Vergleich zu Zwischenschichten in der Membranmitte oder nahe der Kathode, die stärkste Reduktion des Wasserstoffgehalts zufolge hat. Dies wird damit begründet, dass die verfügbare Menge an Sauerstoff an der Zwischenschicht für die Rekombinationsreaktion von der Anode in Richtung Kathode abnimmt.

Schlagworte: Polymerelektrolytmembran-Wasserelektrolyse, Wasserstoff-Crossover, Sauerstoff-Crossover, Sicherheitsproblematik, Effizienz, Langlebigkeit, Mitigationsstrategie

Abstract

To increase the competitiveness of polymer electrolyte membrane water electrolysis (PEM-WE) for the sustainable hydrogen production, the electrolyzers must be operated safely, efficiently, and need a long durability. The gas crossover of the product gases hydrogen and oxygen through the membrane affects all three requirements, which is why a thorough understanding of this phenomenon is necessary to develop solution or mitigation strategies. In this thesis, the crossover of oxygen and hydrogen is experimentally investigated.

In the first part of this work, the investigation of design and operating parameters for the hydrogen crossover is consolidated, which is particularly relevant in terms of the safe and efficient operation. It is shown that a strong cell compression has a positive effect on the polarisation behaviour, but at the same time the hydrogen loss through crossover is increased. This is explained by the fact that the transfer of the dissolved hydrogen into the gaseous state is limited with increased compression, leading to higher dissolved hydrogen concentrations and hence to a higher driving force for hydrogen crossover. In addition, it is shown that the functional relationship between the hydrogen crossover and the current density behaves differently at high current densities than expected from commonly used model approaches.

In the second part, the focus is on the quantification of the oxygen crossover, as this triggers the material degradation and reduces the durability of the PEM electrolyzer. In order to avoid the recombination of oxygen and hydrogen, platinum-free catalysts are used at the cathode. It is shown that with less reactive catalysts, more oxygen is detected in the cathode product gas. However, it still has to be assumed that an unknown portion of the permeated oxygen recombines with hydrogen, which means that quantifying the actual oxygen crossover remains challenging.

The third part of this thesis deals with the design of a platinum recombination interlayer in the membrane, with which the hydrogen content in the anode gas stream is purposefully reduced to avoid the formation of explosive gas mixtures. It is found that the positioning of the interlayer near the anode results in a better reduction of the hydrogen content compared to interlayers in the middle of the membrane or near the cathode. This is explained with the available amount of oxygen at the interlayer, decreasing from the anode towards the cathode.

Keywords: polymer electrolyte membrane water electrolysis, hydrogen crossover, oxygen crossover, safety issue, efficiency, durability, mitigation strategy

Contents

Contents

List of Abbreviations and Symbols

The following abbreviations and symbols are used within the written parts of this work. Other abbreviations and symbols may appear in the reprinted journal articles.

Abbreviations

AEM-WE	anion exchange membrane water electrolysis
AWE	alkaline water electrolysis
CCM	catalyst coated membrane
CCS	carbon capture and storage
CL	catalyst layer
EIS	electrochemical impedance spectroscopy
HER	hydrogen evolution reaction
LEL	lower explosion limit
MPL	microporous layer
OER	oxygen evolution reaction
ORR	oxygen reduction reaction
PEM-WE	proton exchange membrane water electrolysis / polymer electrolyte membrane water electrolysis
PFSA	perfluorosulfonic acid
PGM	platinum group metal
PTE	porous transport electrode
PTFE	polytetrafluoro ethylene
PTL	porous transport layer
SEM	scanning electron microscopy
SOEL	solid oxide electrolysis

Symbols

Latin Symbols

a_z	activity of a dissolved species z
c	concentration
c_{gas}	dissolved gas concentration
$D_{H_2}^{eff}$	effective hydrogen diffusion coefficient through Nafion™
F	Faraday's constant, $96\,485\,\mathrm{A\,s\,mol^{-1}}$
G_{H_2}	specific hydrogen flux
i	current density
i_0^{ref}	exchange current density
M_{H_2}	molar mass of hydrogen, $2\,\mathrm{g\,mol^{-1}}$
N_{out}^a	anode flux at outlet
N_{out}^c	cathode flux at outlet
$N_{H_2}^{cross}$	hydrogen crossover flux
$N_{O_2}^{cross}$	oxygen crossover flux
$N_{H_2}^{diff}$	diffusive hydrogen crossover flux
$N_{H_2}^{drag}$	dragged hydrogen crossover flux
$N_{H_2}^{evo}$	evolved hydrogen flux
$N_{O_2}^{evo}$	evolved oxygen flux
$N_{H_2}^{hyd}$	hydraulic hydrogen crossover flux
$N_{H_2}^{recomb}$	recombined hydrogen flux
$N_{O_2}^{recomb}$	recombined oxygen flux
n	number of transferred electrons
n_{drag}	number of dragged water molecules per proton
P_{H_2}	hydrogen permeability of Nafion™
P_{H_2O}	hydraulic permeability of Nafion™
p	pressure
p^x	pressure at the cathode ($x = \mathrm{c}$) or anode ($x = \mathrm{a}$)
p_{gas}^x	partial pressure of a gas (hydrogen or oxygen) at the cathode ($x = \mathrm{c}$) or anode ($x = \mathrm{a}$)
$p_{H_2O}^{sat}$	saturated vapour pressure of water
R	ideal gas constant, $8.3145\,\mathrm{J\,mol^{-1}\,K^{-1}}$

R_{HF}	high frequency resistance
R_{Ω}	ohmic resistance
S_{gas}	gas solubility
T	temperature
U_{cell}	cell voltage
$U_{\text{cell}}^{\text{rev}}$	reversible cell voltage
$U_{\text{cell}}^{\text{rev},\circ}$	standard reversible cell voltage
$w_{\text{H}_2}^{\text{spec}}$	specific energy demand

Greek Symbols

α	charge-transfer coefficient
$\Delta^{\text{R}}G^{\circ}$	standard reaction free enthalpy
δ_{mem}	membrane thickness
η_{faraday}	faradaic efficiency
η_{kin}	kinetic overpotential
η_{mtx}	mass transport and other overpotentials
η_{Ω}	ohmic overpotential
$\mu_{\text{H}_2\text{O}}$	dynamic viscosity of water
$v_{\text{H}_2\text{O}}^{\text{drag}}$	velocity of dragged water
$v_{\text{H}_2\text{O}}^{\text{hyd}}$	velocity of hydraulic transported water
$\phi_{\text{H}_2}^{\text{a}}$	hydrogen in oxygen content in anode product gas
$\phi_{\text{O}_2}^{\text{c}}$	oxygen in hydrogen content in cathode product gas

1 Introduction

Hydrogen plays an indispensable role in sustainable future energy scenarios.[1–3] Just like many fossil energy carriers, hydrogen can be easily stored and transported in gaseous or liquid form, making it an attractive and climate-friendly alternative for the use in the energy and mobility sector.[4–6] Besides deploying it as an energy carrier, hydrogen is also an important raw material for the chemical industry (e. g. production of ammonia and other basic chemicals, hydrogenation of hydrocarbons [2, 7, 8]) and the defossilisation of the heavy duty industry (e. g. steel production [2, 7]).

Although hydrogen is one of the most common elements on earth, it occurs almost exclusively in bound form and barely in molecular state.[3, 4] In order to make hydrogen usable for energy storage, it has to be converted from the bound into the molecular state. Depending on the method, the primary energy source, and how potential carbon emissions are handled, a corresponding colour is assigned to the hydrogen.[9, 10] The resulting hydrogen rainbow, shown in fig. 1.1, gives a brief overview of the most common and promising processes for hydrogen production.
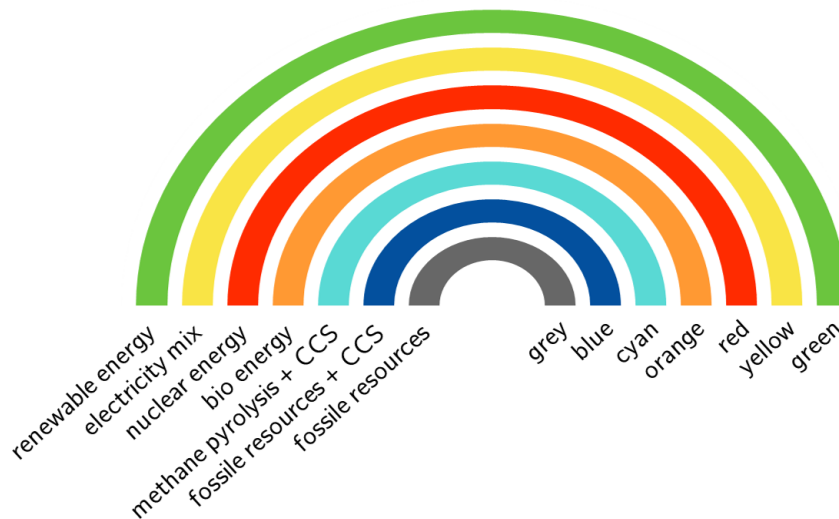

Figure 1.1: The hydrogen rainbow. Based on the primary energy source and how carbon emissions are handled (left side of rainbow), the produced hydrogen is assigned to a specific colour (right side of rainbow). Hydrogen produced by chemical conversion is either grey, blue, cyan or orange. The electrochemical conversion of water results in either red, yellow or green hydrogen. Moreover, there are other, rarely used production processes (such as plasmalysis) which are not considered here.

One option to produce hydrogen is the chemical conversion of hydrocarbons or water with carbon-based energy carriers. Hydrogen obtained by steam reforming with carbon emission into the atmosphere is referred to as black or grey hydrogen.[9, 11–13] Although this method is still widely used, it should be replaced by more sustainable methods in future. One possible approach is the capture and storage of produced carbon emissions (carbon capture and storage, CCS). Then, hydrogen obtained by steam reforming is referred to as blue hydrogen or by pyrolysis as cyan hydrogen.[9–13] Another, more sustainable possibility is the usage of biomass as a renewable carbon source, leading to orange hydrogen.[9, 14]

Moreover, hydrogen can be produced by the electrochemical conversion of water with electrolysis, where the origin of the electrical power is crucial for the classification. When electrolysis is performed with electricity from nuclear energy or from mixed origin (e. g. partially from coal power stations), the resulting hydrogen is red[9, 14] or respectively yellow[10, 12]. With electricity from completely renewable resources, the so-called green hydrogen is produced.[9, 11–14]

From all these proposed methods, using renewable energy for the electrolysis of water is the most promising and sustainable way to produce green hydrogen for the energy sector and other applications.[5, 15] Currently, there are four different technologies for electrolysis, which essentially differ in the type of electrolyte used. The technologies are briefly presented here for the sake of completeness, but only one is examined in more detail in this work.

The alkaline water electrolysis (AWE) is a mature and established technology.[8, 15–18] Although alkaline water electrolyzers are relatively cheap and free of precious metals, their operation is limited to low power densities.[8, 15–18] Another promising technology is the acidic electrolysis of water, in which a proton conductive membrane is used as the electrolyte. This technology is usually referred to as polymer electrolyte membrane or proton exchange membrane water electrolysis (PEM-WE). Compared to AWE, PEM-WE allows the dynamic operation at higher current densities and at differential pressures.[15, 17–19] In the last couple of years, the anion exchange membrane water electrolysis (AEM-WE) emerged as another promising candidate for the electrolytic hydrogen production, combining the advantages of the alkaline and acidic technology.[20, 21] However, the technology and the associated material design are still in an early phase of research and development.[13, 20, 21] The fourth technology uses a solid oxide as an electrolyte (solid oxide electrolysis, SOEL) and requires high temperatures of several hundred degrees.[16, 17] The high process temperatures can be provided by waste heat of other industrial processes, reducing the necessary electrical energy input.[16, 17]

This work is dedicated to an issue that particularly affects the further development of PEM water electrolyzers. One central issue to focus on, besides many others, is the so-called gas crossover. In order to reach a high market penetration for PEM-WE, the technology must be able to be operated safely and at a high level of efficiency, and it must

be durable.[22] Gas crossover is affecting all of these objectives, which is why a thorough understanding of this effect is highly important.

The present work is structured as follows. First, the fundamentals on PEM-WE and gas crossover are set in chapter 2. Then, research questions to be adressed within this work are derived in chapter 3. Chapters 4 to 6 contain a summary of the experimental results and discussion, which were also published in scientific journals. Finally, in chapter 7, the research questions are revisited and answered in relation to the earlier presented findings.

2 Fundamentals on PEM Water Electrolysis and Gas Crossover

This chapter gives the background and necessary concepts to follow the subsequently presented experimental studies, which arose during this work. From an engineering perspective, systems are typically evaluated based on their electrical, thermal and mass transport behaviours. To evaluate them, the standards of the PEM-WE technology, including the working principle and typical materials, are covered first in section 2.1. Then, the individual contributions to the overall electrical performance and its characterisation are discussed. In the second part of this chapter, an overview on the mass transport behaviour in PEM-WE cells, considering the current state of knowledge on gas crossover, is given in section 2.2. In the context of this work, the thermal behaviour of the PEM-WE cell is not relevant, which is why it is not considered further.

2.1 PEM Water Electrolysis: State of the Art

Water electrolysis refers to the splitting of water into molecular hydrogen and oxygen by using electrical energy. The general chemical equation is

$$H_2O \rightarrow H_2 + \tfrac{1}{2}O_2 \ .$$
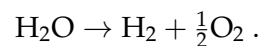
For PEM-WE, a setup consisting of several compact layers has been established. The commonly used materials and their role are outlined in the following, including the chemical and physical characteristics of the cell setup. Subsequently, the characterisation of the electrical performance with polarisation curves is explained.

2.1.1 Working Principle and Key Components

This section starts with a brief overview on the cell setup of a typical PEM-WE cell. Then, the basic requirements and properties of the key components are discussed.

The general cell setup, as sketched in fig. 2.1, contains multiple components for fluid and charge transport. In the center of the cell, a proton conducting membrane serves as the electrolyte and separates both half cells. Catalyst layers (CL) are situated on both sides of the membrane. The following half cell reactions for the oxygen and hydrogen evolution take place inside the catalyst layers:

$$\text{anode:} \qquad H_2O \rightarrow \tfrac{1}{2}O_2 + 2H^+ + 2e^-$$

$$\text{cathode:} \qquad 2H^+ + 2e^- \rightarrow H_2$$
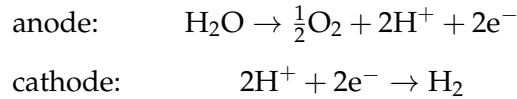
The membrane and CLs are sandwiched between porous transport layers (PTL). Assemblies, in which the CLs are coated directly on the membrane, are called catalyst coated membranes (CCM). Alternatively, the CLs can be coated on the PTLs, which are then called porous transport electrodes (PTE). As the name suggests, the PTLs transport the reactants to and from the CL. Moreover, they ensure the electrical connection to the flow fields. Water and electricity are typically supplied through the flow fields that are embedded in the endplates of the cell. The product gases are removed through the flow fields as well.
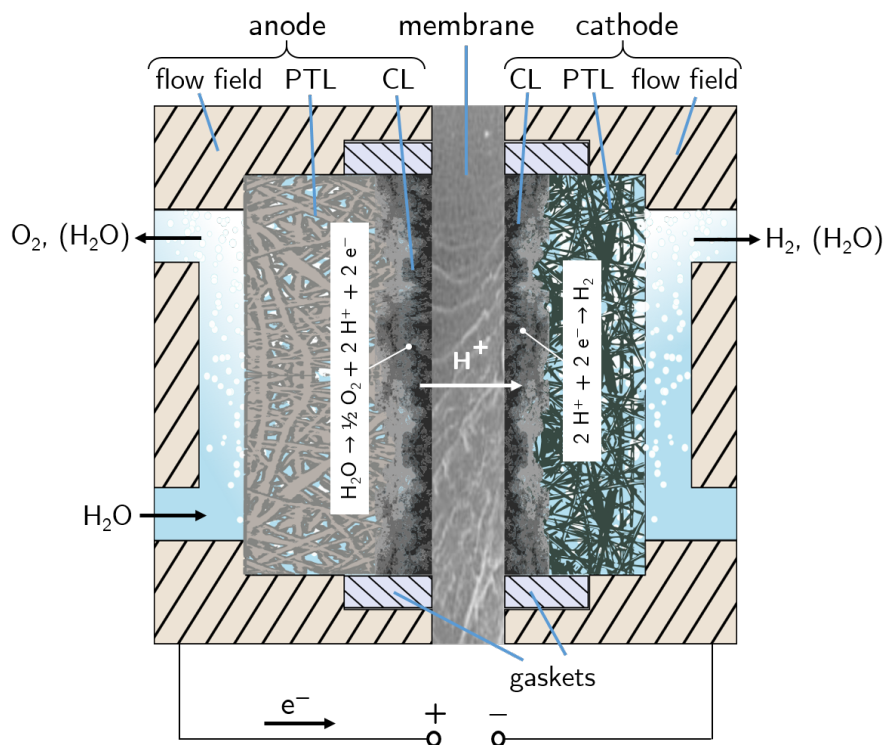

Figure 2.1: Sketch of a typical cell used for PEM-WE. Basic components, mass and charge fluxes are indicated in addition to the half cell reactions. The figure is adapted from Ref. [23].

Membrane A polymer electrolyte membrane serves various purposes in the cell, therefore it requires certain properties. The main tasks of the PEM are to electrically insulate the two electrodes, to enable proton transport and to spacially separate hydrogen and oxygen to prevent mixing. In order to fulfill these tasks, the used material should have a high electrical resistance, a high protonic conductivity and a low gas permeability, respectively.

The named requirements are satisfactorily met by Nafion™, which is the best known representative of the material group of perfluorosulfonic acids (PFSA). In addition, there

are many other material groups (e. g. hydrocarbons), which are described and reviewed in Ref. [24–26].

The characteristic feature of Nafion™ and other PFSAs is a hydrophobic backbone based on polytetrafluoro ethylene (PTFE) and a hydrophilic side chain with sulfonic acid groups.[27] This combination is the reason why PFSAs are often referred to as "ionomer" (ionic polymer). The strong C-F bonds in the backbone and side chain make the material chemically and mechanically stable.[16, 28–30] When the material is wetted, the hydrophobic and hydrophilic phases are separated and form water containing channels.[31, 32] In these channels, the proton transport either takes place on the sulfonic acid groups or in the aqueous phase via the Grotthus mechanism or the vehicle mechanism.[33–35]

Nafion™ membranes are commercially available in different thicknesses (25 µm (NR-211), 51 µm (NR-212), 127 µm (N115), 183 µm (N117), 254 µm (N1110) [36, 37]). For electrochemical applications, such as PEM-WE, the trend goes towards thinner membranes, as this reduces the resistance for proton transport. However, thinner membranes are more prone to electrical shorts and are a minor barrier for gas permeability.[28]

Catalyst Layers   In the catalyst layers, the mass transport towards the electrochemically active catalyst particles takes place. Typically, catalyst layers have a thickness between 10 µm to 30 µm and consist of a porous network made of the ionomer and catalyst particles.[30] The ionomer, usually Nafion™, is required to ensure a sufficient proton conductivity towards the catalyst particles. The electrochemical reaction happens at the triple phase boundary between the ionomer, the catalyst particle and the pore space.[38] In the following, the state of the art catalyst materials for PEM-WE are covered briefly. Recent research progresses and challenges in catalyst development are discussed in Ref. [39–44]. An overview of the possible reaction mechanisms for the electrochemical evolution of hydrogen and oxygen can be found in Ref. [45–47].

In the cathode CL, platinum is used for the hydrogen evolution reaction (HER).[8, 16, 22, 30] Usually, the platinum particles are deposited on activated carbon for increasing the surface area and to reduce the loading.[15, 30, 39] The current platinum loading of around $1\,\mathrm{mg\,cm^{-2}}$ to $2\,\mathrm{mg\,cm^{-2}}$ is expected to decrease in future.[1, 48]

In the anode CL, only few materials are suitable for the oxygen evolution reaction (OER), as they have to withstand the harsh electrochemical environment caused by the acidity of the membrane and the high potentials.[15, 16] For now, oxides of ruthenium and iridium are the best-known electrocatalysts for the OER.[16, 22, 48, 49] Although ruthenium and its oxides show better reaction kinetics, it is prone to dissolution.[16] Iridium and its oxides are more stable during the harsh conditions of the OER, which is why it is widely used in commercial applications.[8, 22, 30] Similar to the cathode catalyst, the typical iridium loading of about $1\,\mathrm{mg\,cm^{-2}}$ to $3\,\mathrm{mg\,cm^{-2}}$ is expected to decrease in future.[2, 15, 48]

Porous Transport Layers   The CCM is sandwiched between two porous transport layers, which provide mechanical support for the the CCM. Moreover, they are designed to

transport reactants towards the catalyst layers and to enable the conduction of heat and electrical currents.[15, 16, 19, 22, 30, 50] Below, the most commonly used materials are introduced briefly. The impact of selected PTL properties such as the thickness[51], the porosity[52, 53] and other aspects[54, 55] are investigated in the named references.

On the cathode side, porous carbon papers with thicknesses between 100 µm to 500 µm are typically used.[15, 22] Carbon PTLs may be coated with a microporous layer (MPL) or may be treated hydrophobically. The MPL can lower the interfacial resistances by increasing the interface between the cathode CL and PTL.[1] The hydrophobic treatment of the PTL with PTFE is expected to improve fluid transport.[1, 54]

On the anode side, carbon is not a suitable material for the PTL, as it would oxidize at the high potentials.[15, 22, 50] Therefore, PTLs on the anode side are typically made of sintered titanium fibers or particles and their thicknesses range between 0.2 mm to 1 mm.[55, 56] Although titanium is a quite corrosion resistant metal, it will oxidize after long operation, which will increase its electrical resistance. For this reason, titanium based PTLs are sometimes coated with iridium or platinum, which are less prone to oxidization.[57, 58]

Flow Fields   The main purposes of the flow fields in a PEM-WE cell are the uniform supply and removal of reactants and the electrical connection to the PTLs.[22, 59] The flow fields have a certain pattern of lands and channels (e. g. straight and parallel channels or serpentine-like structures), to meet the requirements for fluid transport.[59–61] Moreover, they are critical components for the homogeneous distribution of the externally applied clamping pressure and provide room for gasketing to ensure gas and water tightness.[62] Therefore, the flow fields are usually made of high strength materials that are also highly conductive.

In addition to ensure the electrical and fluid supply of the cell, the flow field must also withstand the chemical environment, which limits the choice of material. Currently, titanium is commonly used, because it fulfills all the named requirements. However, titanium flow fields oxidize just as titanium PTLs over time. Again, this can be prevented by coating the flow fields with noble metals.[16, 30]

2.1.2 Electrical Performance and its Characterisation

In the previous section, common materials and components of a PEM-WE cell were introduced. After assembling the components in the cell, the assessment of the electrical performance is usually the next step. For this, a powerful method is the measurement of the current-voltage relationship, resulting in a so-called polarisation curve.[63] The various overpotentials contributing to the polarisation curve and their characterisation are discussed below.

A typical polarisation curve, as shown in fig. 2.2, is obtained by measuring the integral cell voltage response of a PEM-WE cell as the current density is varied or vice versa. Usually, the cell voltage increases monotonically with the current density, because the individual overpotentials contributing to the integral cell voltage, increase with current density as well. Equation 2.1 represents the measured cell voltage U_{cell} as the sum of the reversible cell voltage $U_{\text{cell}}^{\text{rev}}$ (also known as Nernst potential), the ohmic overpotential η_Ω, the kinetic overpotential η_{kin} and remaining overpotentials η_{mtx} caused by mass transport and other processes.[30, 60, 64] For an efficient PEM-WE system, a low cell voltage is desired and can be obtained by minimizing the overpotentials. The indicated cell voltage contributions are discussed in the following.

$$U_{\text{cell}} = U_{\text{cell}}^{\text{rev}} + \eta_\Omega + \eta_{\text{kin}} + \eta_{\text{mtx}} \tag{2.1}$$
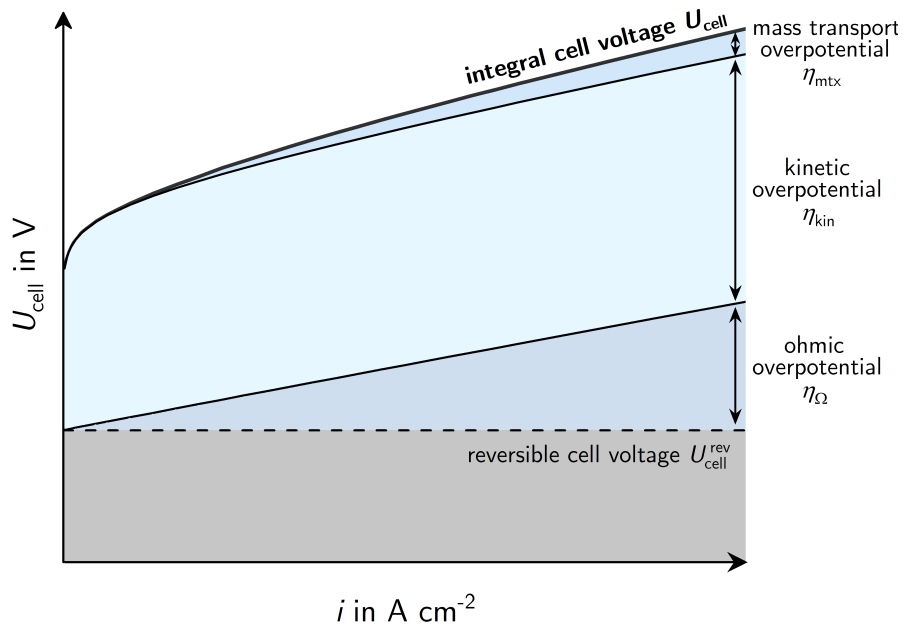

Figure 2.2: A typical polarisation curve with the individual overpotentials according to eq. 2.1.

Reversible Cell Voltage   The reversible cell voltage $U_{\text{cell}}^{\text{rev}}$ is a basic value at open circuit. It is calculated from the known operating conditions according to the Nernst equation for the net water splitting reaction as described by eq. 2.2.[48, 50, 64]

$$
\begin{aligned}
U_{\text{cell}}^{\text{rev}}(T, p) &= U_{\text{cell}}^{\text{rev},\circ}(T) + \frac{\text{R} \cdot T}{n \cdot \text{F}} \cdot \ln\left(\frac{a_{\text{H}_2} \cdot \sqrt{a_{\text{O}_2}}}{a_{\text{H}_2\text{O}}}\right) \\
&\approx \frac{\Delta^{\text{R}} G^{\circ}(T)}{2 \cdot \text{F}} + \frac{\text{R} \cdot T}{2 \cdot \text{F}} \cdot \ln\left(\frac{p_{\text{H}_2}^{\text{c}}}{p_{\text{H}_2}^{\circ}} \cdot \sqrt{\frac{p_{\text{O}_2}^{\text{a}}}{p_{\text{O}_2}^{\circ}}}\right)
\end{aligned}
\tag{2.2}
$$

The standard reversible cell voltage is indicated with $U_{\text{cell}}^{\text{rev},\circ}$, the universal gas constant is R, T equals to the temperature, n is the number of transferred electrons per reaction, F is the Faraday constant and a_{z} is the activity of hydrogen, oxygen or water. However, the form of the Nernst equation shown in the upper line is quite impractical for calculating the reversible cell voltage, which is why the version in the bottom line of eq. 2.2 is usually used. The standard reversible cell voltage is calculated from the standard reversible free enthalpy $\Delta^{\text{R}} G^{\circ}$. The activity of the gases is approximated by the ratio of the respective partial pressure p_{gas}^{x}, where x is either c (cathode) or a (anode), and the standard pressure p_{gas}°. The activity of pure liquids, like water, is assumed as unity.

At constant pressure, the standard free enthalpy decreases stronger with increasing temperature than the factor of the pressure portion. Therefore, $U_{\text{cell}}^{\text{rev}}$ also decreases with T.[65] In contrast, $U_{\text{cell}}^{\text{rev}}$ increases at constant temperature when the operating pressure increases.[65]

Ohmic Overpotential   The ohmic overpotential η_{Ω} is calculated from Ohm's law (eq. 2.3), which is the product of the current density i and the ohmic cell resistance R_{Ω}.

$$
\eta_{\Omega} = i \cdot R_{\Omega}
\tag{2.3}
$$

The ohmic resistance R_{Ω} includes the electrical resistances of the electrically conductive components used in the cell and the interfacial contact resistances between them. Further, the ionic resistance of the ionomer in the membrane and the catalyst layers is included as well.[13, 50]

The value of R_{Ω} is commonly measured *in situ* during the measurement of polarisation curves. One feasible method is the electrochemical impedance spectroscopy (EIS), in which the alternating current resistance of an electrochemical system is measured in a defined frequency interval. An extensive presentation of the method is not given in this work, but can be found in Ref. [66]. Typically, the high frequency intercept of the impedance spectrum with the real axis (high frequency resistance, R_{HF}) is assumed to be equal to R_{Ω}.

Due to the high electrical conductivities of the metallic components in a PEM-WE cell (flow fields, PTLs), their contribution to R_{HF} is small. The major contribution is caused by the protonic transport resistance of the membrane. Therefore, R_{HF} depends strongly on the thickness and the ionic conductivity of the used PEM.[64] With a thin Nafion™

212 membrane, resistances of about $60\,\mathrm{m\Omega\,cm^2}$ result at $80\,^{\circ}\mathrm{C}$, whereas with a thicker Nafion™ 115 membrane a $R_{\mathrm{HF}} \approx 115\,\mathrm{m\Omega\,cm^2}$ results at the same temperature.[67, 68]

The contribution of η_Ω to the integral cell voltage increases linearly with current density (cf. Ohm's law in eq. 2.3), which makes η_Ω to one of the major overpotentials at high current densities.[18, 19] Using thinner membranes[22, 64] or membranes with a higher ionic conductivity[29] are helpful approaches to reduce the ohmic overpotential.

Kinetic Overpotential   Another major contribution to the cell voltage is caused by the reaction kinetics of the half cell reactions. Basically, the kinetic overpotentials η_{kin} are the driving force for any electrochemical reaction.[13] Just like the previously described ohmic overpotential, the kinetic overpotential can be obtained from the experimental data. Here, a brief insight into the kinetics of electrochemical systems is given. A comprehensive description can be found in Ref. [69].

The relation between the current density i and the kinetic overpotential η_{kin} for a general electrochemical reaction

$$\mathrm{Ox} + n \cdot \mathrm{e}^- \rightleftarrows \mathrm{Red}$$
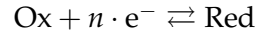
is usually described with the Butler-Volmer approach, as shown in its most basic form in eq. 2.4.

$$i = i_0^{\mathrm{ref}} \cdot \left\{ \exp\left[-\frac{\alpha_{\mathrm{red}} \cdot \mathrm{F}}{\mathrm{R} \cdot T} \cdot \eta_{\mathrm{kin}} \right] - \exp\left[\frac{\alpha_{\mathrm{ox}} \cdot \mathrm{F}}{\mathrm{R} \cdot T} \cdot \eta_{\mathrm{kin}} \right] \right\} \tag{2.4}$$

Where i_0^{ref} is the exchange current density and $\alpha_{\mathrm{red/ox}}$ is the charge-transfer coefficient for the respective direction of the reaction.

Considering only the reaction direction of interest and neglecting the corresponding backward reaction, the equation can be rearranged to η_{kin} as a function of i. The resulting eq. 2.5, which is also known as the Tafel equation, is commonly used to fit the kinetically dominated part of the polarisation curve at low current densities up to typically $100\,\mathrm{mA\,cm^{-2}}$ (cf. fig. 2.2).[64] In this way, the impact of mass transport limitations at higher current densities on the resulting kinetic parameters are limited.

$$\eta_{\mathrm{kin}} = \frac{\mathrm{R} \cdot T}{\alpha \cdot \mathrm{F}} \cdot \ln\left(\frac{|i|}{i_0^{\mathrm{ref}}} \right) \tag{2.5}$$

A major drawback of applying this approach on full cell measurements is that the contributions of the anode and the cathode to η_{kin} cannot be separated from each another. In order to achieve this, a reference electrode for the measurement of the half cell potentials is necessary. However, the integration of such an electrode is difficult for common PEM-WE cells.

From *ex situ* half cell experiments (e. g. with rotating disk electrodes), it is known that the HER kinetics on platinum is very good, which is why only low kinetic overpotentials result from this reaction.[19] In contrast, the OER follows a more complex reaction mecha-

nism, leading to noticeably higher overpotentials in a similar order of magnitude as the ohmic overpotential at industrial relevant current densities.[19] For this reason, there is a great interest in reducing the kinetic losses caused by the OER. This might be achieved by increasing the catalyst utilization or by new catalysts with higher exchange current densities.[44, 49]

Overpotentials Caused by Mass Transport and Other Effects The exemplary polarisation curve shown in fig. 2.2 reveals that the sum of the reversible cell voltage U_{cell}^{rev}, the ohmic overpotential η_{Ω} and the kinetic overpotential η_{kin} almost equals to the integral cell voltage. However, the sum of these is usually up to $100\,mV$ smaller than the measured integral voltage at industrial relevant current densities.[64] The remaining difference η_{mtx} is attributed to the limited mass transfer of water to the anode and of the produced gases away from both electrodes.[13, 61] Further, yet unknown losses can appear as well. Overpotentials of this type are not well understood yet in PEM water electrolysis.

One approach to minimize η_{mtx} is the improvement of all components, which are crucial for the mass transport. One important part is the catalyst layer. There are several studies showing that the structure of the catalyst layer can be adjusted with the ionomer to catalyst ratio, which in turn has an impact on the mass transfer characteristics.[68, 70] Further, the interface between the catalyst layer and the PTL can be optimized by e.g. coating the PTL with a MPL.[50, 64] Also, the PTL structure and porosity have an impact on the mass transfer properties and may be further influenced by the flow field design, the operating pressure and the clamping pressure.[50, 67, 71, 72]

2.2 Gas Crossover: State of Knowledge

In the preceding section, the most important components in a typical setup of a PEM-WE cell and the individual overpotentials contributing to the electrical performance were considered. This serves as a basis for the following section, in which the mass transfer behaviour with regard to gas crossover in PEM-WE cells is discussed.

The term gas crossover describes the permeation of the product gases through the membrane to the opposite side of the cell. In the previous section, the setup of a PEM-WE cell was sketched in fig. 2.1. The sketch is taken up again in fig. 2.3 and is supplemented with fluxes, indicating the directions for hydrogen and oxygen crossover. The two types of crossover are influencing the cell efficiency[73–76], the gas purity[73–75] and the system durability[77, 78]. The following sections give a detailed overview of the current state of knowledge on gas crossover by using recent literature. First, the basic mechanisms and influencing variables are discussed. Since the transport mechanisms and influencing variables are independent of the gas molecule, the examples used throughout this section are usually given for hydrogen, in order to avoid duplication (analogous equations apply for oxygen). Then, the characterisation techniques and some mitigation strategies for gas crossover are presented.
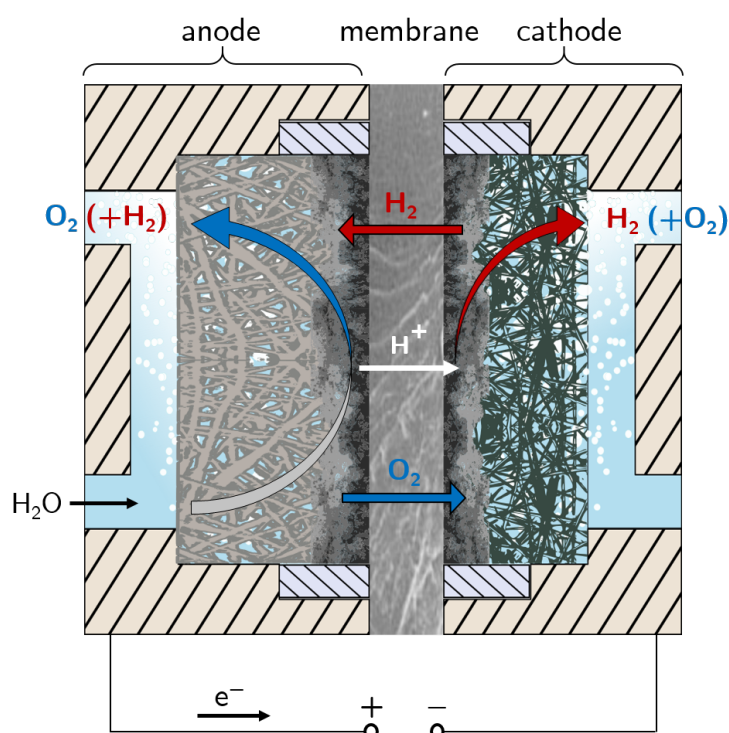

Figure 2.3: Sketch of a PEM-WE cell including the most important fluxes of the reactants. The fluxes across the membrane indicate the crossover fluxes of hydrogen (red) and oxygen (blue). The figure is adapted from Ref. [23].

2.2.1 Gas Crossover Mechanisms

Independently from the transport mechanism, the gas transport happens mainly in dissolved state through the aqueous phase of the Nafion™ membrane, whereas the transport through the polymeric phase is negligible.[29, 30, 76, 79] The gas transport through the membrane of a PEM-WE cell occurs either via a diffusive or a convective pathway.[80–82] Thus, the dissolution of gases in water is summarized first, before the transport mechanisms are discussed.

Aqueous Gas Solutions The concentration of a dissolved gas c_{gas} is generally calculated by Henry's law (eq. 2.6).

$$c_{\text{gas}} = S_{\text{gas}} \cdot p_{\text{gas}}^x \tag{2.6}$$

Where S_{gas} equals to the solubility of a certain gas in water and p_{gas}^x refers to the partial pressure of the respective gas at either the cathode ($x = $ c) or the anode ($x = $ a). In the context of PEM-WE, only hydrogen and oxygen have to be considered as gases.

The respective gas partial pressure p_{gas}^x is calculated from either the cathode pressure p^c (for hydrogen) or anode pressure p^a (for oxygen), and the water vapour pressure. At electrolysis conditions, it is assumed that the produced gas is fully saturated with water vapour, so that the saturated water vapour pressure $p_{\text{H}_2\text{O}}^{\text{sat}}$ at the respective temperature is used for the calculation of p_{gas}. For example, the resulting water vapour pressure at 80 °C is $p_{\text{H}_2\text{O}}^{\text{sat}} = 0.47\,\text{bar}$.[83] The partial pressure of hydrogen at the cathode $p_{\text{H}_2}^c$ is therefore calculated by eq. 2.7.

$$p_{\text{H}_2}^c = p^c - p_{\text{H}_2\text{O}}^{\text{sat}} \tag{2.7}$$

During ideal operation, only oxygen is dissolved on the anode side of the membrane, while hydrogen is dissolved on the cathode side.

Diffusion of Dissolved Gases Hydrogen and oxygen are produced and dissolved in the cathode and anode catalyst layer in the immediate vicinity of the membrane, which leads to a concentration gradient across the membrane towards the respective opposite compartment.[23] This concentration gradient is the driving force for gas crossover. From a practical point of view, the use of pressures instead of concentrations is more feasible, which is why the following model equations are finally converted into a pressure-dependent variant.

Several approaches for the description of diffusion exist. A very profound description of diffusion in multicomponent systems is given by the Maxwell-Stefan approach.[84, 85] The simplification of this approach to the diffusion of a single species leads to Fick's law of diffusion, which is often used for describing gas diffusion processes in PEM-

WE.[30, 76, 79, 84, 86] Equation 2.8 shows the concentration dependent version of Fick's law applied on hydrogen (analogous applies for oxygen).

$$N_{H_2}^{diff} = D_{H_2}^{eff} \cdot \frac{\Delta c_{H_2}}{\delta_{mem}} = D_{H_2}^{eff} \cdot \frac{c_{H_2}^c - c_{H_2}^a}{\delta_{mem}} \approx D_{H_2}^{eff} \cdot \frac{c_{H_2}^c}{\delta_{mem}} \tag{2.8}$$

The diffusive hydrogen flux is described by $N_{H_2}^{diff}$, $D_{H_2}^{eff}$ is the effective hydrogen diffusion coefficient considering the tortuosity and porosity of the membrane, and δ_{mem} is the membrane thickness. The equation is simplified by assuming that the hydrogen concentration difference Δc_{H_2} across the membrane is approximately equal to the the cathodic hydrogen concentration $c_{H_2}^c$, because the anodic hydrogen concentration $c_{H_2}^a$ is negligibly small.[79]

For transferring Fick's law from the concentration dependent version into the pressure dependent form, the three previous equations (eq. 2.6, eq. 2.7 and 2.8) are be combined to eq. 2.9.

$$N_{H_2}^{diff} = D_{H_2}^{eff} \cdot S_{H_2} \cdot \frac{p_{H_2}^c}{\delta_{mem}} = P_{H_2} \cdot \frac{p_{H_2}^c}{\delta_{mem}} \tag{2.9}$$

The permeability P_{H_2} is commonly reported in literature and equals to the product of solubility and effective diffusion coefficient.[29, 76] Knowing the permeability and the membrane thickness, the equation allows a quick estimation of the diffusive hydrogen flux from the hydrogen partial pressure.

In principle, the diffusive crossover flux of hydrogen is higher than that of oxygen in most PEM-WE operating scenarios. This is mainly due to the higher solubility and higher diffusion coefficient of hydrogen in water, resulting in a higher dissolved hydrogen concentration at the cathode compared to the dissolved oxygen concentration at the anode.[29, 76] Further, PEM-WE systems are typically operated at enhanced cathode pressures whereas the anode remains at ambient pressure, which according to eq. 2.9 enhances the diffusive transport as well.[16, 74, 75, 87]

Convective Transport of Dissolved Gases The convective transport of the dissolved gases is due to a net water transport through the membrane, resulting from a hydraulic and electro-osmotic mechanism.[80] For instance, the hydraulic water transport through the membrane is described by Darcy's law, given in eq. 2.10.[80, 82, 88, 89] The equation expresses the velocity of the transported water $v_{H_2O}^{hyd}$ as a function of the hydraulic permeability of Nafion™ $P_{H_2O}^{hyd}$, the dynamic viscosity of water μ_{H_2O}, the pressure difference Δp and the membrane thickness δ_{mem}.

$$v_{H_2O}^{hyd} = \frac{P_{H_2O}^{hyd}}{\mu_{H_2O}} \cdot \frac{\Delta p}{\delta_{mem}} \tag{2.10}$$

Within this hydraulic water flux, dissolved hydrogen and oxygen are transported. The hydraulic gas flux $N_{H_2}^{hyd}$, shown for hydrogen in eq. 2.11, is calculated from Darcy's law (eq. 2.10) and the dissolved hydrogen concentration c_{H_2}.

$$N_{H_2}^{hyd} = v_{H_2O}^{hyd} \cdot c_{H_2} \tag{2.11}$$

However, this effect is assumed to be negligibly small in PEM-WE cells based on Nafion™[76, 79], because the hydraulic permeability $P_{H_2O}^{hyd}$ of Nafion™ is very low[90, 91].

Another type of convective transport of water is by means of the electro-osmotic drag.[75, 79–81, 92, 93] During electrolysis, the electric field between the electrodes causes a proton transport through the membrane. As the protons are solved in water, water is dragged with the protons from anode to cathode. The velocity of the dragged water $v_{H_2O}^{drag}$ depends on the number of dragged water molecules per proton n_{drag}, the current density i, the Faraday constant F and the concentration of water c_{H_2O} (eq. 2.12).

$$v_{H_2O}^{drag} = \frac{n_{drag} \cdot i}{F \cdot c_{H_2O}} \tag{2.12}$$

Considering the concentration gradient of the dissolved gases across the membrane, the gas flux due to the electro-osmotic drag of water not only depends on the velocity of the dragged water, but also on the present dissolved gas concentration. For hydrogen, the resulting flux $N_{H_2}^{drag}$ is described by eq. 2.13.

$$N_{H_2}^{drag} = v_{H_2O}^{drag} \cdot c_{H_2} \tag{2.13}$$

Just as the hydraulic transport of water, the gas transport via dragged water is often neglected in literature. However, its significance should be reconsidered especially at high current densities.[79, 94] At this point, it is emphasized that the transport of hydrogen and oxygen due to drag occurs in the same direction for both gases: from the anode to the cathode. With regard to hydrogen, the transport via drag acts in the opposite direction as the diffusion process, which should weaken the net hydrogen crossover at high currents at which $v_{H_2O}^{drag}$ is high. In contrast, the net oxygen crossover should be amplified by this transport mode, because it acts in the same direction as oxygen diffusion.[67, 79]

2.2.2 Influencing Variables on Gas Crossover

The mechanisms for gas crossover in PEM-WE were introduced above. The diffusive transport of dissolved gases was identified to be the governing crossover mechanism.[75, 79, 80, 95] For the discussion regarding the impact of influencing variables on diffusion, the previously introduced Fick's law in eq. 2.8 and 2.9 is shown as a function of typical operating parameters such as temperature, pressure and the current density in eq. 2.14.

$$N_{H_2}^{diff}(T, p_{H_2}^c, i) = D_{H_2}^{eff}(T) \cdot \frac{c_{H_2}^c(i)}{\delta_{mem}} = P_{H_2}(T) \cdot \frac{p_{H_2}^c(i)}{\delta_{mem}} \tag{2.14}$$

Operating Conditions

The impact of common operating parameters, such as temperature, pressure and current density, are summarized first, before the influence of the cell configuration is discussed.

Temperature   Generally, the diffusive crossover flux increases with temperature.[96, 97] This is the result of increasing hydrogen and oxygen diffusion coefficients in water at elevated temperatures.[27, 28] Since the diffusion coefficient is dominating the permeability (cf. eq. 2.9), it also increases with temperature.[29]

Partial Pressure   According to eq. 2.14, an increase in the partial pressure or operating pressure results in a higher diffusive crossover flux. This leads to higher concentration gradient across the membrane, which equals to an increased driving force for diffusion.[16, 28, 29, 97]

Current Density   In addition to the temperature and pressure dependence of the diffusive crossover fluxes, it is also reported that a larger applied current density enhances oxygen crossover[98, 99] and hydrogen crossover[67, 73, 75, 93, 95, 97, 99], as shown in fig. 2.4. Trinke *et al.*[23, 97] have discussed several possible reasons and proposed theories for the current dependence of the crossover fluxes, which are summarized below.

Similar to the influences of pressure and temperature on the coefficients in Fick's law as presented above, further temperature and pressure effects might be induced by applying a current to the PEM-WE cell. The increase in current density leads to higher heat production during the electrochemical reactions, which in turn results in an increased temperature within the CCM. As a consequence, the diffusion coefficients for hydrogen and oxygen in water increase, leading to a higher gas crossover flux according to eq. 2.14. However, a temperature increase of more than $100\,\mathrm{K}$ per $\mathrm{A\,cm^{-2}}$ would be necessary in order to explain the current dependence of the crossover flux as reported in Ref. [97]. As this is highly improbable, the local temperature increase is an implausible explanation for the strong increase of the hydrogen crossover flux with current density.

Another explanation, also proposed by others[28, 75, 95], is the local pressure enhancement within the catalyst layer. The increasing current density leads to a higher gas production rate at the electrodes. Assuming a limited removal of the gases, it is therefore possible that the pressure increases locally within the catalyst layer. According to eq. 2.14, higher pressures result in an increased driving force for diffusion and hence, the crossover flux increases as well. However, a simulation has revealed that the local pressure enhancement is too small to explain the increasing crossover flux with current density.[97]

A further theory deals with the supersaturation of water with hydrogen in the cathode catalyst layer, or respectively with oxygen in the anode catalyst layer.[23, 93, 97] As described previously, evolved hydrogen and oxygen are solved in water surrounding the catalyst particles in the catalyst layer before they transfer into gaseous state. The

supersaturation theory suggests that with increasing gas evolution at higher currents, the dissolved gas saturation increases concurrently to a point where it exceeds the theoretical saturation concentration of the respective gas expected from Henry's law (eq. 2.6). Exceeding the saturation concentration has already been observed experimentally for both gases, hydrogen and oxygen.[100–104] Considering this concentration increase in the concentration dependent version of Fick's law in eq. 2.8 and 2.14, the increasing crossover flux with current density is explained. Trinke *et al.*[23, 97] show with their model that out of all discussed theories, the supersaturation theory is the best fit for the observed current dependence of the gas crossover flux.

The impacts of all three operating parameters on the gas crossover flux are summarized in fig. 2.4.
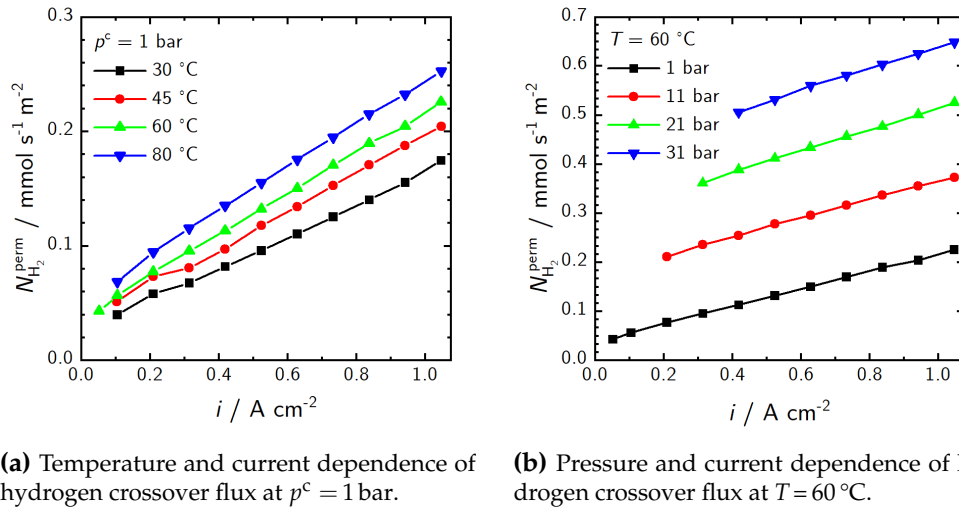
(a) Temperature and current dependence of hydrogen crossover flux at $p^c = 1$ bar.

(b) Pressure and current dependence of hydrogen crossover flux at $T = 60\,°C$.

Figure 2.4: Impact of common operating variables on the hydrogen crossover flux of a PEM-WE cell with a fumea EF-40 membrane. The impact of temperature and current density at $p^c = 1$ bar are shown in (a). In (b), the influence of the cathode pressure and the current density at $T = 60\,°C$ are shown. The data is taken and adapted from Ref. [97].

Cell Configuration

In addition to the applied operating condition, the cell setup affects the gas crossover properties in PEM-WE cells as well.

Membrane From eq. 2.14 it becomes clear that with decreasing membrane thickness, the concentration gradient across the membrane increases and consequently, the gas crossover flux increases.

Besides the physical dimension of the membrane, the membrane chemistry is crucial for its permeability properties. For example, PFSA-based membranes can be produced with different backbone to side chain ratios. Membranes, which contain a larger density of side chains, also contain more sulfonic acid groups and can bind more water.[28] As

the diffusion occurs mainly in the aqueous state, this leads to an increased membrane permeability and hence, to higher crossover fluxes.[28]

Moreover, proton conducting membranes can be obtained by completely different chemistries, which preferentially have improved permeability characteristics leading to lower crossover fluxes (e. g. radiation-grafted membranes [105, 106], hydrocarbon membranes[107, 108]).

Catalyst Layer   Another important material property for the gas crossover characteristics, that is less intuitive than the membrane but no less important, is the structure of the catalyst layer. In the previous discussion on the current dependence of the gas crossover flux, it was already briefly mentioned that the supersaturation of water with hydrogen and oxygen occurs in the respective catalyst layer.

Trinke *et al.*[23, 97] explain the continuing supersaturation of water with hydrogen with a limited transfer of the dissolved gas into the gaseous state, which results from high mass transport resistances in the ionomer of the catalyst layer. These mass transport resistances can be varied by changing the catalyst layer structure. In order to achieve different catalyst layer structures, Trinke *et al.*[68] and Bernt *et al.*[70] have varied the ionomer content in the cathode and anode catalyst layer, respectively. Both have observed that with increasing ionomer content, the mass transport losses η_{mtx} increase, implying that the transport of the dissolved gases is increasingly limited at higher ionomer contents. In addition to the voltage loss analysis, Trinke *et al.*[68] have investigated the impact of the ionomer content on the hydrogen crossover as well. It is reported that the hydrogen crossover flux increases with the ionomer content, which is consistent with the increasing mass transport losses η_{mtx} seen in the cell voltage analysis. With increasing ionomer content, the dissolved gas travels a longer distance through the ionomer in the catalyst layer. This leads to greater mass transfer resistances, resulting in an increasing supersaturation and thus, to a higher crossover flux.

Cell Setup and Cell Design   As discussed above, it was found that the intrinsic properties of the key components of a PEM-WE cell, namely the membrane and the catalyst layer, have a decisive impact of the resulting gas crossover. However, the properties of these layers are also influenced by other cell components.

On both sides of the CCM, a respective anode and cathode PTL is located. As mentioned before, the main purposes of the PTLs are to ensure a good electrical connection between the catalyst layers and the flow fields, and to stabilize the CCM mechanically. If the PTL structure displays e. g. a low porosity, the water supply towards and the gas removal away from the catalyst layers can be hindered.

Furthermore, unstable PTL materials can suffer from the external compression, causing fluid transport issues (e. g. Ref. [109, 110]). Especially with highly compressible and brittle carbon materials, too high clamping pressures can be transferred to other porous media inside the cell as well.[67, 71] Thus, not only the PTLs but also the catalyst layers and

the membrane may be compressed excessively, which in turn can affect their properties. However, high clamping pressures are necessary in order to maintain low interface resistances.[67, 71, 109, 110]

The last remaining component to be considered is the flow field of the cell. Its design is crucial for the transmission of the clamping pressure to the PTLs and CCM. It is expected that most of the external pressure is transferred via the lands of the flow field. Therefore, areas with higher and lower compression forces can result. So far, the impacts of the PTL structure, the cell compression and the flow field design on gas crossover are not fully understood.

2.2.3 Experimental Characterisation of Gas Crossover

The preceding theoretical assessment of gas crossover is important for modelling purposes and for understanding the impact of the various influencing variables. In order to validate the models and to reveal gaps, the experimental analysis of gas crossover during electrolysis operation in full PEM-WE cells is necessary.

Hitherto, several approaches for the determination of hydrogen crossover exist. The basic diffusive hydrogen flux at zero current, as expected from Fick's law (eq. 2.8 and 2.9), can be determined by permeation experiments as shown in Ref. [76] and [80]. Further, permeated hydrogen can be measured by electrochemical compensation or by linear sweep voltammetry, as shown by Bensmann *et al.*[111] and Pei *et al.*[112], respectively. Recently, Kang *et al.*[113] have proposed a tandem cell setup, where the anode product gas stream is supplied to a second cell, in which the hydrogen is quantified electrochemically. However, all these methods are not applicable for the determination of oxygen crossover or cannot be performed under electrolysis conditions. For this reason, the measurement of the gas composition of the product gas stream is an established method for the experimental determination of both, hydrogen and oxygen crossover, under operating conditions. This method is explained in more detail below.

Hydrogen Crossover The hydrogen crossover flux can be determined by measuring the anodic hydrogen in oxygen content, which can be performed by e. g. gas analysing sensors[71, 97], a mass spectrometer[80] or a gas chromatograph[67, 68, 79, 99, 114]. Due to its availability and high accuracy, the latter is used throughout this work. The composition of the dried anode gas is described by eq. 2.15.

$$\phi_{H_2}^a = \frac{N_{H_2}^{cross}}{N_{out}^a} = \frac{N_{H_2}^{cross}}{N_{H_2}^{cross} + N_{O_2}^{evo}} \tag{2.15}$$

The anodic hydrogen content $\phi_{H_2}^a$ is defined as the ratio between the hydrogen crossover flux $N_{H_2}^{cross}$ and the total anode gas flux N_{out}^a, which is the sum of $N_{H_2}^{cross}$ and the evolved oxygen flux $N_{O_2}^{evo} = \frac{i}{4 \cdot F}$ according to Faraday's law. The measurement of the hydrogen content during electrolysis operation is easily implemented by supplying the anode pro-

duct gas to the desired analytic instrument. Furthermore, this method has the advantage that the composition of the gas mixture is constantly monitored. In this way, actions can be taken when a critical gas mixture is formed (lower explosion limit, LEL $\phi_{H_2}^a \geqq 4\,\text{vol\%}$[115]) or a safety criterion is reached (typically 50 % LEL). Finally, the hydrogen crossover flux is calculated from the experimentally determined content according to eq. 2.16.

$$N_{H_2}^{cross} = \frac{\phi_{H_2}^a \cdot N_{O_2}^{evo}}{1 - \phi_{H_2}^a} \qquad (2.16)$$

Oxygen Crossover   Theoretically, the oxygen crossover can be determined analogous to the hydrogen crossover, by measuring the cathode oxygen in hydrogen content $\phi_{O_2}^c$ as described by eq. 2.17.

$$\phi_{O_2}^c = \frac{N_{O_2}^{cross} - N_{O_2}^{recomb}}{N_{out}^c} = \frac{N_{O_2}^{cross} - N_{O_2}^{recomb}}{N_{O_2}^{cross} + N_{H_2}^{evo} - N_{O_2}^{recomb} - N_{H_2}^{recomb}} \qquad (2.17)$$

However, determining the oxygen crossover from the cathodic gas composition is a greater challenge than with hydrogen, because some of the permeated oxygen $N_{O_2}^{cross}$ recombines with hydrogen on the platinum particles used in the cathode catalyst layer. Therefore, the measurable oxygen content is lower than observed from permeation measurements using only the membrane material without catalyst layers. As the amounts of recombined oxygen $N_{O_2}^{recomb}$ and hydrogen $N_{H_2}^{recomb}$ are unknown, the determination of the actual oxygen crossover during electrolysis operation remains to be a challenge. From a safety point of view, however, this is a useful side effect, because no explosive gas mixtures are formed.

2.2.4 Consequences of Gas Crossover and Mitigation Strategies

The major drawbacks of gas crossover in PEM-WE are efficiency losses[73–75], safety issues[73–75] and degradation issues[77, 78]. These consequences are discussed briefly in the following and then, mitigation strategies for gas crossover are presented.

Efficiency Losses   In the context of hydrogen crossover, the faradaic efficiency is the most meaningful measure, since it describes the ratio of actually usable hydrogen to the theoretically expected amount of produced hydrogen.[60, 67] The amount of produced hydrogen is calculated by Faraday's law, describing the proportional relation between the applied current density and the amount of charge required per reaction. All parameters leading to a higher hydrogen crossover flux, such as thin membranes or high hydrogen pressures, result in a lower faradaic efficiency.

Besides the crossover of hydrogen, another hydrogen loss mechanism can occur within the cell. Some of the produced hydrogen recombines with permeated oxygen from the anode, because the platinum particles in the cathode catalyst layer catalyze the recombina-

tion of the gases to water. The amount of recombined hydrogen is hard to quantify, as the actual oxygen crossover flux at electrolysis conditions is unknown.

Safety Issues   Safety issues induced by gas crossover were adressed briefly in the previous section.

Especially on the anode side, critical gas mixtures with more than 4 vol% hydrogen in oxygen (lower explosion limit[115]) can be formed at elevated cathode pressures and during operation of the PEM electrolyzer. When hydrogen permeates through the membrane into the anode compartment, it is diluted with a certain amount of produced oxygen. This amount increases with the applied current density, as given by Faraday's law. Hence, low current densities result in a low dilution of permeated hydrogen. Typically, PEM electrolyzers are only operated up to 50 % LEL, in order to ensure sufficient safety. Ref. [73] and [74] address the safety issues of PEM electrolyzers operated at high pressures in more detail.

On the cathode side, corresponding safety problems induced by oxygen crossover usually do not arise, since most of the permeated oxygen recombines with hydrogen on platinum. However, remaining oxygen needs to be removed from the cathode product gas stream to ensure a high purity of the produced hydrogen.

Degradation Issues   The recombination of permeated oxygen with hydrogen in the cathode of the PEM-WE cell is favourable in terms of the system safety. However, the recombination reaction is suspected to trigger undesired side reactions, which lead to the chemical degradation of some components.[77, 78, 116–121] During the recombination reaction, highly reactive radicals are formed as an intermediate to the actual recombination product water. These radicals can attack the ionomer in the catalyst layer and the membrane, eventually leading to cell failure.[118, 121] In Ref. [40] and [120], a review on membrane degradation mechanisms in PEM-WE cells is given. Although the chemical degradation occuring in PEM-WE cells is not fully understood yet, oxygen crossover is considered to be the main cause for the chemical material degradation.[22, 77, 78, 119]

Mitigation Strategies   For the reduction of the presented drawbacks arising from gas crossover, mitigation strategies are required. Trinke *et al.*[79] evaluated several crossover mitigation strategies for PEM-WE and AWE. In the following, the most prominent strategies proposed for PEM-WE are summarized and evaluated with regard to efficiency, safety and degradation issues.

A simple possibility to reduce gas crossover without changing the cell setup or the materials used, is to choose operation parameters at which the driving forces for the crossover are minimized. For example, low temperatures, low gas pressures and low current densities reduce the driving force and hence, the crossover flux. However, this approach will most likely only lead to a lower degradation rate, because the oxygen crossover flux remains small. Although the actual hydrogen crossover flux is also reduced

at these conditions, efficiency losses and safety issues arise at low current densities. Moreover, these operation conditions are contradictive with the electrical performance goals of a PEM-WE system. Therefore, this approach can only be considered as a proof of concept for first generation PEM electrolyzers to work reasonably well. Certainly, this approach is ineligible for optimized systems.

Another approach suggests to taylor the properties of new membrane materials towards lower gas permeabilities. First studies show that lower gas permeabilities compared to those of Nafion™ are achievable.[105–108] This is an important criterion in order to compete with Nafion™, but the material stability and durability are insufficient yet. Therefore, efficiency, safety and degradation issues might be reduced with better ionomers, if their intrinsic durability and stability gets improved.

A third strategy suggests to reduce the supersaturated dissolved gas concentrations, which have an impact on the driving force for crossover during electrolysis. One approach is to change the catalyst layer structure by optimizing the ionomer to catalyst ratio, as shown by Trinke *et al.*[68] Furthermore, the catalyst loading and the catalyst layer thickness should be considered as well. However, the effectiveness of an improved catalyst layer with regard to efficiency, safety and degradation is difficult to predict.

Another strategy deals with the implementation of an interlayer within the membrane. Here, two approaches are possible. First, so-called blocking interlayers may be included in the membrane.[79] The blocking interlayer consists of a material, which only allows proton transport but is impermeable for water. Hence, the electrolysis reaction still works, but the transport of dissolved gases through the membrane is suppressed. Previously, graphene[122], graphene oxide[123] and hexagonal boron nitride[124] were successfully used for crossover mitigation. However, full cell experiments with such membranes containing blocking interlayers usually show an inferior electrical performance, which is ascribed to higher membrane resistances.[123] This is either caused by a lower overall protonic conductivity or an insufficient water content in the membrane.

The second approach for interlayers involves the implementation of recombination catalysts, such as platinum. With this approach, the safety issue associated with high hydrogen crossover fluxes is addressed in particular, because the formation of explosive gas mixtures is prevented. For this, a recombination catalyst is dispensed within the membrane. Permeated oxygen and hydrogen meet at the catalyst particles in the membrane and recombine to water. The effective reduction of the anodic hydrogen content was already shown before.[125–130] However, the implementation of a noble metal as a recombination catalyst increases the effort and the costs for membrane manufacturing. Therefore, such a recombination interlayer has to be well designed in order to reduce both side effects to a minimum. Moreover, this approach utilizes the recombination reaction between hydrogen and oxygen, which was previously identified as a key trigger for the chemical degradation of the polymer. For this reason, the influence of a recombination interlayer on the durability of the PEM-WE cell must be investigated in future. In addition, the recombination reaction consumes hydrogen, which lowers the efficiency. Therefore,

the advantages and disadvantages of using a recombination interlayer must be considered carefully.

3 Research Questions

From the previous considerations it became clear that the gas crossover during electrolysis conditions depends on many operating parameters and design variables. Although the research in the last years progressed and revealed new relations, the following research questions remain unanswered and will be examined in more detail in this work.

Research Question 1:   How does cell compression affect hydrogen crossover?

   The consideration of the cell compression is important for several reasons. Firstly, although the investigated materials are usually named clearly in the various crossover studies from different laboratories, the compression force or clamping pressure is often unknown. On account of this, the comparison of results from different laboratories is difficult. Secondly, it was previously mentioned that the structure of the catalyst layer has a significant impact on the supersaturation behaviour of water, and thus on the resulting crossover. As the catalyst layer is a highly porous structure and the carbon PTL used at the cathode is compressible, it is expected that both structures change with compression. In this work, it is examined how different cell compression levels affect the hydrogen crossover.

Research Question 2:   How do high current densities above $5\,\mathrm{A\,cm^{-2}}$ affect hydrogen crossover?

   Due to the research progress in PEM-WE, many material parameters can be controlled in order to achieve specific properties. This is accompanied by an increase in efficiency, often resulting in higher applicable current densities without exceeding voltage limits. Although the hydrogen production rate increases with the applied current density, commercial PEM electrolyzers are nowadays rarely operated above $2\,\mathrm{A\,cm^{-2}}$. In research applications, the operating window is extended frequently up to $4\,\mathrm{A\,cm^{-2}}$ and some studies even exceed this current density. Therefore, it is important to verify whether the previous findings on hydrogen crossover are still valid in the extended operation window or whether yet unknown effects become dominating at such high current densities above $5\,\mathrm{A\,cm^{-2}}$.

Research Question 3:   What is the impact of increased cathode pressures on hydrogen crossover, in addition to the cell compression and high current densities?

   When working on new research questions, it makes sense to define one variable and to vary it under otherwise identical conditions, in order to describe the effects on the

system in the first instance. However, the variation of typical thermodynamic parameters, such as pressure and temperature, can be useful in uncovering physical relationships. With regard to the first two research questions, it is therefore interesting to evaluate how a variation in cathode pressure affects hydrogen crossover in addition to the main investigated variable. The impact of increased cathode pressures on the performance and on the crossover characteristics is especially from the industrial point of view relevant. On account of this, the investigations on the compression influence and the impact of high current densities on hydrogen crossover is extended by crossover measurements at elevated cathode pressures.

Research Question 4: How can the oxygen crossover be meausured precisely by changing the cathode catalyst?

With the variety of studies focussing on hydrogen crossover, it is striking that there are very few studies dealing with oxygen crossover in PEM-WE. Since the oxygen crossover plays a crucial role for the chemical degradation of the ionomer, more attention to the determination of the oxygen crossover should be paid. The main reason for the challenging quantification of permeated oxygen during electrolysis is that it recombines at the typically used platinum catalyst within the cathode catalyst layer with evolved hydrogen to water, before it can be quantified properly. One possible approach for the measurement of the oxygen crossover is to use a recombination-inactive catalyst on the cathode. In this work, several cathode catalysts are evaluated with regard to their recombination activity and their eligibility to quantify the oxygen crossover at electrolysis conditions.

Research Question 5: What is important for the design of a recombination interlayer within the polymer electrolyte membrane?

The integration of a membrane interlayer with a recombination catalyst, such as platinum, is a known and well-working strategy for the reduction of the anodic hydrogen content. Since such a platinum interlayer increases the costs and the manufacturing effort, it must be well designed to minimize both impacts. One aspect, for example, is the positioning of such an interlayer within the membrane. In the context of this work, three different interlayer positions are examined with respect to their recombination effectiveness and compared to a reference CCM without an interlayer.

4 Refining the Role of Influencing Variables on Hydrogen Crossover

The previous dicussion of recent literature revealed research gaps in the further investigation of the influence of design and operating variables on hydrogen crossover. The resulting first three research questions introduced in chapter 3 are examined in two different studies in this chapter.

Research Question 1: How does cell compression affect hydrogen crossover?

Research Question 2: How do high current densities above $5\,\mathrm{A\,cm^{-2}}$ affect hydrogen crossover?

Research Question 3: What is the impact of increased cathode pressures on hydrogen crossover, in addition to the cell compression and high current densities?

Research question 1 was elaborated in an experimental study dealing with the impact of compression of a PEM-WE cell on the electrical performance and on hydrogen crossover. The results were published in a peer-reviewed journal. The article is introduced with a summary of the methods and results in section 4.1.

For the investigation of research question 2, the hydrogen crossover of a PEM-WE cell was examined at current densities up to $10\,\mathrm{A\,cm^{-2}}$. The findings of the study are summarized in section 4.2.

In addition to the investigation of the two variables on hydrogen crossover, the variation of the cathode pressure can help to consolidate physical relationships between the variables. To adress research question 3, the influence of enhanced cathode pressures on hydrogen crossover was considered in both experimental studies as well as in sections 4.1 and 4.2.

4.1 Impact of Cell Compression on Hydrogen Crossover

The influence of compression and elevated cathode pressures on hydrogen crossover (research questions 1 and 3) are adressed in a peer-reviewed article named "The Effect of Cell Compression and Cathode Pressure on Hydrogen Crossover in PEM Water Electrolysis" (*J. Electrochem. Soc.* 169(1):014502, 2022). The referenced supplemental information can be found in Appendix A. The original article follows behind these summarizing paragraphs on the concept and key findings.

Four different cathode compression levels are introduced in a PEM-WE cell setup by adjusting the height of an insulating component in 25 μm steps. This allows a defined maximum compression of the cathode by the same increment. The resulting differences in the contact pressure across the geometric cell area is confirmed with pressure measuring films. Precisely, it is shown that the contact pressure with the highest compression level is locally the fivefold value than measured with the lowest compression level. Moreover, each compression level is examined in a full PEM-WE cell with regard to its polarisation behaviour and hydrogen crossover characteristics during electrolysis operation.

The analysis of the anodic gas composition at ambient pressure reveals that the anodic hydrogen content is independent of the compression level up to $1\,\mathrm{A\,cm^{-2}}$ and then rises with increasing compression. This finding implies that the mass transport resistance for transferring dissolved hydrogen into the gaseous state increases with compression at current densities above $1\,\mathrm{A\,cm^{-2}}$. Finally, the hydrogen crossover flux is enhanced as a result of a growing hydrogen concentration in the cathode catalyst layer. The limited mass transport of hydrogen is supported in the cell voltage analysis. Although higher compression levels result in reduced interfacial contact resistances and hence, to lower cell voltages, the mass transport overpotentials increase.

Moreover, the anodic hydrogen content is measured at elevated cathode pressures up to 15 bar. The results show that the increase of the initial driving force for hydrogen crossover by elevating the cathode pressure leads to higher hydrogen crossover fluxes, but also that the impact of the compression is amplified. The combination of elevated cathode pressures and high compression levels at higher current densities results in massive hydrogen crossover fluxes, leading to explosive gas mixtures. Hence, the stronger compressed cells showing a superior electrical performance, cannot be operated below the technical safety limit of 50 % LEL at cathode pressures above 5 bar.

In summary, a high cell compression has a negative impact on hydrogen crossover. This is in contrast to the improved electrical performance at high compression. Furthermore, the compression effect on hydrogen crossover is amplified by increased cathode pressures.

The Effect of Cell Compression and Cathode Pressure on Hydrogen Crossover in PEM Water Electrolysis

Agate Martin,[1] Patrick Trinke,[1] Markus Stähler,[2] Andrea Stähler,[2] Fabian Scheepers,[2] Boris Bensmann,[1,z] Marcelo Carmo,[2,3] Werner Lehnert,[2,4] and Richard Hanke-Rauschenbach[1]

[1]*Leibniz University Hannover, Institute of Electric Power Systems, 30167 Hannover, Germany*
[2]*Forschungszentrum Jülich GmbH, Institute of Energy and Climate Research, IEK-14, Electrochemical Process Engineering, 52425 Jülich, Germany*
[3]*Mechanical and Materials Engineering, Queen's University, Kingston, K7L 3N6 ON, Canada*
[4]*RWTH Aachen University, Aachen, Germany*

Hydrogen crossover poses a crucial issue for polymer electrolyte membrane (PEM) water electrolysers in terms of safe operation and efficiency losses, especially at increased hydrogen pressures. Besides the impact of external operating conditions, the structural properties of the materials also influence the mass transport within the cell. In this study, we provide an analysis of the effect of elevated cathode pressures (up to 15 bar) in addition to increased compression of the membrane electrode assembly on hydrogen crossover and the cell performance, using thin Nafion 212 membranes and current densities up to 3.6 A cm^{-2}. It is shown that a higher compression leads to increased mass transport overpotentials, although the overall cell performance is improved due to the decreased ohmic losses. The mass transport limitations also become visible in enhanced anodic hydrogen contents with increasing compression at high current densities. Moreover, increases in cathode pressure are amplifying the compression effect on hydrogen crossover and mass transport losses. The results indicate that the cell voltage should not be the only criterion for optimizing the system design, but that the material design has to be considered for the reduction of hydrogen crossover in PEM water electrolysis.
© 2022 The Author(s). Published on behalf of The Electrochemical Society by IOP Publishing Limited. This is an open access article distributed under the terms of the Creative Commons Attribution 4.0 License (CC BY, http://creativecommons.org/licenses/by/4.0/), which permits unrestricted reuse of the work in any medium, provided the original work is properly cited. [DOI: 10.1149/1945-7111/ac4459]

Supplementary material for this article is available online

For the development of next generation polymer electrolyte membrane (PEM) water electrolysers, the generation of a comprehensive understanding of gas crossover phenomena is necessary.[1–5] Furthermore, the voltage loss mechanisms in the electrochemical polarisation behaviour of PEM water electrolysers are not fully resolved yet and offer possibilities for improvement. For instance, thin membranes are required for the reduction of undesired ohmic voltage losses.[6–8] However, thin membranes also lead to higher concentration gradients of the produced gases across the membrane, which results in enhanced gas crossover.[4,5,9] Hence, the loss of hydrogen leads to reduced faradaic efficiencies and triggers safety issues, which have to be solved for future system designs.[1,4,5,10–12]

There are various existing studies dealing with the influence of external operation conditions on hydrogen crossover. In summary, these studies found that increases in cell temperature, in cathode pressure, and in current density result in increased hydrogen crossover.[3–5,9,10,13–15] Further investigations on structural effects were carried out by Trinke *et al.*[16] and Bernt *et al.*[9] These show that an increase of the ionomer content within the cathode catalyst layer leads to higher anodic hydrogen volume fractions. It is now understood that the limited transport of evolved hydrogen from the catalyst into the pores translates into increased dissolved hydrogen concentrations, which eventually results in higher hydrogen crossover and higher mass transport losses.[14–16]

Recently, Stähler *et al.*,[17] co-authors in this study, have investigated the impact of porous transport layer compression on hydrogen crossover at ambient pressure. They found that the hydrogen in oxygen content increases at higher current densities, the more the porous transport layer on the cathode (PTL-c) was compressed. Based on this and further data,[4,5,10,14,15] Omrani *et al.*[18] have developed a model for hydrogen crossover in PEM water electrolysers. They concluded that the super-saturation of water with evolved hydrogen is a decisive explanation for hydrogen crossover.

However, it was emphasized that the interaction of high compression with other parameters (e. g. high current densities) needs to be further explored.

In this context, we understand that the interface between PTL and catalyst layer needs to be considered as well. Usually, high clamping pressures are chosen in order to allow good electric conductivity across the interfaces, which results in lower ohmic losses.[6,19] However, high clamping pressures have other negative consequences.[20] Especially on the cathode side, where the carbon PTL-c is more compressible than the titanium PTL-a, mass transport limitations are typically found due to reduced permeability of the PTL-c and the catalyst layer.[6,18,19,21,22] This trade-off was already evidenced by Stähler *et al.*[17]

These works highlight that further investigations on the cathodic structural properties are necessary in order to develop a comprehensive understanding of hydrogen crossover in PEM water electrolysers. In order to meet this objective, this study aims to answer the questions whether the experimental findings on the compression effect of Stähler *et al.*[17] can be validated in a different cell setup and how an increase in cathode pressure in combination with the variation of the cell compression affects hydrogen crossover and voltage losses caused by mass transport. For this, four different compression levels were introduced into the cell setup and the anodic hydrogen in oxygen content was measured at four cathode pressures at each compression level. Moreover, the polarisation behaviour of each compression level and each cathode pressure was measured in order to perform a thorough cell voltage analysis.

Experimental

Material and setup.— *Catalyst coated membranes.*—The catalyst coated membranes (CCMs) were fabricated with the decal method that has been described in detail previously.[23,24] First, the anodes were produced by coating an iridium dispersion on a glass fibre reinforced PTFE substrate (140 μm, Saint Gobain) by means of a 200 mm slot die (TSE Troller AG) (anode composition: 70 wt% iridium(IV)oxide (Premion, Alfa Aesar) and 30 wt% Nafion ionomer

[z]E-mail: boris.bensmann@ifes.uni-hannover.de

(Chemours)). Subsequently, the cathodes were produced in the same manner by using a platinum dispersion (cathode composition: 85 wt% platinum supported on high surface area Ketjenblack (60% Pt; EC-300J, PK catalyst) and 15 wt% Nafion ionomer (Chemours)). After drying at 80 °C, the electrodes were cut into pieces of 2 × 2 cm^2 and hot pressed on a Nafion 212 membrane at 130 °C and 0.5 kN cm^{-2}. The catalyst loading was 0.20 ± 0.02 mg$_{Pt}$ cm^{-2} for the cathode and 1.05 ± 0.05 mg$_{Ir}$ cm^{-2} for the anode.

Porous transport layers.—For the anode side, the same titanium PTL-a (sintered fibers, 350 μm, Bekaert) sputtered with iridium (0.05 mg cm^{-2}) to prevent corrosion,[25,26] was used for all measurements. In order to achieve the most uniform and reproducible compression level possible, a carbon PTL-c sheet (H23I2, Freudenberg) of approximately 30 × 40 cm^2 was cut into 2 × 2 cm^2 pieces. The thickness of all individual samples was determined with a thickness measuring device (160 kPa contact pressure) and only samples with a thickness of 200 ± 4 μm were used.

Cell setup.—The 4 cm^2 cell used was designed by Fraunhofer ISE.[27] The current collectors and flow fields are made of gold-coated titanium. The contact force is applied with an adjusting screw perpendicular to the cell's base area and is monitored with a load cell between the screw and the cell (K-14 with GM77, Lorenz Messtechnik GmbH). The applied force after thermal conditioning was 3 kN for every compression level. Figure 1a illustrates the cell unit in an uncompressed state.

For means of isolation and proper positioning of both PTLs, each electrode block is equipped with a frame made of PEEK. The different compression levels were introduced by different thicknesses of the cathode frames. In Fig. 1b, the cell setup is visualized for an uncompressed state. Since an identical anode frame was used in all measurements and the carbon PTL-c is highly compressible, it is assumed that most of the compression acts on the cathodic cell compartment. Further, the cell is sealed with a flat gasket (60 FC-FKM 200, 0.8 mm, Freudenberg) on the frames around the flow fields at both electrodes. The same gaskets were used for all measurements.

In this work, the compression levels are referred in increasing order as c_1, c_2, c_3 and c_4. Within the figure, it can be seen that compression level c_1 has the thickest frame, resulting in a low excess length of the PTL-c above the frame (Δ 10 μm). Thus, the resulting compression is the lowest. In contrast, c_4 has the thinnest frame and the largest PTL-c excess length (Δ 85 μm) which results in the highest compression.

The contact pressure distribution across the active area and the gasket area was determined with measuring films (types LLW, LW and MW, Prescale by Fujifilm). For this, the CCMs were replaced with the measuring films while the PTLs and the gaskets remained in the cell. Then, the contact force of 3 kN was applied at one stroke. The films were evaluated with software provided by Fujifilm.

Testing periphery.—The measurements were performed in a E100 test station by Greenlight Innovation. As a current source, a BCS 815 potentiostat (BioLogic) was used. For the analysis of the dried anodic product gas, the anode gas outlet was connected to a gas chromatograph (GC, 490 μGC System, Agilent). Helium was used as the carrier gas. The gas chromatograph is equipped with 5 Å mole sieve columns of 10 m length and a thermal conductivity detector. Prior to the measurement, the system was calibrated with known H$_2$ in O$_2$ mixtures.

As high hydrogen contents were expected at low current densities and high cathode pressures, the anode product gas was diluted with an additional flow of oxygen. The constant mass flow of 0.06 g min^{-1} ($N_{O_2}^{dilute}$ = 3.125 · 10^{-5} mol s^{-1}) was supplied with a mass flow controller (EL-flow Prestige, Bronkhorst).

The measured hydrogen content at the GC $\phi_{H_2}^{GC}$ is described with Eq. 1, where the evolved O$_2$ flux is equal to $N_{O_2}^{evolved} = \frac{i}{4 \cdot F}$, i is the applied current density and F is the Faraday constant.
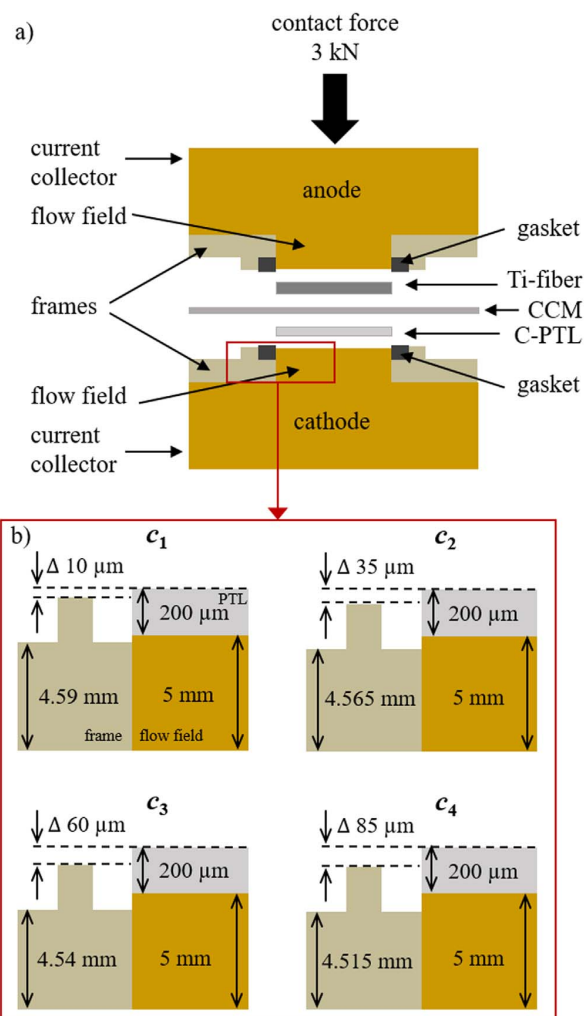

Figure 1. Schematic illustration of the 4 cm^2 cell in (a) and the functionality of different compression levels in b). Gaskets between the frame and the flow field are not shown for clarity in b). The compression is increasing from c_1 to c_4. The shown thicknesses and heights are not true to scale and refer to the uncompressed state. This scheme is published with the permission of Fraunhofer ISE.

$$\phi_{H_2}^{GC} = \frac{N_{H_2}^{cross}}{N_{O_2}^{evolved} + N_{O_2}^{dilute} + N_{H_2}^{cross}} \quad [1]$$

Solving Eq. 1 for the molar flux of permeated hydrogen $N_{H_2}^{cross}$ leads to Eq. 2. Then, the real hydrogen content $\phi_{H_2}^{real}$ is eventually calculated by Eq. 3.

$$N_{H_2}^{cross} = \frac{\phi_{H_2}^{GC}(N_{O_2}^{evolved} + N_{O_2}^{dilute})}{1 - \phi_{H_2}^{GC}} \quad [2]$$

$$\phi_{H_2}^{real} = \frac{N_{H_2}^{cross}}{N_{O_2}^{evolved} + N_{H_2}^{cross}} \quad [3]$$

Measurement protocol.—After assembly, the cell was mounted into the test station. Figure 2 shows a schematic summary of the
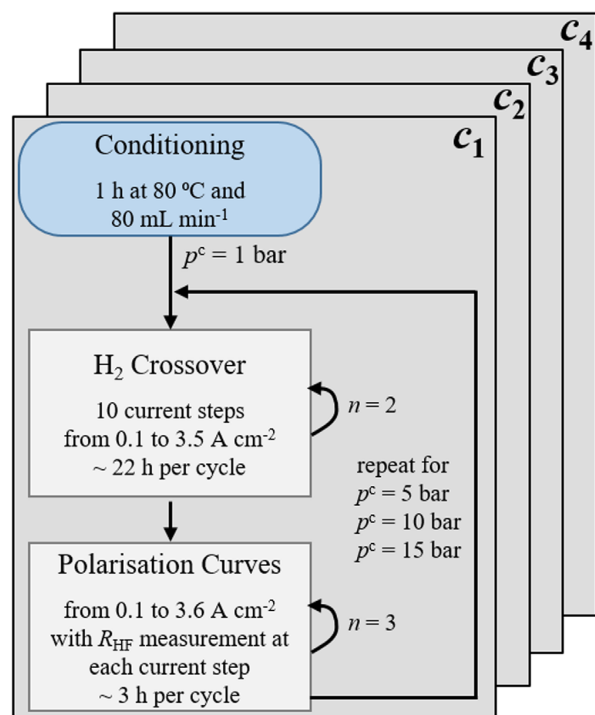
Figure 2. Summary of the used measurement protocol for each compression level, where n is the number of cycles.

applied measurement protocol for each compression level. Prior to starting the measurements, the cell was thermally conditioned without polarisation for 1 h at 80 °C and 80 ml min^{-1}. Then, the hydrogen crossover and the polarisation behaviour were measured at four different absolute cathode pressures (1 bar, 5 bar, 10 bar and 15 bar), whereas the anode pressure remained at 1 bar. The protocols are described in more detail in the following sections.

Hydrogen crossover.—The hydrogen crossover was evaluated by measuring the anodic hydrogen content with the GC. For this, a galvanostatic step profile was used. One measurement cycle consisted of ten current density steps (4 h at 0.1 A cm^{-2}, 3.5 h at 0.25 A cm^{-2}, 3 h at 0.5 A cm^{-2}, 2.5 h at 0.75 A cm^{-2}, 2 h at 1 A cm^{-2}, 2 h at 1.5 A cm^{-2}, 1.5 h at 2 A cm^{-2}, 1.5 h at 2.5 A cm^{-2}, 1 h at 3 A cm^{-2} and 1 h at 3.5 A cm^{-2}). The time intervals were chosen by using information from previous studies, until a constant hydrogen in oxygen signal was measured.[15,16,28] Due to low gas production rates, the holding time at low current densities is longer than at higher current densities.

Two cycles were performed at each cathode pressure. At $p^c = 1$ bar, an extra cycle was passed in order to purge the test station. At $p^c = 15$ bar the cycle started at 0.5 A cm^{-2} for maintaining the safety limits despite oxygen flushing.

Polarisation curves.—After the crossover measurements, polarisation curves were recorded from 0.01 A cm^{-2} to 3.6 A cm^{-2} in logarithmic current density steps until 2 A cm^{-2} and steps of 0.2 A cm^{-2} for higher current densities. The holding time was 10 s at each step. Each current step was followed by an electrochemical impedance measurement in order to determine the high frequency resistance R_{HF}. The frequency range was set from 10 kHz to 100 Hz and a respective current amplitude of 10% was applied. R_{HF} was obtained by interpolating the Nyquist plots at the intercept with the real axis.

This procedure was repeated twice. The average of the three cycles was used for further evaluation of the data. The measurement error was calculated by standard deviation.

Results and Discussion

Influence of compression level.—As already introduced above, the cell compression has consequences on the polarisation behaviour of PEM water electrolysis cells and on the material properties. For PEM fuel cells, it is already well known that the compression of the porous materials has negative consequences for the cell performance. The reduced porosity and increased tortuosity of the materials result in a limited mass transport towards the electrodes, which becomes visible in a mass transport dominated region of the fuel cells polarisation curve.[18,19,21,22,29,30]

Besides the impact of the external clamping pressure, it is known that mass transport limitations are also affected by the contact pressure distribution on the active area, which are in turn influenced by the flow field design.[31,32] Hence, the contact pressure distribution on the active cell area is evaluated first. The findings are then used to analyse the compression effect on the polarisation behaviour and on hydrogen crossover of the investigated PEM water electrolysis cells.

Contact pressure distribution.—As illustrated in Fig. 1, the compression levels c_1, c_2, c_3 and c_4 are achieved by different thicknesses of the cathodic isolation frame. We assume that the compression occurs mainly on the cathode side, since the frames were adjusted there and the carbon PTLs-c are highly compressible, especially compared to the titanium PTL-a used at the anode.

Figure 3 shows the resulting contact pressure distribution of the four compression levels. In general, most of the applied force is transferred over the active area for all compression levels. As expected, the thickest isolation frame c_1 shows the lowest overall contact pressure and the thinnest isolation frame c_4 has the highest contact pressure, and consequently the highest compression level. Additionally, most of the contact pressure acts on the lands of the flow fields for all compression levels, which results in low pressures in the channel areas ($\leqslant 1$ MPa). The resulting pressure differences between the lands and channel areas are increasing significantly with higher compression. For the highest compression level c_4, more than 25 MPa are measured at the maximum.

In this regard, it must be emphasized that the contact pressure distributions might be different during electrolysis, as the contact pressure measuring films were integrated into the dry cell, instead of CCMs, at ambient conditions. However, the results indicate that the cell materials are compressed more under the lands than at the channel areas. This means that the resulting strain within the Nafion membrane can be locally very high, leading to membrane deformation. For fully humidified Nafion 212 membranes at temperatures around 80 °C, a Young's modulus between 50 and 100 MPa is reported.[33] Assuming that a wet Nafion membrane is exposed to the same contact pressure distribution as indicated with the pressure measuring films, the resulting strain might be severe. At compression level c_4, the maximum stress of 25 MPa would translate to a maximum strain of 25 to 50% and a high local deformation. In contrast, the maximum stress of c_1 (~ 5 MPa) leads to a local strain of only 5 to 10%, which is essentially no deformation. A deeper analysis requires a more detailed investigation of the contact pressure distribution during electrolysis conditions and of the mechanical properties of wet Nafion membranes, which is beyond the scope of this work.

Moreover, it is expected that the porosity of the cathode catalyst layer is affected by the compression levels.[34] As explained earlier, the structural properties of the materials have an impact on the mass transport,[16,35] which is why a compression effect should be noticeable in the polarisation behaviour as well as in the hydrogen crossover. This is examined in the following sections.
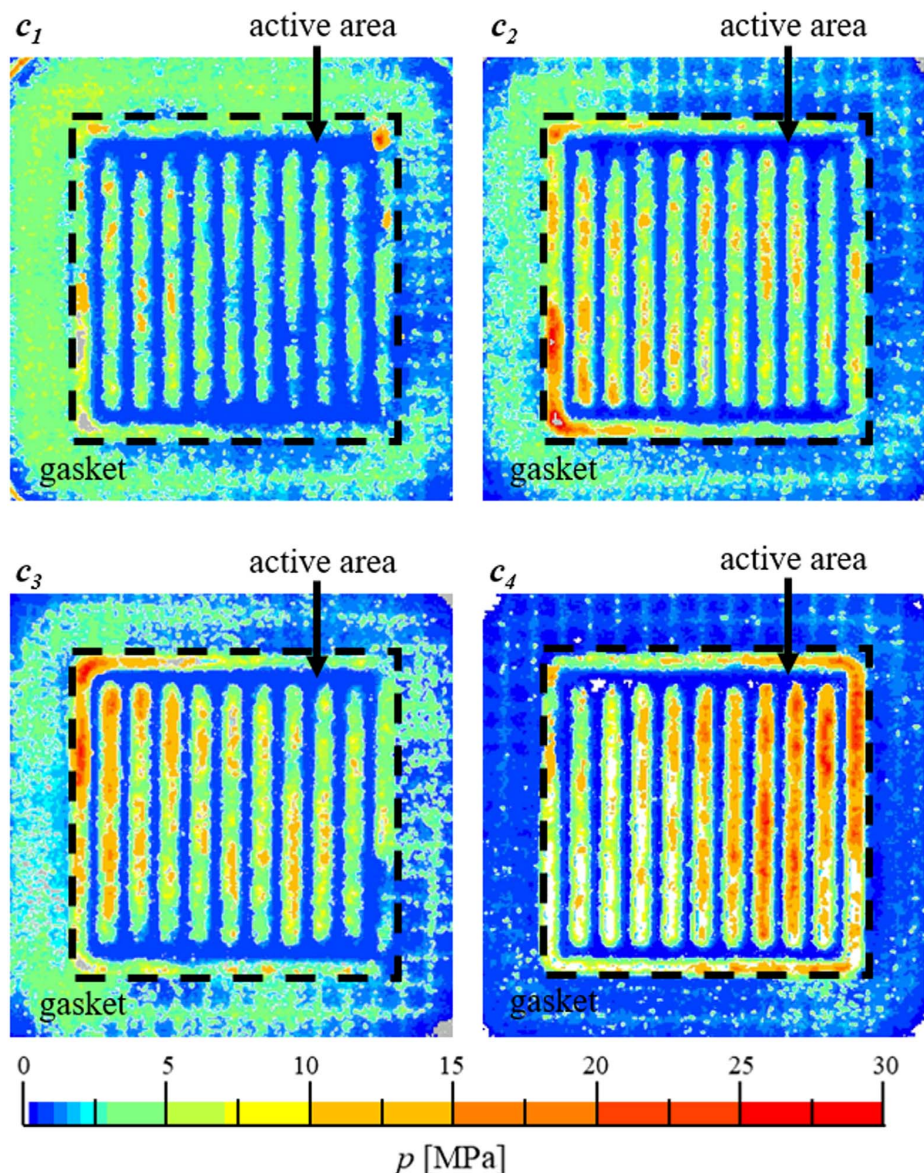
Figure 3. Pressure distribution across the active area and gasket for the four investigated compression levels c_1, c_2, c_3 and c_4 in increasing order.

Polarisation behaviour.—The influence of the compression level on the cell polarisation behaviour and key cell parameters is shown in Fig. 4. In Fig. 4a, the integral cell polarisation is displayed. The cell voltages decrease slightly with increasing compression level. The maximum cell voltage of all compression levels falls below 1.8 V and the deviation at 3.6 A cm^{-2} is only 30 mV.

Figure 4b shows the obtained R_{HF} values. It is assumed that R_{HF} describes the ohmic cell resistance and is mainly caused by the proton transport resistance of the membrane. It can be observed that an increase in current density leads to a small reduction of R_{HF}. This effect was already reported by others and can be explained by the reduction in resistance due to temperature increases with higher applied current densities.[36,37]

With growing compression, R_{HF} is decreasing. This can be explained by a better electric contact between the PTL-c and catalyst layer with increasing contact pressure. This was already reported by others[19,20,22,38] and by Stähler *et al.*[17] Although they have used a different setup, a resistance $R_{HF} = 58$ mΩ cm^2 is reported for their

highest compression level, which agrees well with the values of c_4 in this work.

In Fig. 5a, R_{HF} is shown for 1 A cm^{-2} and 3 A cm^{-2} as a function of compression. The reduction of R_{HF} with increasing current density can be seen here as well. The compression increase from c_1 to c_4 leads to a reduction of ~ 11 mΩ cm^2 at both current densities.

In the next step of the voltage loss analysis, the measured cell voltage is corrected by the ohmic potential drop according to Eq. 4. Figure 4c shows the resulting iR_{HF}-corrected curves.

$$U_{iR_{HF}-free} = U_{cell} - i \cdot R_{HF} \qquad [4]$$

The effect of the compression level on $U_{iR_{HF}-free}$ is more pronounced at higher current densities (zoom in Fig. 4c). The higher the compression level is, the higher the iR_{HF}-free voltage is as well. Thus, the compression level has an opposing effect on the iR_{HF}-free cell voltage than on the integral cell voltage. As the used material
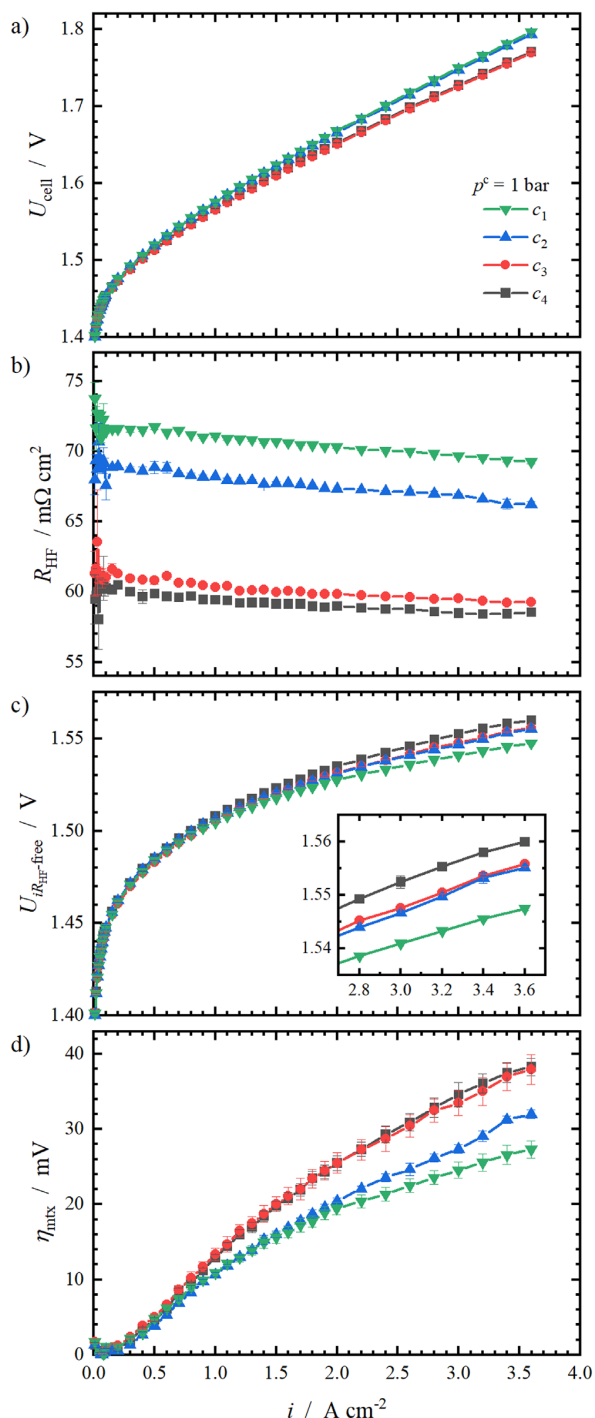
Figure 4. Deconvolution of the measured cell voltage at $p^c = 1$ bar for all four compression levels. The integral cell voltage is shown in (a), (b) shows the respective R_{HF}, (c) shows the resulting iR_{HF}-corrected cell voltages and (d) shows η_{mtx}.
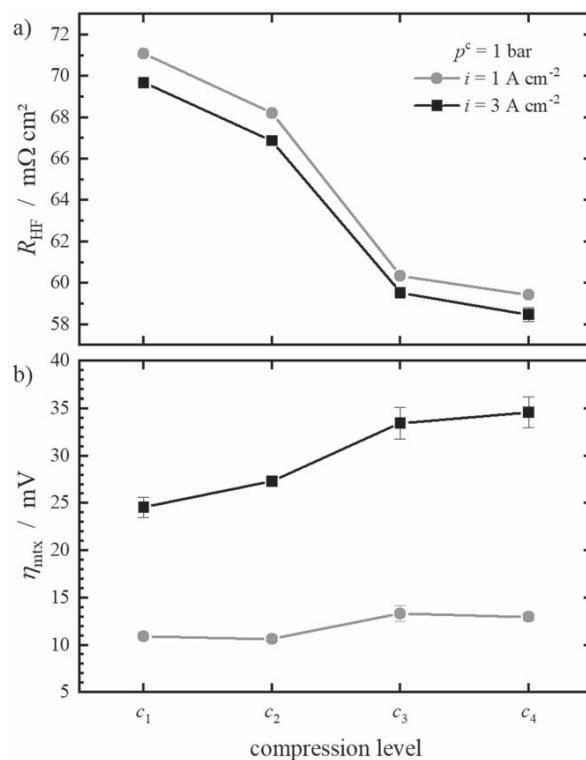

Figure 5. Dependence R_{HF} in a) and η_{mtx} in b) at 1 A cm^{-2} (light grey) and 3 A cm^{-2} (black) on the compression level at $p^c = 1$ bar.

the open circuit voltage $U_{cell,0}^{p^c=1\,bar}$ at 80 °C is calculated according to Nernst's equation (Eq. 5) and then subtracted from $U_{iR_{HF}-free}$ (Eq. 6). Assuming a reference pressure of $p_i^{\circ} = 1$ bar and that the evolved gases are saturated with water vapour ($p_{H_2O}^{sat} = 0.47$ bar[39]), a value of $U_{cell,0}^{p^c=1\,bar} = 1.169$ V is determined. The remaining overpotential η is assumed to be the sum of the activation overpotential η_{act} and other overpotentials such as mass transport losses η_{mtx}. The latter can be interpreted as a measure of quality for the removal of the two product gases and depends on the structural design of the electrodes.

$$U_{cell,0}^{p^c} = U_{cell,0}^{\circ} + \frac{RT}{2F} \cdot \ln\left(\frac{p_{H_2}}{p_{H_2}^{\circ}}\sqrt{\frac{p_{O_2}}{p_{O_2}^{\circ}}}\right) \qquad [5]$$

$$\eta = U_{iR_{HF}-free} - U_{cell,0}^{p^c} = \eta_{act} + \eta_{mtx} \qquad [6]$$

According to the Tafel analysis, the activation overpotential η_{act} can be obtained by fitting η against $\log(i)$ in its linear regime between 0.01 and 0.1 A cm^{-2}. The obtained Tafel slopes for the four investigated compression levels are quite close to one another, with values of 47.7 ± 0.9 mV dec^{-1} (Tafel plots are located in supplemental information—Fig. S1 available online at stacks.iop.org/JES/169/014502/mmedia). This implies that the kinetics are identical for all compression levels and consequently fail to explain the visible differences in $U_{iR_{HF}-free}$.

As a last step of the voltage loss analysis, η_{mtx} is shown in Fig. 4d. Here, clear indications for the divergences in iR_{HF}-free polarisation can be seen. With increasing current density, η_{mtx} rises. This was reported previously by others[35,37,38] and was also predicted by modelling.[40]

was the same in every cell, the differences in the iR_{HF}-corrected curves are not caused by ohmic losses of the membrane electrode assembly.

In order to explain the opposing trends between the integral and iR_{HF}-free cell voltage, a Tafel analysis can be performed. For this,

Moreover, η_{mtx} increases with increasing compression level. The effect of compression on η_{mtx} is more pronounced at higher current densities. In Fig. 5b, η_{mtx} at 1 A cm^{-2} and 3 A cm^{-2} is shown as a function of the compression level. At 1 A cm^{-2}, the effect of increased compression can barely be seen whereas at 3 A cm^{-2} the increase of ~ 10 mV from c_1 to c_4 is significant.

The effect of the compression level on the mass transport losses could be a result of changed structural properties of the cathode. The previously described structural changes of the PTL-c due to compression should also be true for the catalyst layer, in which the pores are even smaller. Perhaps, the diffusive pathways under the lands are completely different from the pathways in between the lands. As the pore volume is reduced, the transition of evolved, dissolved H$_2$ from the catalyst through the ionomer into the gas phase, is hindered.[16,34] Thus, the reduced permeability of both the PTL-c and catalyst layer, and the reduction of the surface between the pore space and the ionomer within the catalyst layer, could result in higher mass transport limitations within the more compressed cells than in less compressed cells. This eventually becomes visible in the mass transport losses (cf. Fig. 4d).[18,19,22]

This contrary effect on the cell parameters must be kept in mind when a PEM water electrolyser system is designed. Although high compressions lead to reduced ohmic losses, the mass transport losses increase. Thus, more than one cell parameter, such as low cell voltages or R_{HF}, should be considered for system design, and the trade-off between R_{HF} and η_{mtx} should be found.

Hydrogen crossover.—The anodic hydrogen content and the resulting hydrogen crossover fluxes at $p^c = 1$ bar as a function of the applied current density are shown in Fig. 6. Regarding the H$_2$ in O$_2$ content (Fig. 6a), it is observed that a safe operation begins at 0.25 A cm^{-2} (H$_2$ in O$_2$ content < 2% or 50% LEL[41]) and that the contents show a re-ascent with increasing current density. The latter finding was already seen by others.[9,17,28] In the re-ascending content region above 1 A cm^{-2}, the influence of the compression level becomes visible: the higher the compression level is, the higher is the resulting hydrogen content and the slope of the ascent.

Figure 6b shows the resulting hydrogen crossover fluxes calculated according to Eq. 2. Up to 1 A cm^{-2}, the fluxes of all compression levels are nearly identical and show a linear dependence on current density. In a previous study, Trinke *et al.*[14] have reported on this linear relationship with current density up to 1 A cm^{-2}. The dependence on current density can be explained with the super-saturation of water with evolved hydrogen.[14,18,42,43] Further, the slope is no longer linear and depends on the compression level at higher current densities. The combination of high compression and high currents leads to significant increases in $N_{H_2}^{cross}$. At the maximum current density of 3.5 A cm^{-2}, $N_{H_2}^{cross}$ of c_4 is more than the double of the lowest compression c_1 (1 mmol s^{-1} m^{-2} vs 0.4 mmol s^{-1} m^{-2}).

As mentioned previously, not only the porosity of the PTL-c and the catalyst layer is reduced with increasing compression, but also the surface between the ionomer and pore volume is reduced. Especially under the lands, the H$_2$ removal from the active sites into the free pore space is hindered and occurs mainly in plane.[34] This results in a higher dissolved gas concentration and accordingly, in a higher hydrogen crossover flux.[34] This effect might be comparable to an ionomer variation within the catalyst layer. Trinke *et al.*[16] and Bernt *et al.*[9] varied the ionomer content with the cathode catalyst layer which translated into a reduction in pore space and a thickening of the ionomer film surrounding the catalyst particles with increasing ionomer content. This eventually results in higher mass transport limitations leading to higher dissolved hydrogen concentrations, enhanced hydrogen crossover fluxes and increased η_{mtx}.

To summarize the section of the compression impact at ambient pressure conditions, the results of the polarisation curves and of the crossover measurements agree well with each other and with the
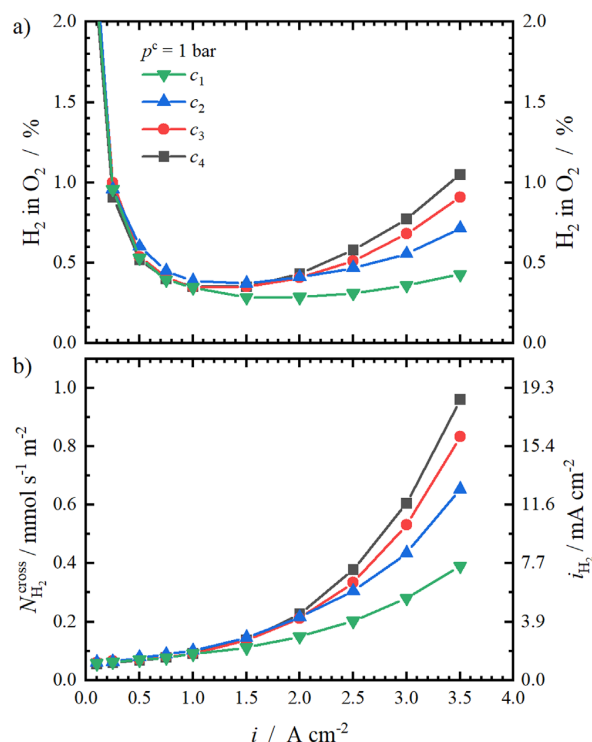

Figure 6. Current dependence of H$_2$ in O$_2$ content for the four investigated compression levels at $p^c = 1$ bar is shown in (a). In (b), the resulting anodic hydrogen flux $N_{H_2}^{cross}$ and the permeation current density equivalent $i_{H_2} = 2F \cdot N_{H_2}^{cross}$ is displayed.

work of Stähler *et al.*[17] The results indicate that the enhanced compression affects the mass transport at the cathode side. This leads to limitations in hydrogen removal, which becomes visible in higher mass transport voltage losses and in higher hydrogen crossover. Although the compression has a positive effect on the overall cell voltage, these contrary effects need to be considered in the system design.

Influence of cathode pressure.—In the first part of this study, the findings of Stähler *et al.*[17] were validated successfully in a different cell setup. Therefore, the discussed compression effects are qualitatively valid with different cell designs. However, the quantitative course is affected by the different cell designs.

In the next part of this study, the impact of enhanced cathode pressure on top of the compression levels was investigated. The evaluation of the cross-relationships between compression and gas pressure is necessary for gaining an extensive knowledge on the electrochemical and gas transport properties in PEM water electrolysers.

Polarisation behaviour.—For the evaluation of the cathode pressure dependence of the cell voltage, the cell voltage was analysed for different pressures ($p^c = 1$ bar; 5 bar; 10 bar; 15 bar). Since the pressure dependencies are similar for each compression level, the cell voltage analysis shown in Fig. 7 is performed exemplarily for c_4. The corresponding figures for c_1, c_2 and c_3 are shown in the Supplemental Information (Figs. S2, S3 and S4).

Figure 7a shows the measured cell voltage for the named pressures using c_4. It can be observed that the cell voltage is higher with increasing cathode pressures. This agrees well to the reversible cell potential according to Nernst's equation. In Fig. 7b, the respective R_{HF} are shown. As in the previous section, R_{HF} decreases with increasing i at each pressure. Further, R_{HF} is the lowest at
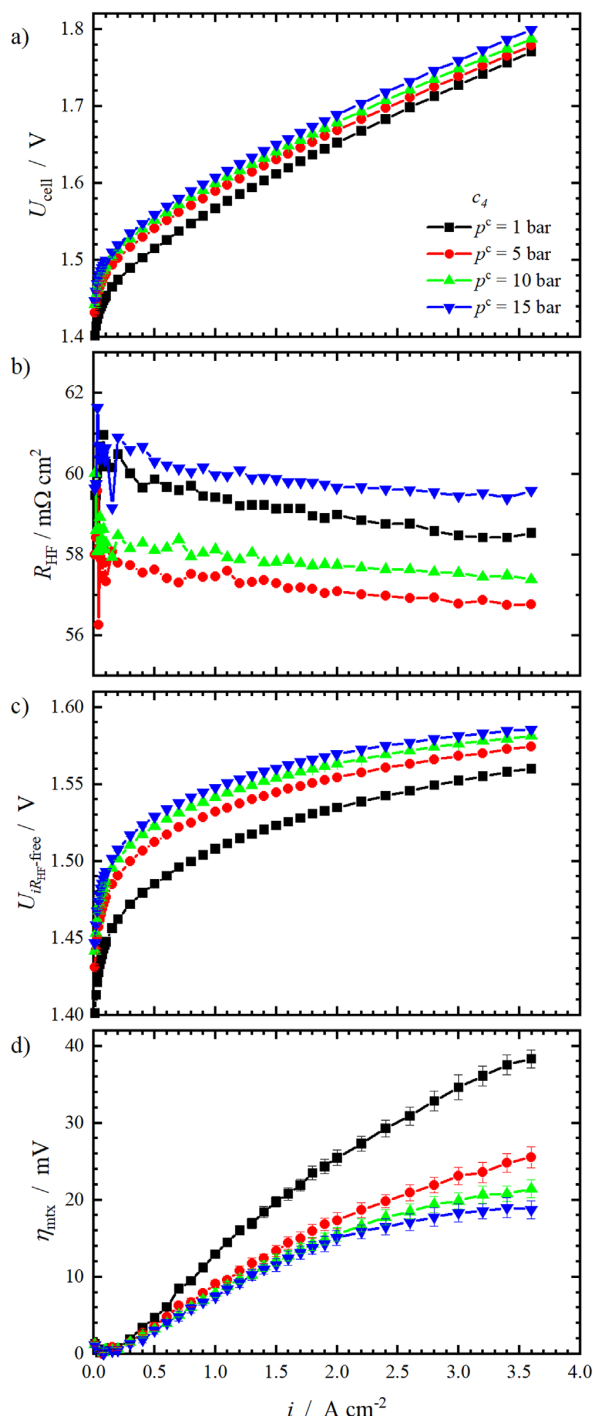
Figure 7. Deconvolution of the measured cell voltage $p^c = 1$ bar, 5 bar, 10 bar and 15 bar for compression level c_4. The integral cell voltage is shown in (a), (b) shows the respective R_{HF}, (c) shows the resulting iR_{HF}-corrected cell voltages and d) shows η_{mtx}.

$p^c = 5$ bar and the highest for $p^c = 15$ bar, which is also true for the other compression levels (cf. Figs. S2, S3 and S4). This finding will be discussed in more detail at a later point of this section.

From the integral cell voltage and R_{HF}, $U_{iR_{HF}-free}$ is calculated and shown in Fig. 7c. Here, the pressure dependence of the voltage

according to Nernst can be seen as well. For the further separation of the overpotentials according to the procedure described previously, the open circuit voltage at the respective cathode pressure levels were calculated according to Eq. 5 and subtracted from $U_{iR_{HF}-free}$. The purpose of this correction is to avoid an incorrect mapping of the increased reversible cell potentials at elevated cathode pressures to the mass transport losses (cf. Nernst's Eq. 5).

A further analysis of η according to Tafel reveals that the Tafel slopes of all measurements coincide with values of 47.9 ± 0.5 mV dec^{-1}. The respective Tafel plots of all compression levels and pressures are shown in Fig. S1. Hence, neither a dependence of the compression level nor of the cathode pressure on the cell kinetics can be identified.

As a last step of the voltage loss analysis, η_{mtx} was calculated and displayed in Fig. 7d. As in the previous section, η_{mtx} rises when the current density increases. Further, η_{mtx} decreases with enhanced cathode pressure. This positive effect of enhanced pressure on η_{mtx} was already reported by others.[36,40]

In order to compare and discuss the pressure influence on key cell parameters (R_{HF} and η_{mtx}) together with the impact of compression, R_{HF} and η_{mtx} at 3 A cm^{-2} are shown as a function of cathode pressure in Fig. 8. In Fig. 8a, the aforementioned positive effect of enhanced compression on R_{HF} is visible again. This is due to lower interfacial contact resistances with increasing compression[6,19] and applies for all pressures.

As mentioned previously, R_{HF} shows a nonlinear relation with p^c. For all compression levels, R_{HF} is the lowest at $p^c = 5$ bar. To the best of our knowledge, this was not observed and reported before.

We assume that the contact pressure distribution on the lands and at the channel areas plays an essential role for the nonlinearity of R_{HF}. As shown in a previous section, the contact pressure on the lands is far higher than in between (cf. Fig. 3). Following from this, we propose the following hypotheses for the nonlinearity of R_{HF} with increasing cathode pressure.

First, the structural properties of the cathode might be a function of both, the contact pressure and the cathode pressure. In a previous work of Schuler *et al.*[37] the influence of the PTL structure on the electrochemical performance of PEM electrolysis cells was investigated. Qualitatively, they found that R_{HF} using highly porous PTLs is higher than with low porosities, since the contact resistances of the catalyst layer-PTL interface rise with increasing porosity. When the porosity of a highly compressed carbon PTL-c is considered to be lower than of a less compressed PTL-c, the same trend is observed in this work. Moreover, we assume that the PTL-c porosity between the lands is higher than at the lands, because the compression force acts mainly on the lands of the flow field. Since the applied cathode pressure is far lower than the contact pressure resulting on the lands, we believe that only the PTL-c areas at the channel areas can be affected by the cathode pressure. Therefore, a slight increase in the cathode pressure might lead to reduced interfacial resistances which would result in lower R_{HF}. In contrast, too high cathode pressures might enlarge the pore space again, leading to a contrary effect.

The second proposed hypothesis addresses the pressure impact on the entire membrane electrode assembly. It is logical that an increase in cathode pressure acts through the membrane to the anode catalyst layer,[44] which could change the contact resistances on the anode side. In order to examine this hypothesis, we conducted a further experiment in which R_{HF} was measured at various symmetric and asymmetric pressure conditions. The experiment has shown that an increase in anode pressure without an increase in cathode pressure ($p^a = 5$ bar | $p^c = 1$ bar) leads to higher R_{HF} than at ambient pressure ($p^a = p^c = 1$ bar). However, the measurement of R_{HF} at $p^a = p^c = 5$ bar revealed similar values than at $p^a = 1$ bar | $p^c = 5$ bar. From this, we conclude that the anodic pressure dependence of R_{HF} appears to be different than on the cathode side. Perhaps, the membrane and the cathode catalyst layer are deforming more into the channel areas of the cathode flow field, leading to a reduced contact area when the anode pressure is increased. This might result

in higher R_{HF}. Possibly, the more rigid titanium PTL-a on the anode prevents the membrane deformation into the channels on this side and thus, the contact resistances between the PTL and the catalyst layer decrease only, when the pressure comes from the cathode side.

As a third hypothesis we propose that the membrane itself might suffer from compression. It was shown previously that the compression of Nafion membranes leads to changes in its nanostructure, reduces the membrane thickness and lowers its proton conductivity.[45–47] In combination with the inhomogeneous thickness distribution within the active area, the resulting R_{HF} might be affected.

Moreover, deviations in temperature can also lead to changes in e. g. proton conductivity and of course, other explanations may apply. Probably, a mixture of multiple hypotheses will explain the nonlinearity of R_{HF}. The fact that this effect was not reported yet can be a result of several aspects, such as the covered pressure range, the used membrane thickness or the cell setup. Further studies are necessary to elucidate this effect.

Besides R_{HF}, Fig. 8 also includes η_{mtx} of all compression levels at 3 A cm^{-2} as a function of cathode pressure. Using compression level c_4 at ambient pressure results in the highest η_{mtx} ($\sim$ 35 mV) whereas c_1 at $p^c = 15$ bar results in the lowest value ($\sim$ 16 mV).

Further, there are two observable trends for η_{mtx}. First, η_{mtx} rises with enhanced compression level at each investigated pressure. Second, η_{mtx} decreases with increasing cathode pressure. The former was already seen in the previous section in which the compression dependency of η_{mtx} was discussed. The latter is a result of the logarithmic course of the cathodic half-cell potential $\Delta U_{H_2}^c$, which can be seen from Nernst's equation for the cathodic half-cell reaction (Eq. 7).

$$\Delta U_{H_2}^c = U_{H_2}^\bullet + \frac{RT}{2F} \cdot \ln\left(\frac{c_{H_2}}{c_{H_2}^{sat}}\right) \qquad [7]$$

The dissolved hydrogen concentration c_{H_2} increases with the applied current density, whereas the hydrogen saturation concentration $c_{H_2}^{sat}$ is a function of the hydrogen pressure and rises with the hydrogen pressure. Since the half-cell potential increases logarithmically with the hydrogen concentration c_{H_2}, the mass transport losses decrease at elevated hydrogen pressures.

In summary, the increases in compression and cathode pressure show contrary effects on η_{mtx}. An increased cell compression leads to higher mass transport losses, whereas higher cathode pressure reduces them.

Hydrogen crossover.—In a previous section we have seen that an enhanced compression of PEM water electrolysis cells leads to increased H$_2$ in O$_2$ contents at high current densities. This may be explained by either one or by both of the following effects: First, the pores within the PTL-c and catalyst layer are diminishing with enhanced compression, which results in lower gas permeability and hence, worse gas transport properties. Second, the transition of the dissolved hydrogen gas into the gas phase is hindered, because the surface area between the ionomer and the pores is reduced when the compression is increased.

The first effect depends on the pressure. According to Darcy's law, the gas transport within the porous media is improved at higher gas pressures. Hence, an increase in cathode pressure should counteract the worse gas transport coming from high compressions. If the enhancement of gas pressure due to gas transport within the porous media is dominating, increased cathode pressures should improve the gas transport. Consequently, the increase in crossover at high current densities should be reduced at elevated cathode pressures. However, the opposite effect is reported in literature.[14,15]

In contrast, the second explanation describes that the structural change of the porous media with increasing compression leads to higher transfer resistances of the produced gas from the dissolved
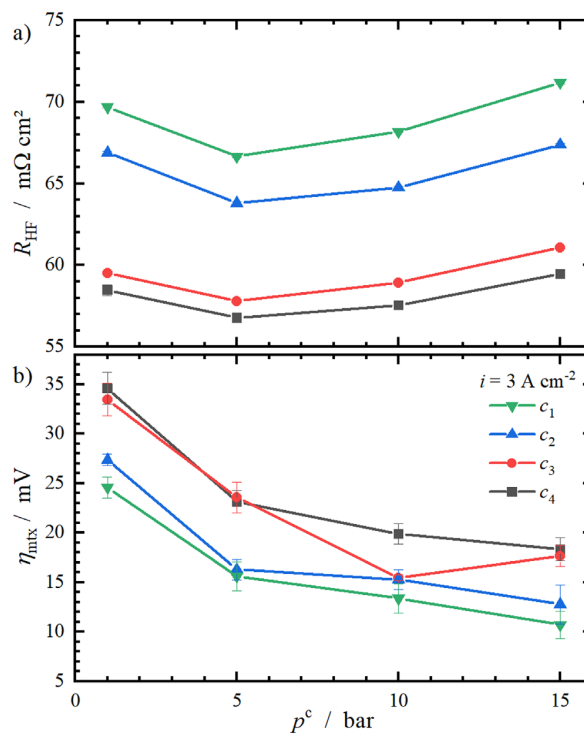

Figure 8. Dependence of η_{mtx} and R_{HF} at 3 A cm^{-2} on the cathodic pressure p^c.

into the gaseous state. This is explained by the fact that less surface area between the ionomer and pore space is available for the gas transition, when the compression is higher. Thereby, the diffusion path of the dissolved gases through the ionomer becomes longer. As a result, the transfer resistances increase with compression. Thus, if this effect is dominating, it is assumed that the crossover increase with current density will not be reduced at high compression levels in combination with enhanced cathode pressures.[14]

On account of this, we investigated the effect of elevated cathode pressures on top of the compression levels in a next step. In Fig. 9, the H$_2$ in O$_2$ contents of all compression levels at elevated cathode pressures and the resulting hydrogen crossover fluxes are shown. Please refer to Fig. 6 for ambient conditions.

Regarding the hydrogen contents, an increase in compression level results in enhanced H$_2$ in O$_2$ contents at every pressure level. At $p^c = 5$ bar (Fig. 9a), the previously observed increase of the hydrogen concentration at higher current densities (cf. Fig. 6a) is only present for the two higher compression levels c_3 and c_4. The other two compression levels approach a more hyperbolic trend. Since the H$_2$ in O$_2$ contents stagger around 2 %, safety precautions must be taken. A further increase in cathode pressure leads to even higher H$_2$ in O$_2$ contents. For $p^c = 10$ bar and $p^c = 15$ bar, the re-ascent in concentrations at higher current densities is not present anymore. The resulting high anodic hydrogen concentrations are not only relevant in terms of safety, but also in terms of faradaic efficiency losses.

The data presented in this work was measured in a specific experimental setup. In a previous study by Trinke *et al.*,[14] the importance of the experimental setup on the quantitative results was already highlighted. Slight changes within the setup can therefore lead to other quantitative results. For example, Bernt *et al.*[9] measured the H$_2$ in O$_2$ content at 80 °C and asymmetric pressure conditions in a similar system as used in this work (Nafion 212, PTL-a made of titanium, PTL-c made of carbon). However, their H$_2$
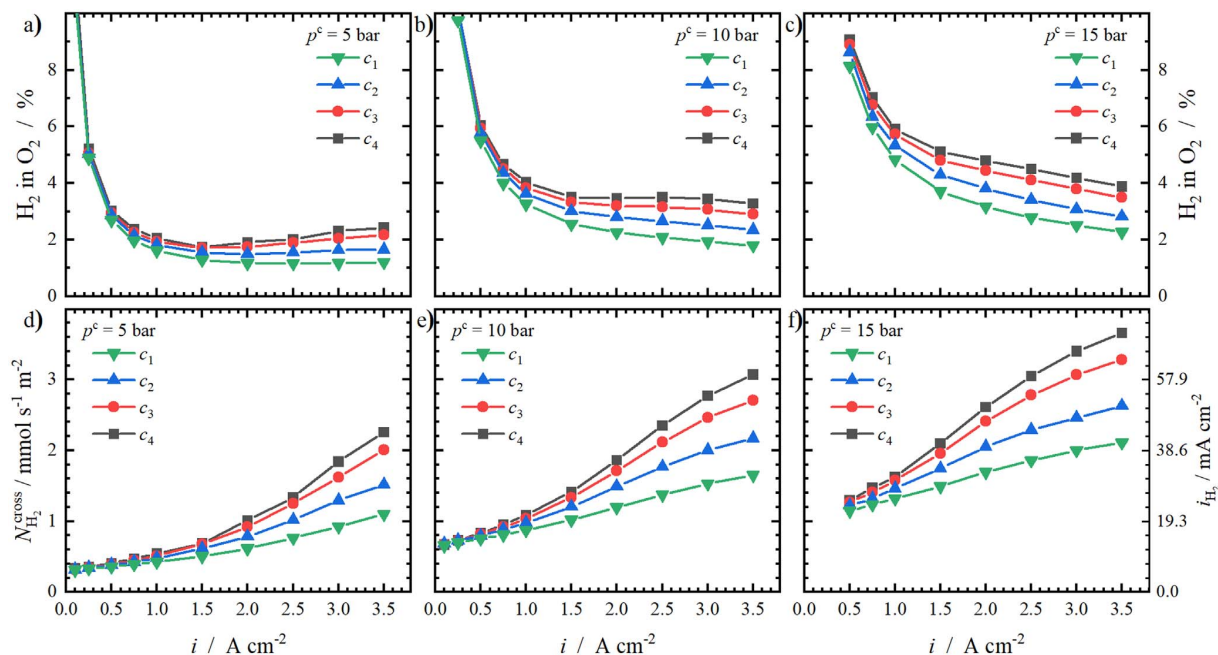
Figure 9. Current dependence of H_2 in O_2 content at (a) $p^c = 5$ bar, (b) $p^c = 10$ bar, (c) $p^c = 15$ bar and the hydrogen crossover flux $N_{H_2}^{cross}$ at (d) $p^c = 5$ bar, (e) $p^c = 10$ bar, f) $p^c = 15$ bar. The current density equivalent i_{H_2} to $N_{H_2}^{cross}$ can be read from the right ordinate in (f).

in O_2 contents are much lower than those measured in this work. These differences highlight that the chosen experimental setup has severe consequences on the quantity of results, although the qualitative trends are comparable. Hence, a careful and thorough report of all experimental conditions is inevitable for a meaningful comparison of data in order to develop a comprehensive understanding of hydrogen crossover.

The resulting hydrogen crossover fluxes from the H_2 in O_2 contents are calculated according to Eq. 2. The respective fluxes at elevated cathode pressures are shown as a function of current density in Figs. 9d–9f. Clearly, the relation between the hydrogen flux and the current is nonlinear for every compression and pressure level. At low current densities, the curves are approaching one another. The extrapolation of the converging curves to $i = 0$ A cm^{-2} equals to the expected pure diffusive hydrogen crossover at the corresponding cathode pressure. This basic value rises with the applied pressure because the hydrogen concentration gradient through the membrane increases and results in a higher driving force.[16]

At higher current densities, the impact of the compression level becomes visible again. According to the discussed hydrogen contents, the increase of the compression level is followed by higher hydrogen crossover fluxes. At $p^c = 5$ bar, for example, $N_{H_2}^{cross}$ of c_4 is more than the double than of c_1 (2.25 mmol s^{-1} m^{-2} and 1.10 mmol s^{-1} m^{-2}, respectively).

Moreover, the absolute crossover gain with the applied current density increases with rising cathode pressures. For example, the crossover gain between 0.5 A cm^{-2} and 3.5 A cm^{-2} for the highest compression level c_4 at atmospheric conditions is 0.89 mmol s^{-1} m^{-2} and increases with pressure: 1.86 mmol s^{-1} m^{-2} (at 5 bar), 2.24 mmol s^{-1} m^{-2} (at 10 bar) and 2.37 mmol s^{-1} m^{-2} (at 15 bar). In contrast, the respective crossover gains at the lowest compression level c_1 with cathode pressure are much lower (0.29 mmol s^{-1} m^{-2} (at 1 bar), 0.74 mmol s^{-1} m^{-2} (at 5 bar), 0.90 mmol s^{-1} m^{-2} (at 10 bar) and 0.96 mmol s^{-1} m^{-2} (at 15 bar)), but still rise with the cathode pressure.

In summary, the effect of the compression level on hydrogen crossover is amplified by elevated cathode pressures. This observation contradicts a transport limitation in the gas phase, because the

gas transport is improved at higher pressures. However, a reduction in hydrogen crossover is not observed but it rather becomes more pronounced. This implies that the steady increase in the dissolved hydrogen concentration explains the progressing increase of hydrogen crossover with greater compression and cathode pressure to a better extent. Furthermore, the resulting anodic hydrogen contents indicate that the operating pressure has a greater impact on the faradaic efficiency than the compression level. A more detailed comparison with regards to the specific energy demand of the usable hydrogen amount at each compression and pressure level is given in the Supplemental Information.

Conclusions

In this study, the cell compression and cathode pressure were varied in order to examine their influence on the cell polarisation behaviour and on hydrogen crossover on pristine materials in a PEM water electrolysis cell.

It was shown that an enhanced cell compression reduces the obtained cell voltages due to lowered interfacial contact resistances. However, a detailed cell voltage analysis revealed that the mass transport losses increase with higher compressions. These mass transport restrictions also become visible in increased H_2 in O_2 contents, which are increasing at higher current densities at ambient pressure. This is explained with a reduced pore volume in the carbon PTL-c and cathode catalyst layer at higher compressions. In terms of the catalyst layer, the reduction of the surface area between the ionomer and the pore space leads to a restricted removal of dissolved hydrogen and higher dissolved hydrogen concentrations. Consequently, the hydrogen concentration gradient across the membrane increases and results in a higher hydrogen crossover.

Furthermore, the impact of enhanced cathode pressures in addition to the compression was evaluated. In terms of the polarisation behaviour, the results show a contrary effect of the two parameters on cell voltage parameters. As a consequence of Nernst's equation, the cell voltage rises with increased pressures, whereas higher compressions are reducing the cell voltage. However, the pressure increase is also lowering the mass transport losses. Moreover, this study shows a first report on the pressure

dependence of R_{HF} with an optimal value at medium cathode pressures of $p^c = 5$ bar. Several hypotheses are proposed to explain this observation. Certainly, further investigations on the pressure dependence of R_{HF} are needed to understand this phenomenon.

With regards to hydrogen crossover, it was shown that the pressure increase amplifies the compression influence. Especially at high current densities, the combination of high cathode pressures and high compressions leads to explosive gas mixtures due to high hydrogen crossover fluxes. As mentioned previously, the restricted removal of hydrogen caused by the reduced porosity in the catalyst layer leads to higher dissolved hydrogen concentrations. This increases the driving force for hydrogen crossover.

The presented findings highlight the importance of the structural design of the PTL-c and catalyst layer. Regarding the electrochemical parameters, both layers should be designed in such a way that the interfacial resistances are small, while the mass transport losses are also kept to a minimum. These improvements would lead to reduced cell voltages and lower hydrogen crossover. Besides the structural changes of cell materials, the cell design itself might also be optimized. Other flow field designs, for example, might help to achieve the improvements.

The findings presented here offer a systematic analysis of hydrogen crossover in PEM water electrolysis cells. Since the resulting anodic hydrogen contents measured in our setup lead to a reduced hydrogen output and exceed technical safety limits, improvements are necessary. The structural optimization of the cell materials (e. g. catalyst layer structure) might improve both aspects. However, other strategies such as the integration of a recombination catalyst in the cell could also be a possibility to meet the demands. Both suggestions should be investigated in future in order to generate a comprehensive understanding of hydrogen crossover and to propose an optimal design for PEM water electrolysers.

ORCID

Agate Martin https://orcid.org/0000-0003-4673-1135
Patrick Trinke https://orcid.org/0000-0002-0935-5321
Andrea Stähler https://orcid.org/0000-0002-4058-6056
Fabian Scheepers https://orcid.org/0000-0001-6243-4291
Boris Bensmann https://orcid.org/0000-0001-8685-7192
Richard Hanke-Rauschenbach https://orcid.org/0000-0002-1958-307X

References

1. B. Bensmann, R. Hanke-Rauschenbach, and K. Sundmacher, *Int. J. Hydrogen Energ.*, **39**, 49 (2014).
2. P. Millet, *Electrochemical Energy Storage for Renewable Sources and Grid Balancing* (Elsevier, Amsterdam) (2015).
3. S. A. Grigoriev, P. Millet, S. V. Korobtsev, V. I. Porembskiy, M. Pepic, C. Etievant, C. Puyenchet, and V. N. Fateev, *Int. J. Hydrogen Energ.*, **34**, 5986 (2009).
4. M. Schalenbach, M. Carmo, D. L. Fritz, J. Mergel, and D. Stolten, *Int. J. Hydrogen Energ.*, **38**, 14921 (2013).
5. M. Schalenbach, *Int. J. Hydrogen Energ.*, **41**, 729 (2016).
6. K. Ayers, N. Danilovic, R. Ouimet, M. Carmo, B. Pivovar, and M. Bornstein, *Annu. Rev. Chem. Biomol. Eng.*, **10**, 219 (2019).
7. U. Babic, M. Suermann, F. N. Büchi, L. Gubler, and T. J. Schmidt, *J. Electrochem. Soc.*, **164**, F387 (2017).
8. M. Carmo, D. L. Fritz, J. Mergel, and D. Stolten, *Int. J. Hydrogen Energ.*, **38**, 4901 (2013).
9. M. Bernt, J. Schröter, M. Möckl, and H. A. Gasteiger, *J. Electrochem. Soc.*, **167**, 124502 (2020).
10. H. Ito, N. Miyazaki, M. Ishida, and A. Nakano, *Int. J. Hydrogen Energ.*, **41**, 20439 (2016).
11. M. Schalenbach and D. Stolten, *Electrochim. Acta*, **156**, 321 (2015).
12. M. Schalenbach, T. Hoefner, P. Paciok, M. Carmo, W. Lueke, and D. Stolten, *J. Phys. Chem. C*, **119**, 25145 (2015).
13. P. Trinke, B. Bensmann, S. Reichstein, R. Hanke-Rauschenbach, and K. Sundmacher, *J. Electrochem. Soc.*, **163**, F3164 (2016).
14. P. Trinke, B. Bensmann, and R. Hanke-Rauschenbach, *Int. J. Hydrogen Energ.*, **42**, 14355 (2017).
15. P. Trinke, P. Haug, J. Brauns, B. Bensmann, R. Hanke-Rauschenbach, and T. Turek, *J. Electrochem. Soc.*, **165**, F502 (2018).
16. P. Trinke, G. P. Keeley, M. Carmo, B. Bensmann, and R. Hanke-Rauschenbach, *J. Electrochem. Soc.*, **166**, F465 (2019).
17. M. Stähler, A. Stähler, F. Scheepers, M. Carmo, W. Lehnert, and D. Stolten, *Int. J. Hydrogen Energ.*, **45**, 4008 (2020).
18. R. Omrani and B. Shabani, *Electrochim. Acta*, **377**, 138085 (2021).
19. S. H. Frensch, A. C. Olesen, S. S. Araya, and S. K. Kær, *Electrochim. Acta*, **263**, 228 (2018).
20. E. Borgardt, L. Giesenberg, M. Reska, M. Müller, K. Wippermann, M. Langemann, W. Lehnert, and D. Stolten, *Int. J. Hydrogen Energ.*, **44**, 23556 (2019).
21. E. Espinoza, M. Andersson, J. Yuan, and B. Sundén, *Int. J. Energy Res.*, **39**, 1528 (2015).
22. W. R. Chang, J. J. Hwang, F. B. Weng, and S. H. Chan, *J. Power Sources*, **166**, 149 (2007).
23. A. Stähler, M. Stähler, F. Scheepers, M. Carmo, and D. Stolten, *Int. J. Adhes. Adhes.*, **98**, 102473 (2020).
24. M. Stähler, A. Stähler, F. Scheepers, M. Carmo, and D. Stolten, *Int. J. Hydrogen Energ.*, **44**, 7053 (2019).
25. C. Liu, M. Carmo, G. Bender, A. Everwand, T. Lickert, J. L. Young, T. Smolinka, D. Stolten, and W. Lehnert, *Electrochem. Commun.*, **97**, 96 (2018).
26. C. Liu et al., *Adv. Energy Mater.*, **11**, 2002926 (2021).
27. Fraunhofer Institute for Solar Energy Systems ISE, *Fraunhofer ISE—Annual Report 2020/2021* (Freiburg, Germany) (2021).
28. C. Klose, P. Trinke, T. Böhm, B. Bensmann, S. Vierrath, R. Hanke-Rauschenbach, and S. Thiele, *J. Electrochem. Soc.*, **165**, F1271 (2018).
29. J. Ge, A. Higier, and H. Liu, *J. Power Sources*, **159**, 922 (2006).
30. W. Lee, C.-H. Ho, J. W. van Zee, and M. Murthy, *J. Power Sources*, **84**, 45 (1999).
31. R. Taccani and N. Zuliani, *Int. J. Hydrogen Energ.*, **36**, 10282 (2011).
32. H. A. Dhahad, W. H. Alawee, and A. K. Hassan, *Renewable Energy Focus*, **30**, 71 (2019).
33. A. Kusoglu, M. H. Santare, A. M. Karlsson, S. Cleghorn, and W. B. Johnson, *J. Polym. Sci. B Polym. Phys.*, **46**, 2404 (2008).
34. P. J. Kim, C. Lee, J. K. Lee, K. F. Fahy, and A. Bazylak, *J. Electrochem. Soc.*, **167**, 124522 (2020).
35. M. Bernt and H. A. Gasteiger, *J. Electrochem. Soc.*, **163**, F3179 (2016).
36. M. Suermann, T. J. Schmidt, and F. N. Büchi, *Electrochim. Acta*, **211**, 989 (2016).
37. T. Schuler, T. J. Schmidt, and F. N. Büchi, *J. Electrochem. Soc.*, **166**, F555 (2019).
38. M. Suermann, K. Takanohashi, A. Lamibrac, T. J. Schmidt, and F. N. Büchi, *J. Electrochem. Soc.*, **164**, F973 (2017).
39. L. Haar, J. S. Gallagher, and G. S. Kell, *NBS/NRC Steam Tables* (CRC Press, Boca Raton, FL) (1984).
40. G. Schmidt, M. Suermann, B. Bensmann, R. Hanke-Rauschenbach, and I. Neuweiler, *J. Electrochem. Soc.*, **167**, 114511 (2020).
41. H. Janssen, J. C. Bringmann, B. Emonts, and V. Schroeder, *Int. J. Hydrogen Energ.*, **29**, 759 (2004).
42. K. Kikuchi, A. Ioka, T. Oku, Y. Tanaka, Y. Saihara, and Z. Ogumi, *J. Colloid Interface Sci.*, **329**, 306 (2009).
43. K. Kikuchi, Y. Tanaka, Y. Saihara, M. Maeda, M. Kawamura, and Z. Ogumi, *J. Colloid Interface Sci.*, **298**, 914 (2006).
44. E. Borgardt, O. Panchenko, F. J. Hackemüller, J. Giffin, M. Bram, M. Müller, W. Lehnert, and D. Stolten, *J. Power Sources*, **374**, 84 (2018).
45. A. Kusoglu, M. Calabrese, and A. Z. Weber, *ECS Electrochem. Lett.*, **3**, F33 (2014).
46. A. Kusoglu, A. Hexemer, R. Jiang, C. S. Gittleman, and A. Z. Weber, *J. Membr. Sci.*, **421-422**, 283 (2012).
47. A. Kusoglu, B. L. Kienitz, and A. Z. Weber, *J. Electrochem. Soc.*, **158**, B1504 (2011).

4.2 Hydrogen Crossover at High Current Densities

For the investigation of the effect of high current densities on hydrogen crossover (research question 2) and the additional increase of the cathode pressure (research question 3), a respective study was designed. The results are published in a peer-reviewed article entitled "Hydrogen Crossover in PEM Water Electrolysis at Current Densities up to $10\,\mathrm{A\,cm^{-2}}$" (*J. Electrochem. Soc.* 169(9):094507, 2022). The article follows these introductory paragraphs on the concept and key findings of the study.

The experimental study is performed with a standard PEM-WE cell without modifications. In order to enable the high current densities up to $10\,\mathrm{A\,cm^{-2}}$ without reaching critical cell voltages, a CCM based on a thin Nafion™ 212 membrane is used. The cell is investigated with regard to its electrical performance and hydrogen crossover characteristics during electrolysis at ambient and enhanced cathode pressures.

The findings at ambient pressure provide first experimental indications of a currently unknown functional relation between the hydrogen crossover flux and the high applied current density. Generally, it is observed that the hydrogen crossover flux increases over the entire current density range. However, the slope of the flux passes through multiple regions, starting at a rather linear growth at low currents, to a stronger than linear growing region, which flattens at high current densities above $5\,\mathrm{A\,cm^{-2}}$. This pass through the various slopes is observed at increased cathode pressures as well.

The analysis of the data reveals that commonly used model approaches, which are based almost exclusively on diffusion, are insufficient to explain the transition between the slopes of the hydrogen crossover flux with increasing current density. Therefore, it is suggested that the diffusion of dissolved hydrogen from the cathode to the anode is no longer the dominating transport mechanism in the high current density regime above $5\,\mathrm{A\,cm^{-2}}$. Hence, it is proposed that other transport mechanisms become increasingly relevant at such operating conditions. For example, the electro-osmotic drag of water is one convective transport mechanism, carrying dissolved hydrogen back to the cathode (cf. section 2.2.1). This transport mode is often neglected in model approaches. However, other yet unknown effects may apply as well.

With regard to the initially presented research questions, it is summarized that the supersaturation of water with hydrogen continues at exceptionally high current densities. Again, an increase in cathode pressure enhances this effect. As the relation between the hydrogen crossover flux and current density passes through several regions with different slopes, commonly used model approaches should be revised in order to maintain a physically meaningful description of the mass transport characteristics in PEM-WE cells at the applied operating conditions.

Hydrogen Crossover in PEM Water Electrolysis at Current Densities up to 10 A cm^{-2}

Agate Martin, [ORCID] Patrick Trinke, Boris Bensmann,[z] [ORCID] and Richard Hanke-Rauschenbach [ORCID]

Leibniz University Hannover, Institute of Electric Power Systems, 30167 Hannover, Germany

Hydrogen crossover poses a critical issue in terms of the safe and efficient operation in polymer electrolyte membrane water electrolysis (PEMWE). The impact of key operating parameters such as temperature and pressure on crossover was investigated in the past. However, many recent studies suggest that the relation between the hydrogen crossover flux and the current density is not fully resolved. This study investigates the hydrogen crossover of PEMWE cells using a thin Nafion 212 membrane at current densities up to 10 A cm^{-2} and cathode pressures up to 10 bar, by analysing the anode product gas with gas chromatography. The results show that the hydrogen crossover flux generally increases over the entire current density range. However, the fluxes pass through regions with varying slopes and flatten in the high current regime. Only considering hydrogen diffusion as the single transport mechanism is insufficient to explain these data. Under the prevailing conditions, it is concluded that the electro-osmotic drag of water containing dissolved hydrogen should be considered additionally as a hydrogen transport mechanism. The drag of water acts opposite to hydrogen diffusion and has an attenuating effect on the hydrogen crossover in PEMWE cells with increasing current densities.

This study covers the hydrogen crossover characteristics in polymer electrolyte membrane water electrolysis (PEMWE) at high current densities up 10 A cm^{-2}.

The assessment of hydrogen loss mechanisms is important for establishing PEM water electrolyzers as an efficient tool for the production of green hydrogen.[1,2] Due to various loss mechanisms, such as leakages and the recombination of hydrogen and oxygen at the cathode, the faradaic efficiency in PEMWE is less than unity.[3–5] The probably most important loss of hydrogen is caused by the diffusion of the evolved hydrogen dissolved in water through the membrane into the anode compartment.[6–9] This effect is known as hydrogen crossover. Especially at part load, the so-formed hydrogen in oxygen mixtures can reach hydrogen contents above 4 vol%, which pose a critical safety issue due to the risk of explosion.[6,8,10,11]

For the investigation of fundamental pressure and temperature relations, hydrogen crossover was first evaluated by permeation experiments at zero current.[7,12,13] In the recent years, hydrogen crossover was investigated at electrolysis conditions by analyzing the hydrogen content in the anode product gas, whereby an increase in hydrogen crossover with increasing current densities was observed.[7,14–16] Trinke *et al.*[7,14–16] explain this effect with an increase in the dissolved hydrogen concentration, which results from mass transport limitations within the cathode catalyst layer. This theory was supported by varying the ionomer content in the cathode catalyst layer.[14] It was shown that higher ionomer contents lead to increased mass transport resistances, which in turn result in an increasing supersaturation of water with hydrogen and thus, in higher crossover fluxes.[14] Moreover, Martin *et al.*[17] showed that an increased compression of the cathode leads to similar observable effects.

Generally, hydrogen crossover studies at electrolysis conditions with moderate current densities up to 2 A cm^{-2} and thick perfluorosulfonic acid membranes (fumea EF-40 ∼ 240 μm, Nafion 117 ∼ 178 μm, Nafion 115 ∼ 127 μm) revealed a linear relation between the hydrogen crossover flux and current density.[3,4,6,11,14–16]

More recent studies have used thinner Nafion 212 membranes (51 μm) at higher current densities up to 5 A cm^{-2}.[13,17–19] Compared to the earlier mentioned studies, the usage of thinner membranes generally results in higher anodic hydrogen contents. Further, the relation between the crossover flux and the current density follows a stronger than linear growing function. This functional relation can only partially be explained by known, theoretical approaches, such

as the growing supersaturation with hydrogen at increasing current densities, and the resulting increased driving force for diffusion. However, the former approaches fail to explain other parts of the data, such as the flattening of the hydrogen crossover flux with the further increase of current density or at enhanced cathode pressures.[13,17,20] Thus, it has to be assumed that under these conditions, yet unknown effects happen. This will be considered in more detail within this contribution.

For this purpose, the hydrogen crossover characteristics of a catalyst coated membrane (CCM) based on Nafion 212 is investigated at current densities up to 10 A cm^{-2} and at cathode pressures up to 10 bar. The investigation at these pressure levels is particularly interesting in an industrial context, whereas the high current densities are less important in this context and primarily serve to explore the effects on hydrogen crossover.

After presenting the experimental details for this study, an insight into the polarisation behaviour of the examined PEMWE cell is given. Then, a detailed analysis of the impact of the high applied current densities on hydrogen crossover at ambient and at elevated cathode pressures is performed.

Experimental

Material and cell setup.—A 4 cm^2 cell by Fraunhofer ISE[21] was equipped with a 5.95 mm insulation frame for the anode and a 5.14 mm frame for the cathode. A commercially available CCM based on Nafion 212 (1 mg cm^{-2} Pt/C, 2 mg cm^{-2} Ir black, Hiat gGmbh) was assembled in the cell. For the anode side, a porous transport layer (PTL) made of sintered titanium fibers (1 mm, 2GDL40–1.00, Bekaert) was ultra-sonicated for 10 min in de-ionised water before usage. A carbon paper with hydrophobic treatment (H23I2, now available as E20H, Freudenberg SE) was used as the cathode PTL.

The cell was assembled in dry state. The cell was thermally conditioned by recirculating water through the anode at 80 °C. Then, the compression force of 3 kN was applied. A minimum contact pressure on the active area of 3.3 MPa is estimated, when a homogeneous distribution of the force on the active cell area and the surrounding gaskets is assumed. Please refer to Ref. 17 for more details on the cell setup and the distribution of contact pressure.

Testing periphery.—After cell assembly, the cell was mounted into an electrolysis test station (E100, Greenlight Innovation). Thermal sensors were placed at the electrode endplates. Only the anode side of the cell was supplied with de-ionised water

[z]E-mail: boris.bensmann@ifes.uni-hannover.de

(80 ml min^{-1} at 80 °C). The resistivity of the water in the test station was ⩾ 2 MΩ cm. Here, we would like to highlight the importance of naming the resistivity or conductivity of the de-ionised water used for PEMWE measurements for future works, since it has a significant impact on the cell's performance.[22–24] Manufacturer of electrolyzer systems (e.g. ProtonOnSite,[25,26] Proton Energy Systems[27]) demand a minimum water resistivity of 1 MΩ cm, but recommend a resistivity of greater than 10 MΩ cm. Our own experience shows that PEMWE cells degrade noticeably below the 1 MΩ cm limit. Therefore, we encourage our readers to monitor the minimum resistance continuously.

A SP150 potentiostat equipped with a 100 A booster (current accuracy: 0.5% full scale range, BioLogic) was used as the current source. For the investigation of the hydrogen crossover during electrolysis, the dried product gas was supplied to a gas chromatograph (GC, 490 μGC, Agilent). Helium was used as a carrier gas. In order to ensure safe gas mixtures at low current densities and high cathode pressures, an additional constant oxygen mass flow of 0.06 g min^{-1} ($N_{O_2}^{dil} = 3.125 \cdot 10^{-5}$ mol s^{-1}) was added with a mass flow controller (EL-Flow Prestige, Bronkhorst) to dilute the anode product stream directly behind the cell outlet.

From the diluted, then measured hydrogen content at the GC $\phi_{H_2}^{GC}$, the hydrogen crossover flux $N_{H_2}^{cross}$ is obtained with Eq. 1. Then, Eq. 2 is used to calculate the actual hydrogen content ϕ_{H_2} (see Ref. 17 for details), where $N_{O_2}^{evo} = \frac{i}{4 \cdot F}$ refers to the evolved amount of oxygen by the anodic half-cell reaction.

$$N_{H_2}^{cross} = \frac{\phi_{H_2}^{GC}(N_{O_2}^{evo} + N_{O_2}^{dil})}{1 - \phi_{H_2}^{GC}} \quad [1]$$

$$\phi_{H_2} = \frac{N_{H_2}^{cross}}{N_{H_2}^{cross} + N_{O_2}^{evo}} = \frac{\phi_{H_2}^{GC}(N_{O_2}^{evo} + N_{O_2}^{dil})}{N_{O_2}^{evo} + \phi_{H_2}^{GC} \cdot N_{O_2}^{dil}} \quad [2]$$

Measurement protocol.—Before beginning the actual measurements, the cell was thermally conditioned by recirculating the anode feed water at the operating temperature (80 °C), followed by a polarized conditioning phase at 3 A cm^{-2} for six hours. The conditioning was followed by one measurement block for characterizing the hydrogen crossover and one measurement block for measuring the polarisation behaviour. These two blocks were repeated at each investigated cathode pressure level (1 bar, 4 bar, 7 bar, 10 bar). The anode pressure remained at 1 bar for the entire investigation. The used measurement protocol was based on Ref. 17.

The hydrogen crossover was determined during electrolysis operation by analysing the dried anode product gas via GC. A galvanostatic profile with steps between 0.25 … 10 A cm^{-2} was applied. This cycle was repeated twice. The time intervals for each step were based on previous studies,[14,15,17,28] until a constant hydrogen in oxygen value was reached (3 h for the lowest current density of 0.25 A cm^{-2} down to 1 h starting at a current density of 2 A cm^{-2}).

The polarization behaviour of the cell was measured three times with a galvanostatic step profile with current steps between 0.01 … 10 A cm^{-2} and a holding time of 10 s per step. Each current step was followed by an electrochemical impedance measurement for determining the high frequency resistance R_{HF}. Here, the frequency range was set from 100 kHz to 100 Hz and the amplitude was set to 10% of the DC current. R_{HF} was then identified by the interpolation of the Nyquist plots with the intercept of the real axis.

Results and Discussion

For the sake of completeness, a brief insight into the polarisation behaviour of the investigated PEMWE cell is given before analyzing
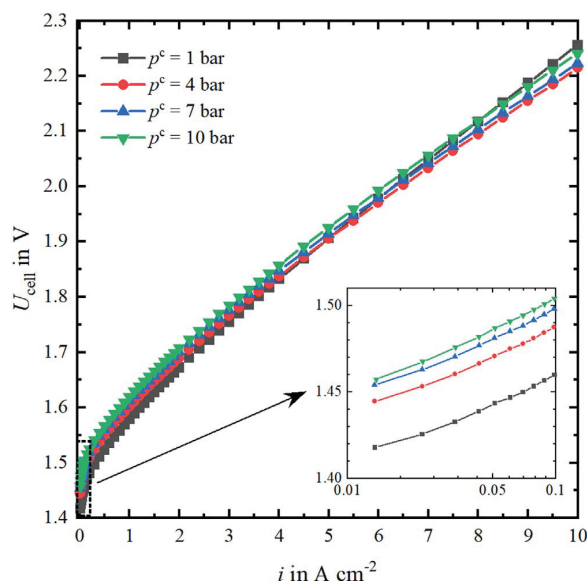

Figure 1. Polarisation behaviour of a 4 cm^2 PEMWE cell, with a Nafion 212 membrane at 80 °C and cathode pressures up to 10 bar. In the zoom of the low current density region (logarithmic), the impact of increasing cathode pressure on the cell voltage becomes clear.

the hydrogen crossover characteristics, which is the focus topic of this contribution.

Polarisation behaviour.—Figure 1 shows the polarisation curves measured with the investigated PEMWE cell at four different cathode pressures. At the maximum current density of 10 A cm^{-2}, the cell voltage remains below 2.25 V. Considering an industrial relevant maximum cell voltage of 2 V, current densities of slightly more than 6 A cm^{-2} can be reached with this setup.

In the low current density region of the polarisation curves (zoom in Fig. 1), the impact of the cathode pressure on the cell voltage according to Nernst's equation is clearly visible. However, the focus of this contribution lays on hydrogen crossover, which is why no further analysis of the cell voltage is given at this point. A more detailed cell voltage breakdown, including the high frequency resistance R_{HF} and iR_{HF}-corrected cell voltage, is given in the Appendix.

Hydrogen crossover at ambient pressure.—The hydrogen crossover measurements at ambient pressure conditions are shown in Fig. 2. The data is divided in three regions, so that the discussion is easier to follow.

Figure 2a) shows the anodic hydrogen in oxygen content ϕ_{H_2}. It is observed that the hydrogen content decreases rapidly at low current densities (region I). This is explained by the linear increase in the amount of evolved oxygen with increasing current density according to Faraday's law, leading to a continuous dilution of the permeated hydrogen (c.f. Eq. 2). At medium current densities (region II), the hydrogen content increases. This trend was already observed in earlier works.[13,17,18,29] Entering region III at high current densities results in a slight decrease of the hydrogen content. To our knowledge, this contribution is a first report on such a course of data.

For the evaluation of the measured data, the hydrogen permeation rate $N_{H_2}^{cross}$ shown in Fig. 2b) (calculated according to Eq. 1), is resolved in the following. Generally, the concentration difference of dissolved hydrogen across the membrane is the driving force for the diffusive hydrogen transport, which is frequently described by Fick's law:[6,7,12,14–16]
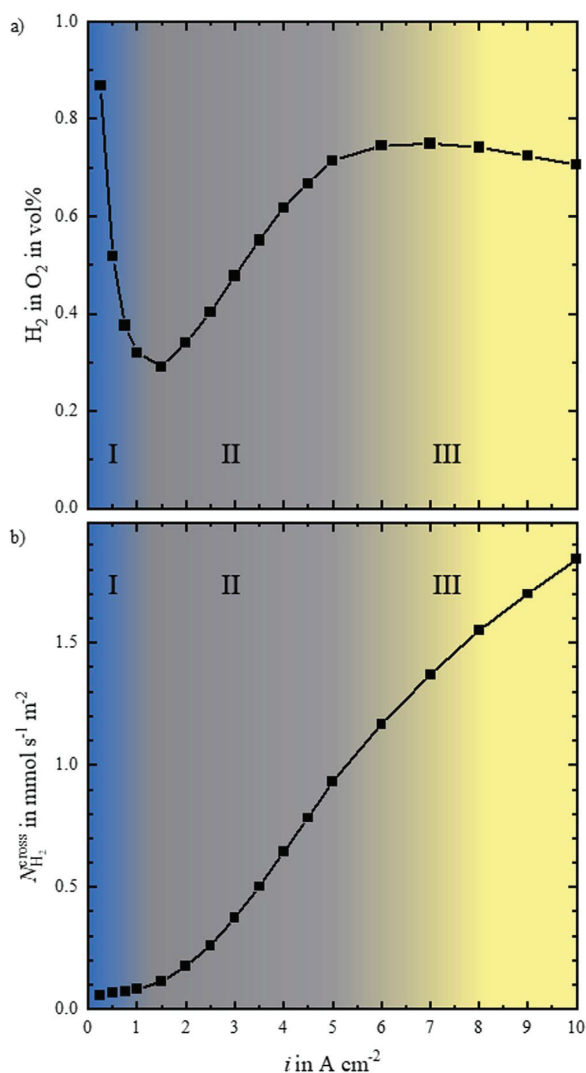
Figure 2. Hydrogen crossover at ambient pressure and 80 °C.

$$N_{H_2}^{diff} = D_{H_2}^{eff} \cdot \frac{c_{H_2}^{*,c} - c_{H_2}^{a}}{\delta_{mem}} \approx D_{H_2}^{eff} \cdot \frac{c_{H_2}^{*,c}(i, k_l, p_{H_2}^{c})}{\delta_{mem}} \qquad [3]$$

Where $D_{H_2}^{eff}$ describes the effective diffusion coefficient of dissolved hydrogen through a wet Nafion membrane and δ_{mem} is the membrane thickness (63 μm for a wet Nafion 212 membrane[12]). Assuming that the hydrogen concentration at the anode $c_{H_2}^{a}$ is negligible, $N_{H_2}^{diff}$ depends mostly on the dissolved, supersaturated hydrogen concentration at the cathode $c_{H_2}^{*,c}$. This supersaturation is a result of mass transport limitations, which depends on the applied current density i and the mass transfer coefficient k_l.[15,16] At zero current, $c_{H_2}^{*,c}$ equals to the hydrogen saturation concentration, which is mainly a function of hydrogen partial pressure $p_{H_2}^{c}$. Consequently, the resulting hydrogen crossover flux at zero current is mainly a function of the hydrogen partial pressure and respectively, of the cathode pressure. This value is the minimum, base amount of permeating hydrogen. In the following, this base diffusion flux will be referred as $N_{H_2}^{diff,0}$.

There are different methods to determine this value (e.g. permeation experiments at zero current,[12,13,30] by electrochemical compensation of permeated hydrogen,[7,8] by linear sweep voltammetry[31] or by extrapolation of the existing data obtained at electrolysis conditions to zero current[13]). Usually, the experimentally obtained values differ slightly from one another.

Trinke et al.[16] investigated the linear relation between $N_{H_2}^{cross}$ and i observed in region I in detail. They concluded that mass transfer resistances in the cathode catalyst layer result in a limited mass transfer of dissolved hydrogen into the gas phase. Since the amount of evolved hydrogen increases linearly with the applied current density (Faraday's law), the dissolved hydrogen concentration increases linearly as well. As a consequence of Fick's law (Eq. 3), the hydrogen crossover flux shows the same linear relationship with current density in this region.

In region II, $N_{H_2}^{cross}$ enters a regime in which a stronger than linear relationship with current density is observed. This effect was already reported in literature[13,18,29] and was recently investigated in a previous work of our group.[17] This functional relationship only agrees with the diffusion approach, if an disproportionate increase of $c_{H_2}^{*,c}$ with i is assumed. This relation can grow stronger than linear, if the reaction front of the hydrogen evolution reaction in the catalyst layer moves towards the membrane[14,32] or other parameters such as the mass transport coefficient k_l or the the diffusion properties in the catalyst layer change. All of these factors result in a continuing growth of $c_{H_2}^{*,c}$ at the interface between the catalyst layer and the membrane, leading to a higher driving force for the cross permeation and eventually to a higher hydrogen crossover flux.

However, the mentioned effects should lead to a further, more than linear growing supersaturation, which would result in a more than linear increase of the hydrogen crossover as well (considering $N_{H_2}^{cross} \approx N_{H_2}^{diff}$). Certainly, this is not observed in region III, but instead a flattening of $N_{H_2}^{cross}$ results in the high current regime. Hence, the earlier introduced, pure diffusive approach with the previous described parameter functionalities, fails to explain the data in at higher current densities.

With such high current densities, increases in temperature and pressure and their impact on hydrogen crossover should be considered. In an earlier study by Trinke et al.,[16] these two and further effects were examined and discussed thoroughly. As the current density increases, more heat is produced, causing the local temperature in the membrane to rise. This causes the diffusion coefficient of hydrogen through Nafion to increase as well and hence, a higher hydrogen crossover flux is expected. However, the current dependence of the crossover flux is found to be stronger than the temperature dependence. The results shown in this work support this finding, since the increase of the hydrogen crossover flux in the high current region III is lower than at medium current densities, as seen in region II. Moreover, Trinke et al.[16] discussed a potential increase of the local hydrogen partial pressure within the cathode with increasing current density. They came to the conclusion that a pressure gradient across the cathode PTL of several 100 bar per cm would be necessary, to explain the observed current dependence of hydrogen crossover. Since such high pressure increases cannot be explained, this approach is insufficient to explain the flattening of the crossover flux observed at high current densities. For this reason, it is assumed that the local increases in temperature and pressure only have a subordinate impact on the current dependence of the hydrogen crossover and therefore do not explain the results either qualitatively or quantitatively.

Another potential explanation for the observed flattening of $N_{H_2}^{cross}$ at high current densities might be another transport mechanism acting in the opposite direction of diffusion. Therefore, the electro-osmotic drag of water comes in mind. During the electrolysis reaction, protons are formed in the anodic half-cell reaction. Due to the electric field between the electrodes, the protons move towards the cathode and drag water molecules with them. Thus, it is obvious that dissolved hydrogen might be carried within the dragged water.[3,15]

This convective hydrogen transport by the electro-osmotic drag of water was already mentioned in literature, but did not receive much attention. Grigoriev et al.[33] were the first to implement this hydrogen transport mechanisms in a mathematical model for PEM water electrolyzers. Schalenbach et al.[3] have simulated hydrogen crossover in PEMWE under various pressure conditions and with different membrane thicknesses and considered the drag of water as well. They came to the conclusion that with the prevailing conditions, diffusion is the dominating transport mechanism and that the impact of the drag on hydrogen crossover is negligible. Trinke et al.[7,15] also emphasized the growing impact of hydrogen and oxygen transport via water drag at increasing current densities. Since diffusion and water drag act in opposite directions in PEMWE, the drag should eventually reduce hydrogen crossover at high current densities.

Generally, the hydrogen transport due to the electro-osmotic drag of water $N_{H_2}^{drag}(x)$ can be described with Eq. 4, where x = 0 marks the interface between membrane and cathode catalyst layer and x reflects the distance to the cathode catalyst layer across the membrane. The net hydrogen crossover flux $N_{H_2}^{cross}$ is then described by Eq. 5.

$$N_{H_2}^{drag}(x) = v_{H_2O}^{drag}(i) \cdot c_{H_2}(x) \qquad [4]$$

$$N_{H_2}^{cross} = N_{H_2}^{diff} - N_{H_2}^{drag} \qquad [5]$$

The velocity of the dragged water is described by $v_{H_2O}^{drag}$ and depends directly on the number of protons transported through the membrane and is therefore a function of the applied current density. Thus, the hydrogen transport via this mechanism is low and slow at small current densities and gains in relevance with increasing current densities. At this point, it is emphasized that the transport via drag does not replace the diffusive transport at high current densities, but that both counteracting mechanisms are coexisting (c.f. Eq. 5).

The dissolved hydrogen concentration at the position x in the membrane is described by $c_{H_2}(x)$. Due to the concentration gradient across the membrane, the hydrogen concentration near the cathode is greater than in the vicinity of the anode. It is therefore expected that the effect of the drag is stronger at the cathode as well. Moreover, the dissolved hydrogen concentration increases with the applied current, which in itself leads to a higher amount of transported hydrogen by the dragged water. A simple calculation in the appendix shows that at higher current densities, hydrogen transport by drag is of the same order of magnitude as the crossover measurement results, which supports this hypothesis.

Following from these assumptions, it is concluded that the amount of dragged hydrogen depends on (i) the amount of dragged water and hence, the current density and (ii) the concentration of dissolved hydrogen within the membrane. According to Eq. 3, the latter can be varied by increasing the hydrogen pressure. For higher cathode pressures it follows that the initial dissolved hydrogen concentration is higher and that the amount of dragged hydrogen already should become noticeable at lower current densities. This hypothesis is evaluated in the next section.

Hydrogen crossover at elevated cathode pressures.—Figure 3a) contains the measured anodic hydrogen content at all investigated cathode pressures. Especially at low current densities, the hydrogen content depends strongly on the cathode pressure, which results in an exceeding of the technical safety criterion of 2 vol% H_2 in O_2 (50% LEL[10]). This is a consequence of the increased base hydrogen permeation flux $N_{H_2}^{diff,0}$ and the low oxygen production rate at the small currents, as described by Eq. 2. In contrast, the increasing oxygen production rate with current density results in a strong dilution of the permeated hydrogen. On account of this, the four curves approach one another at 1 vol%. In the transition area at
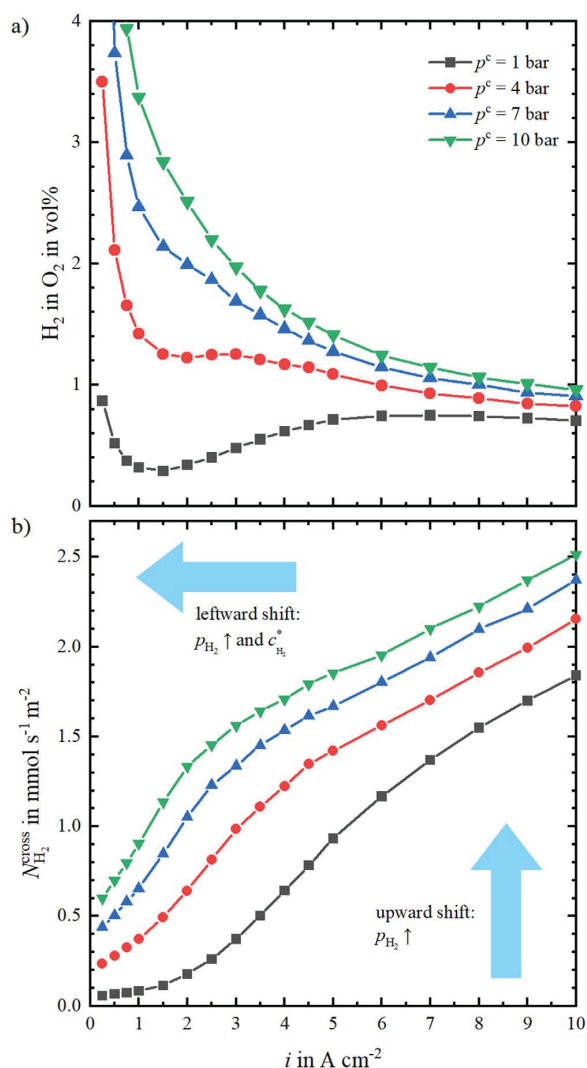

Figure 3. Hydrogen crossover at all cathode pressures and 80 °C. In a) the hydrogen in oxygen content and in b) the hydrogen crossover flux are shown as a function of the current density.

medium current densities, the course of the curve depends on the cathode pressure. At lower pressures, an increase in the hydrogen content is clearly visible and becomes less and less pronounced with increasing pressure. At 15 bar, the hydrogen content has the typical hyperbolic dependence on current density.

A more detailed look into the hydrogen crossover fluxes (Fig. 3b) helps to explain the presented observations. The course of the data at ambient pressure was already discussed in the previous section. This curve is used as a benchmark for comparison in the following discussion.

Generally, the hydrogen crossover fluxes show the same qualitative relation with current density as the benchmark curve. In the beginning, there is a region with a more than linear slope and then the curves flatten at higher current densities. There, the curves seem to be parallel to one another. From a quantitative point of view, the fluxes obtained at higher pressures are shifted (i) upwards to higher permeation fluxes, because of the increasing $N_{H_2}^{diff,0}$ with increasing pressure (c.f. Eq. 3) and (ii) to the left to lower current densities, which results in an earlier flattening of $N_{H_2}^{cross}$.
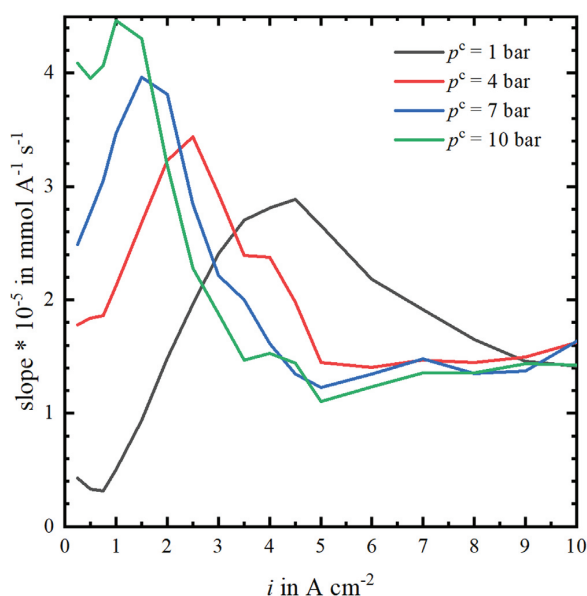
Figure 4. First derivative of the hydrogen crossover fluxes shown in Fig. 3b). With increasing cathode pressure, the maxima shift to lower current densities (1 bar: 4.5 A cm^{-2}, 5 bar: 2.5 A cm^{-2}, 10 bar: 1.5 A cm^{-2}, 15 bar: 1 A cm^{-2}).

For the evaluation of the shift towards lower current densities, the first derivative of $N_{H_2}^{cross}$ is used to assess to slopes (Fig. 4). With respect to the benchmark curve at ambient pressure, the exact same regions as identified in the previous section are visible. The first region up to ~1 A cm^{-2} has a constant slope and corresponds to the linear region I, which was observed previously in Fig. 2b). Then, another region with an increasing slope follows. This region clearly represents the stronger than linear crossover increase (c.f. region II in Fig. 2b). The slope of the ambient pressure curve shows a maximum at ~4.5 A cm^{-2} and decreases afterwards to a value of ~1.2 · 10^{-5} mmol A^{-1} s^{-1}. This reflects the flattening of $N_{H_2}^{cross}$(1 bar) labeled with region III in Fig. 2b).

The other derivatives of $N_{H_2}^{cross}$ at elevated pressures generally show the same trends as the benchmark curve and also pass maxima. From Fig. 4 it becomes clear that the maxima (5 bar: ~2.5 A cm^{-2}, 10 bar: ~1.5 A cm^{-2}, 15 bar: ~1 A cm^{-2}) shift to lower current densities, when the cathode pressure is increased. This mirrors the earlier flattening of the curves (c.f. Fig. 3b). All slopes eventually reach a value of 1.2 · 10^{-5} mmol A^{-1} s^{-1}, which matches to the parallel course of all $N_{H_2}^{cross}$ at high current densities, as seen in Fig. 3b).

These findings fit well to the previous hypothesis, in which it was assumed that the flattening of $N_{H_2}^{cross}$ at high current densities is a result of the electro-osmotic drag of water. This convectively transported water carries an increasing amount of dissolved hydrogen back to the cathode. If this hypothesis is expanded to elevated cathode pressures, it is assumed that the impact of the drag must begin at lower current densities, because the overall amount of dissolved hydrogen is higher and leads to a higher back transport (c.f. Eq. 4). Therefore, $N_{H_2}^{drag}$ should also increase with pressure in exactly this point. In relation to the presented data, it is assumed that the earlier flattening of $N_{H_2}^{cross}$ and the resulting shift of the inflection point to lower current densities (c.f. Fig. 4) supports this hypothesis.

Besides the curve flattening, the parallel course of $N_{H_2}^{cross}$ in the high current density region is another remarkable characteristic. Apparently, the drag counteracts the disproportionate increase of the

hydrogen crossover flux at higher current densities, so that the fluxes eventually increase linearly again. Moreover, it is questionable how long the increase in $N_{H_2}^{cross}$ will proceed. Since the infinite growth of $c_{H_2}^{*,c}$ in the cathode catalyst layer is questionable, there might be a kind of natural limit at some point, which perhaps leads to a saturation of $N_{H_2}^{cross}$. Further, it might be possible that the drag increases so much at even higher cathode pressures, that the hydrogen crossover flux starts to decrease at high current densities.

Summary & Conclusion

In this study, the polarisation behaviours and the hydrogen crossover in PEMWE cells with a thin Nafion 212 membrane at current densities up to 10 A cm^{-2} and cathode pressures up to 10 bar were investigated. At the maximum current density, the resulting cell voltage was only ~2.25 V. Further, no hints for significant mass transport limitations were observed.

The analysis of the hydrogen crossover characteristics was divided in two section (ambient pressure and elevated pressures). The evaluation at ambient pressure revealed that the hydrogen crossover flux generally increases with current density. Further, it was observed that the hydrogen crossover flux passes through a linear and a more than linear region, before flattening out at high current densities. It is assumed that the transition of the slopes at high currents is a first experimental indicator that the hydrogen transport due to the electro-osmotic drag of water competes with the diffusive hydrogen transport. Eventually, these two competing transport modes lead to a lower total increase in the hydrogen crossover flux over the investigated current density range, than expected from a pure diffusive approach.

The crossover analysis at increased cathode pressures revealed that the hydrogen crossover flux not only increases with cathode pressure, but also that the curve flattening begins at lower current densities. It was assumed that this is as well a result of the hydrogen transport via dragged water, because the hydrogen concentration within the membrane increases with pressure.

The presented results indicate that a pure diffusive approach is insufficient to explain experimentally determined hydrogen crossover data, especially at high current densities, and that presumably negligible effects, such as the effect of the electro-osmotic drag on hydrogen crossover, should be considered in future. Further, the results emphasize that the consideration of this transport mode becomes essential, when diffusion is not the dominating gas transport mechanism anymore. This occurs especially when thick membranes are used or as in this study, when high current densities are applied and the hydrogen concentrations are high.

Another aspect to be considered is the impact of the electro-osmotic drag on oxygen crossover. In this study, it was assumed that the drag attenuates the net hydrogen crossover, since it opposes to the hydrogen diffusion direction. Consequently, the drag should enhance oxygen crossover, because it acts in the same direction as the oxygen diffusion. In order to investigate this in more detail, methods for the precise measurement of oxygen crossover during electrolysis have to be established. Further, a model description of the dissolved gas concentration profiles across the catalyst layers and the membrane could help to elucidate the impact of the electro-osmotic drag on both gas crossovers.

Acknowledgments

Estimation of Electro-osmotically Dragged Hydrogen

As the hydrogen concentration depends on the position in the membrane, a one dimensional model is necessary for a more precise calculation of the diffusive and convective hydrogen fluxes through

the membrane. The formulation of such a model is quite extensive, which is why only a very simple estimation (neglecting the dependence on the position) of the dragged hydrogen flux is given here to support our hypothesis, that that the electro-osmotic drag of water at elevated current densities carries a significant amount of hydrogen back to the cathode.

As shown previously, the convective hydrogen transport is calculated as follows (c.f. Eq. 4):

$$N_{H_2}^{drag} = \underbrace{\frac{n_{drag} \cdot i}{F \cdot c_{H_2O}}}_{v_{H_2O}} \cdot c_{H_2}^* \qquad [A \cdot 1]$$

First, the dissolved hydrogen concentration $c_{H_2}^*$ at an average hydrogen crossover flux of $N_{H_2}^{cross} = 0.5$ mmol s^{-1} m^{-2} is calculated from Fick's first law of diffusion (c.f. Eq. 3). With a wet membrane thickness $\delta_{mem} = 63$ μm[12] and an effective diffusion coefficient $D_{H_2}^{eff} = 2.9 \cdot 10^{-9}$ m^2 s^{-1},[14] it follows:

$$c_{H_2}^* = N_{H_2}^{cross} \cdot \frac{\delta_{mem}}{D_{H_2}^{eff}} = 10862 \frac{mmol}{m^3} \qquad [A \cdot 2]$$

In the next step, the concentration of water $c_{H_2O} = 0.054$ mol cm^{-3} is calculated from the ratio of the density at 80 °C $\rho = 0.972$ g cm^{-3} and the molar mass $M_{H_2O} = 18$ g mol^{-1}.

Lastly, at a current density of 5 A cm^{-2} and a mean drag coefficient[40,41] $n_{drag} = 2.5$, a dragged hydrogen flux of $N_{H_2}^{drag} \approx 0.26$ mmol s^{-1} m^{-2} is calculated according to Eq. A·1.

As this value has the same order of magnitude as the crossover measurement results shown in Fig. 2b), it supports the hypothesis, that the convective hydrogen transport via drag can counteract the diffusive transport.

Appendix

Cell voltage analysis.—A detailed cell voltage analysis was omitted in the main part of this contribution, because the focus lays on hydrogen crossover at high current densities in PEMWE. However, the polarisation behaviour and major voltage loss sources at such high current densities should be considered for a complete evaluation of a PEMWE cell. Therefore, the analysis is made up for at this point.

Figure A·1a) shows the measured cell voltage as a function of the applied current density. The dependence on the pressure is clearly visible at low current densities. There, the voltage increases with increasing cathode pressure. Above 6 A cm^{-2}, no clear relation between the cell voltage and the pressure is visible anymore. At the maximum current density of 10 A cm^{-2}, the cell voltage is around 2.25 V.

Möckl et al.[34] investigated the thermal limitations of PEMWE cells operated at high current densities as well. In the study, Nafion membranes of different thicknesses (117, 212 and XL) were compared. The cell with Nafion 212 achieved an almost identical cell voltage (∼2.25 V) at 10 A cm^{-2} compared to the present work. It is also striking that the current-voltage relation appears to remain linear at such high currents. This indicates that PEMWE cells are not limited by water transport to the reaction zone or a product accumulation at either electrode. In Möckl's work,[34] significant mass transport limitations start at around 12 A cm^{-2}. The excellent cell performance reported in this work is mainly a result of the low protonic resistance of the thin membrane. For a thicker Nafion 117 membrane at 80 °C, cell voltages of 2.2 V are already reached below 5 A cm^{-2}.[13,34,35]

In this work, the ohmic cell resistance was measured with electrochemical impedance spectroscopy, by determining the high frequency resistance R_{HF}. The respective results are shown in Fig. A·1b). The values reported here (61 … 68 mΩ cm^2) are slightly higher than those reported in a previous study,[17] although the measurement and the setup are almost identical. One potential explanation may be

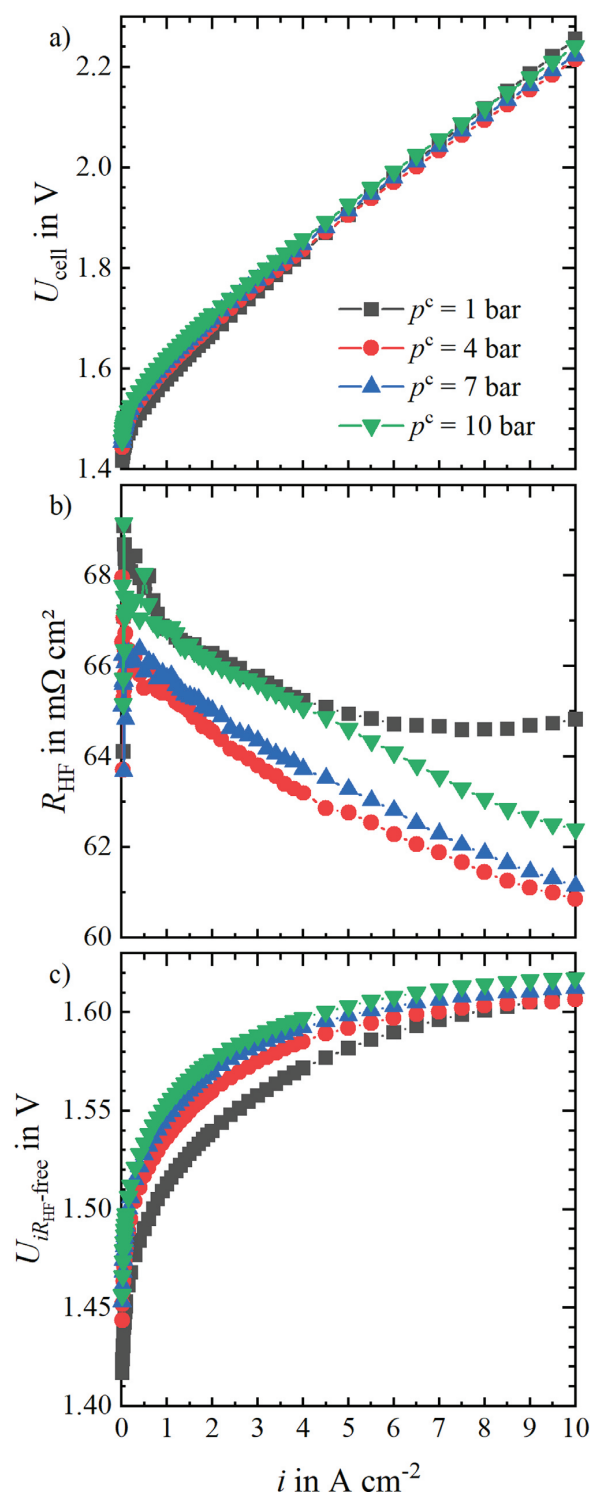**Figure A·1.** Cell voltage analysis of a PEM water electrolysis cell with Nafion 212 at 80 °C. The measured cell voltage is shown in a), b) shows the high frequency resistance R_{HF} and c) presents the iR_{HF}-free cell voltage.

found in differences of the setup. The main setup difference to the previous work is the used anode PTL (1 mm Ti-fiber vs. 350 μm Ir-coated Ti-fibers). In accordance to the works of Liu et al.,[36,37] the

electrochemical performance of cells with an iridium coated PTL is better than with an uncoated one. Iridium prevents the corrosion titanium, leading to a lower PTL resistance and thus, a lower contribution of the PTL to R_{HF}.

Further, it is assumed that the main part of the ohmic cell resistance can be attributed to the ohmic losses due to proton transport through the membrane. Generally, R_{HF} is decreasing with increasing current density. This trend was observed previously and was explained with the reduction of ohmic resistances due to temperature increases at increasing current densities.[17,38,39] This was evidenced with the test station. Temperature probes were placed at the electrode endplates directly below the flow field. Compared to low current densities, a temperature increase of 2 K to 3 K was measured at 10 A cm^{-2} at the anode endplate.

Although the differences between the curves are small ($\leqslant$4 mΩ cm^2), a dependence on pressure is observed. R_{HF} is the lowest at 4 bar. This trend was already observed and discussed previously.[17] In the referred study, the minimum of R_{HF} was measured at a similar cathode pressure level (5 bar).

As a next step of the voltage loss analysis, the ohmic voltage losses are subtracted from the measured cell voltage. The resulting iR_{HF}-corrected cell voltage is shown in Fig. A·1c). Here, it is observed that the iR_{HF}-corrected voltages increase and the distances between the curves decrease with cathode pressure. Both trends can be explained with the logarithmic dependence of the voltage on hydrogen pressure according to Nernst's equation.

In principle, further voltage losses, such as mass transport losses, are expected at high current densities. In order to calculate these, a Tafel analysis, in which the iR-corrected data is linearly fitted with a logarithmic current axis, has to be performed. For this purpose, the measured data must be reliable, especially at low current densities (between 10 … 100 mA cm^{-2}). Hence, high accuracies are needed. Since a very powerful current booster (designed for 100 A) was used for this study, the required accuracy cannot be achieved at the low current densities. For this reason, the Tafel analysis is not performed and the voltage loss break down ends here. At this point, we would like to appeal to our readers, who carry out similar measurements and analyses, to always pay attention to the measuring accuracy of their used devices. This is the only way to check whether the measured data is reliable, suitable for a detailed analysis and worth for sharing with the scientific community.

ORCID

Agate Martin https://orcid.org/0000-0003-4673-1135
Patrick Trinke https://orcid.org/null
Boris Bensmann https://orcid.org/0000-0001-8685-7192
Richard Hanke-Rauschenbach https://orcid.org/0000-0002-1958-307X

References

1. K. Ayers, N. Danilovic, K. Harrison, and H. Xu, *Electrochem. Soc. Interface*, **30**, 67 (2021).
2. K. Ayers, *Curr. Opin. Elechtrochem.*, **18**, 9 (2019).
3. M. Schalenbach, M. Carmo, D. L. Fritz, J. Mergel, and D. Stolten, *Int. J. Hydrogen Energ.*, **38**, 14921 (2013).
4. M. Schalenbach, *Int. J. Hydrogen Energ.*, **41**, 729 (2016).
5. M. Schalenbach and D. Stolten, *Electrochim. Acta*, **156**, 321 (2015).
6. H. Ito, N. Miyazaki, M. Ishida, and A. Nakano, *Int. J. Hydrogen Energ.*, **41**, 20439 (2016).
7. P. Trinke, B. Bensmann, S. Reichstein, R. Hanke-Rauschenbach, and K. Sundmacher, *J. Electrochem. Soc.*, **163**, F3164 (2016).
8. B. Bensmann, R. Hanke-Rauschenbach, and K. Sundmacher, *Int. J. Hydrogen Energ.*, **39**, 49 (2014).
9. F. Scheepers, M. Stähler, A. Stähler, E. Rauls, M. Müller, M. Carmo, and W. Lehnert, *Energies*, **13**, 612 (2020).
10. H. Janssen, J. C. Bringmann, B. Emonts, and V. Schroeder, *Int. J. Hydrogen Energ.*, **29**, 759 (2004).
11. S. A. Grigoriev, P. Millet, S. V. Korobtsev, V. I. Porembskiy, M. Pepic, C. Etievant, C. Puyenchet, and V. N. Fateev, *Int. J. Hydrogen Energ.*, **34**, 5986 (2009).
12. M. Schalenbach, T. Hoefner, P. Paciok, M. Carmo, W. Lueke, and D. Stolten, *J. Phys. Chem. C*, **119**, 25145 (2015).
13. M. Bernt, J. Schröter, M. Möckl, and H. A. Gasteiger, *J. Electrochem. Soc.*, **167**, 124502 (2020).
14. P. Trinke, G. P. Keeley, M. Carmo, B. Bensmann, and R. Hanke-Rauschenbach, *J. Electrochem. Soc.*, **166**, F465 (2019).
15. P. Trinke, P. Haug, J. Brauns, B. Bensmann, R. Hanke-Rauschenbach, and T. Turek, *J. Electrochem. Soc.*, **165**, F502 (2018).
16. P. Trinke, B. Bensmann, and R. Hanke-Rauschenbach, *Int. J. Hydrogen Energ.*, **42**, 14355 (2017).
17. A. Martin, P. Trinke, M. Stähler, A. Stähler, F. Scheepers, B. Bensmann, M. Carmo, W. Lehnert, and R. Hanke-Rauschenbach, *J. Electrochem. Soc.*, **169**, 14502 (2022).
18. M. Stähler, A. Stähler, F. Scheepers, M. Carmo, W. Lehnert, and D. Stolten, *Int. J. Hydrogen Energ.*, **45**, 4008 (2020).
19. S. Garbe, E. Samuelsson, T. J. Schmidt, and L. Gubler, *J. Electrochem. Soc.*, **168**, 104502 (2021).
20. B. Bensmann, A. Rex, and R. Hanke-Rauschenbach, *Curr. Opin. Chem. Eng.*, **36**, 100829 (2022).
21. Fraunhofer Institute for Solar Energy Systems ISE, *Fraunhofer ISE—Annual Report 2020/2021* (Freiburg, Germany) (2021).
22. N. Li, S. S. Araya, X. Cui, and S. K. Kær, *J. Power Sources*, **473**, 228617 (2020).
23. N. Li, S. S. Araya, and S. K. Kær, *J. Power Sources*, **434**, 226755 (2019).
24. S. A. Grigoriev, K. A. Dzhus, D. G. Bessarabov, and P. Millet, *Int. J. Hydrogen Energ.*, **39**(35), 20440 (2014).
25. ProtonOnSite, Technical Specifications H Series Hydrogen Generation System: PD-0600-0062 Rev F https://www.protononsite.com/sites/default/files/2017-04/PD-0600-0062%20Rev%20F.pdf.
26. ProtonOnSite, Technical Specifications M400 Hydrogen Generation System: PD-0600-0122 REV A https://protonenergy.com/sites/default/files/2017-06/PD-0600-0122%20REV%20A.pdf.
27. Proton Energy Systems, Technical Specifications Hogen Hydrogen Generation Systems: S Series Hydrogen Generators http://hmagrp.com/wp-content/uploads/2016/09/HOGEN-S-Series.pdf.
28. A. Martin, D. Abbas, P. Trinke, T. Böhm, M. Bierling, B. Bensmann, S. Thiele, and R. Hanke-Rauschenbach, *J. Electrochem. Soc.*, **168**, 94509 (2021).
29. C. Klose, P. Trinke, T. Böhm, B. Bensmann, S. Vierrath, R. Hanke-Rauschenbach, and S. Thiele, *J. Electrochem. Soc.*, **165**, F1271 (2018).
30. F. Barbir, *Sol. Energy*, **78**, 661 (2005).
31. P. Pei, Z. Wu, Y. Li, X. Jia, D. Chen, and S. Huang, *Appl. Energy*, **215**, 338 (2018).
32. P. Trinke, *Experimental and Model-based Investigations on Gas Crossover in Polymer Electrolyte Membrane Water Electrolyzers* (Hannover, Germany) (2021).
33. S. A. Grigoriev, A. A. Kalinnikov, P. Millet, V. I. Porembsky, and V. N. Fateev, *J. Appl. Electrochem.*, **40**, 921 (2010).
34. M. Möckl, M. Bernt, J. Schröter, and A. Jossen, *Int. J. Hydrogen Energ.*, **45**, 1417 (2020).
35. A. Villagra and P. Millet, *Int. J. Hydrogen Energ.*, **44**, 9708 (2019).
36. C. Liu, M. Carmo, G. Bender, A. Everwand, T. Lickert, J. L. Young, T. Smolinka, D. Stolten, and W. Lehnert, *Electrochem. Commun.*, **97**, 96 (2018).
37. C. Liu et al., *Adv. Energy Mater.*, **11**, 2002926 (2021).
38. T. Schuler, T. J. Schmidt, and F. N. Büchi, *J. Electrochem. Soc.*, **166**, F555 (2019).
39. M. Suermann, T. J. Schmidt, and F. N. Büchi, *Electrochim. Acta*, **211**, 989 (2016).
40. T. A. Zawodzinski, J. Davey, J. Valerio, and S. Gottesfeld, *Electrochim. Acta*, **40**, 297 (1995).
41. Z. Luo, Z. Chang, Y. Zhang, Z. Liu, and J. Li, *Int. J. Hydrogen Energ.*, **35**, 3120 (2010).

5 Approaching the Measurement of Oxygen Crossover

As mentioned in section 2.2.4, the quantification of oxygen crossover is crucial to determine the resulting chemical degradation of the ionomer in a PEM-WE cell. However, the quantification of oxygen in the cathode product gas remains challenging, as most of the oxygen recombines in the cathode and is no longer detectable. In a previous study of Trinke *et al.*[98], a platinum-free cathode catalyst was used to prevent the recombination of hydrogen and oxygen. The findings confirmed qualitatively that the oxygen crossover flux increases with current density, as already known for hydrogen crossover. The use of less active cathode catalysts was taken up for the quantification of oxygen crossover. The resulting research question 4 was examined in an experimental study, which is the focus of this chapter.

Research Question 4: How can the oxygen crossover be measured precisely by changing the cathode catalyst?

The findings of the study are condensed in a peer-reviewed article named "On the Correlation between the Oxygen in Hydrogen Content and the Catalytic Activity of Cathode Catalysts in PEM Water Electrolysis" (*J. Electrochem. Soc.*, 168(11):114513, 2021). The referenced supplemental information on this article is provided in Appendix B. The original article follows behind these introductory and summarizing paragraphs on the concept and key findings of the article.

As mentioned before, the high recombination activity of platinum is identified to be the main reason for the difficult measurement of the actual oxygen crossover. To suppress the recombination reaction, other presumably less active cathode catalysts than platinum are introduced into the cell setup.

Besides platinum as the benchmark cathode catalyst for HER, iridium is used as another representative of the platinum group metals (PGM). Further, three PGM-free catalysts (N-doped carbon nanotubes, N-doped carbon nanotubes decorated with $[Mo_3S_{13}]^{2-}$, titanium suboxide in Magnéli phase) are evaluated. The electrochemical performance of each catalyst is assessed in both, half cell and full cell setups. Moreover, the oxygen crossover characteristics are investigated by measuring the oxygen content of the dried cathode product gas during electrolysis operation.

The full cell polarisation behaviour measured with the PGM-free catalysts is worse than with PGM catalysts. This is expected, since platinum is the best known catalyst for the

HER at the moment, whereby the kinetic overpotentials for the HER are accordingly low. The half cell measurements exploring the HER activity of each catalyst confirm the trend seen in the full cell experiments. Moreover, the gas analysis reveals that with PGM-free catalysts, the measurable oxygen content is higher than with PGM catalysts. The highest measurable oxygen content is measured with the Magnéli phase catalyst, consisting of a titanium suboxide.

The results of the gas analysis suggest that the recombination activity of the cathode catalysts decreases, the higher the measured oxygen content is. The investigation of the activity for the oxygen reduction reaction (ORR), which represent the electrochemical recombination reaction of hydrogen and oxygen, results in the same activity trend as indicated by the gas analysis. Thus, catalysts exposing a low ORR activity lead to higher measurable oxygen contents.

With respect to the research question, it is summarized that cathode catalysts with sluggish recombination activities are indeed applicable for the measurement of higher cathodic oxygen contents. The oxygen crossover flux measured in this way is probably closer to the true crossover behaviour than with recombination-active catalysts, such as platinum. However, the calculated oxygen flux at low permeation rates at small current densities is still lower than the smallest expected flux resulting from permeation experiments at zero current and without catalyst layers. Therefore, it must be assumed that the actual oxygen crossover is even higher than the experimental results imply.

On the Correlation between the Oxygen in Hydrogen Content and the Catalytic Activity of Cathode Catalysts in PEM Water Electrolysis

Agate Martin,[1] Patrick Trinke,[1] Chuyen Van Pham,[2] Melanie Bühler,[3,4] Markus Bierling,[2,5] Peter K. R. Holzapfel,[2,6] Boris Bensmann,[1,z] Simon Thiele,[2,5] and Richard Hanke-Rauschenbach[1]

[1]*Leibniz University Hannover, Institute of Electric Power Systems, 30167 Hannover, Germany*
[2]*Forschungszentrum Jülich GmbH, Helmholtz Institute Erlangen-Nürnberg for Renewable Energy (IEK-11), 91058 Erlangen, Germany*
[3]*Electrochemical Energy Systems, Department of Microsystems Engineering, Albert-Ludwigs-University of Freiburg, 79110 Freiburg, Germany*
[4]*Hahn-Schickard, 79110 Freiburg, Germany*
[5]*Department of Chemical and Biological Engineering, Friedrich-Alexander-Universität Erlangen-Nürnberg, 91058 Erlangen, Germany*
[6]*Technical University of Berlin, Chair of Sustainable Engineering, 10623 Berlin, Germany*

Altogether five platinum group metal (PGM) and PGM-free cathode catalysts were investigated in full PEM water electrolysis cells regarding their polarisation behaviour and their hydrogen and oxygen recombination properties. It was shown that the recombination activity of permeated oxygen and evolved hydrogen within the cathodic catalyst layer correlates with the activity of the oxygen reduction reaction (ORR) which was determined *ex situ* with linear sweep voltammetry. We found that the investigated PGM-free cathode catalysts had a low activity for the ORR resulting in higher measurable oxygen in hydrogen volume fractions compared to the PGM catalysts, which are more active for the ORR. Out of the three investigated PGM-free catalysts, only one commercially available material based on a Ti suboxide showed a similar good polarisation behaviour as the state of the art cathode catalyst platinum, while its recombination activity was the lowest of all catalysts. In addition to the recombination of hydrogen and oxygen on the electrocatalysts, we found that the prevalent carbon-based cathodic porous transport layers (PTL) also offer catalytically active recombination sites. In comparison to an inactive PTL, the measurable oxygen flux using carbon-based PTLs was lower and the recombination was enhanced by microporous coatings with high surface areas.

Hydrogen has a central role in future energy storage scenarios. Polymer electrolyte membrane water electrolysers (PEMWE) are expected to account for a significant share of the hydrogen production facilities in order to fulfil the raising demand.[1,2] However, if significant upscaling of the technology is demanded, two important aspects related to the cathode catalyst material have to be investigated in more detail. Firstly, only the usage of precious platinum group metals (PGM) as electrocatalysts allow a good electrochemical polarisation behaviour and therefore minimal operating costs.[3,4] Secondly, hydrogen purity and the cell's lifetime strongly correlate with oxygen permeation across the cell.[5] As the state of the art materials platinum and iridium may get more expensive due to their scarcity, alternative catalyst designs and materials are required, if the demand raises.[1,2,6] A key challenge within the research field is to find more abundant catalyst materials which withstand the harsh electrochemical environment caused by the low pH of the acidic membrane and the prevailing electric potentials at the electrodes.[1,7–10]

In order to compete with platinum as a hydrogen evolving catalyst, the reaction kinetics has to be as fast as possible so that the cathodic kinetic losses on the cell voltage are kept at a minimum. Another aspect for further investigations are possible side reactions caused by gas crossover.

Also, from PEM fuel cells it is known that the permeation of hydrogen gas from the anode to the cathode leads to the formation of reactive oxygen species, such as hydroxyl radicals, on the platinum particles.[11–13] In PEM water electrolysis, similar problems occur.

The crossover of evolved hydrogen to the anode reduces the efficiency and may form an explosive gas mixture.[14] The same applies to the crossover of evolved oxygen to the cathode. In this case, however, the recombination of both gases to water consumes even more hydrogen and the mentioned radicals are formed by either a chemical or electrochemical pathway.[15] The reactivity of these intermediates is high enough to attack the polymeric backbone of the membrane leading to performance losses due to material degradation and eventually to cell failure and a shortened lifetime.[10–13,16–18] Thus, a deeper understanding on oxygen permeation is crucial. Extensive experimental and theoretical studies on hydrogen crossover were performed in our research group[5,19,20] and by others.[21,22]

As the formation of the intermediate radicals is catalysed by platinum and other impurities such as Fe-ions,[12,15,16] the research on finding new cathode catalysts may also lead to an enhancement of the lifetime, as radical formation might be suppressed. However, less recombination of oxygen and hydrogen at the cathode catalyst reduces the purity of the produced hydrogen. The subsequent purification of the gas is necessary for the most potential hydrogen applications such as fuel cells, which leads to further costs. Besides this extra effort, the system safety is not guaranteed if the oxygen in hydrogen volume exceeds the lower explosion limit (approximately 5% O_2 in H_2[14]). Recently, Trinke *et al.*[23] evidenced the increase in oxygen crossover with increasing current density in PEM electrolysis using platinum and a platinum-free (Pt-free) cathode catalyst. The investigations showed an increased oxygen in hydrogen fraction when using the Pt-free catalyst, which is ascribed to the lower recombination activity compared to platinum. Hence, the evaluation of cathode catalysts is possible by measuring their polarisation behaviour regarding the hydrogen evolution reaction (HER) and their recombination properties, by means of their activity towards

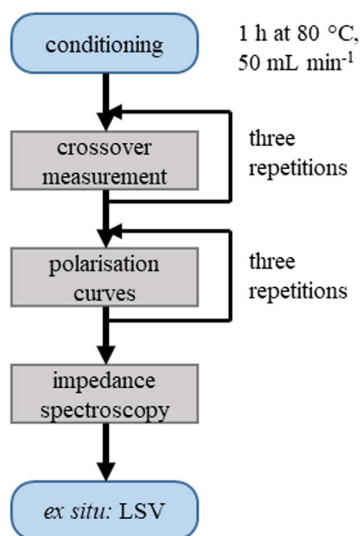[z]E-mail: boris.bensmann@ifes.uni-hannover.de

Figure 1. Illustration of the used electrochemical measurement sequence.

the oxygen reduction reaction (ORR) and the measurable oxygen in hydrogen content.

In this study, we investigated the polarisation behaviour of PEM electrolysis cells using five different cathode catalysts. Pt/C is used as a benchmark catalyst within this study, as it is the state of the art cathode catalyst for the HER. As another PGM catalyst, IrO_2 is used. IrO_2 is reported to be a very good hydrogen evolving electrocatalyst.[24–26] Moreover, three different PGM-free catalysts were investigated. The first one is based on a commercially available PGM-free cathode catalyst for PEM electrolysis. The catalyst (named "Magnéli phase" in this work) is a modified version of Ebonex® which consists of titanium suboxides in Magnéli phase.[27] The other two catalysts are completely PGM-free and are based on nitrogen doped carbon nanotubes (N-doped CNT). Recently, Zeng *et al.*[28] reported that N-doped CNTs are promising electrocatalysts for the HER and the ORR. Hinnemann *et al.*[8] identified molybdenum sulfides as a possible candidate for the HER via computational simulations. Other research groups confirmed the materials catalytic activity experimentally.[6,7,9,29–31] However, they also identified that the catalyst design is very important as only the particle edges are active for HER. As the bulk material is a rather bad electronic conductor, it needs a suitable substrate such as the aforementioned N-doped CNT. In a recent work, Holzapfel *et al.*[32] introduced $[Mo_3S_{13}]^{2-}$@N-doped CNT as a cathode catalyst in full PEM electrolysis cells and report current densities of almost $4\,A\,cm^{-2}$ at a cell voltage of 2.3 V when using a Nafion 212 membrane. We extended the ordinary electrochemical characterisation (polarisation curves, electrochemical impedance spectroscopy and linear sweep voltammetry) by measuring the permeated oxygen in the cathodic product gas to draw conclusions on the recombination characteristics of the used catalysts.

Experimental

Setup and materials.—In this study, commercial Nafion 115 membranes with only an anodic catalyst layer consisting of iridium ($2.0\,mg\,cm^{-2}$ Ir-black, Hiat gGmbH) and an active area of $25\,cm^2$ were used. The anodic porous transport layer (PTL) was a titanium fibre (1 mm, titanium grade 1, 2GDL40–1.00, Bekaert).

For the cathode side, porous transport electrodes (PTE), based on carbon PTLs with a microporous layer (MPL) (H24C5, Freudenberg SE) were used as a substrate for the following catalysts: Pt/C ($0.5\,mg\,cm^{-2}$, HiSPEC 9100, Alfa Aesar), IrO_2 ($1.5\,mg\,cm^{-2}$, Premion, Alfa Aesar), Magnéli phase catalyst ($1.5\,mg\,cm^{-2}$,

Pt-free, Hiat gGmbH), N-doped CNT ($1.5\,mg\,cm^{-2}$, ACS Material) and $[Mo_3S_{13}]^{2-}$@N-doped CNT ($1.5\,mg\,cm^{-2}$, self-synthesized according to Holzapfel *et al.*[32]).

The catalyst layers were deposited onto the substrates by spray coating (Exacta Coat, Sono-Tek). The height of the ultrasonic nozzle was set to 37 mm, the shaping air pressure was 0.6 kPa, speed $170\,mm\,s^{-1}$, flow rate $0.5\,ml\,min^{-1}$ and the ultrasonication energy was set to 5 W at 48 kHz. The PTLs were fixed on a hot plate set to 110 °C. The coating inks consisted of 1 wt% solids (catalyst powder and Nafion D520, FuelCellStore) in a mixture of deionised water and 2-propanol as solvents. The ratio of water and 2-propanol was 1:1 for $[Mo_3S_{13}]^{2-}$@N-CNT mixed with 10 wt% carbon black (Vulcan XC-72R, FuelCellsEtc). For Pt/C and the Magnéli phase catalyst a ratio of 1:3 was chosen for better ink stability. The ionomer content was 20 wt% of the solid part. The ink mixing was performed as described elsewhere[33] with the difference of stirring for two days in between the sonication steps.

Before cell assembly, the Ti-PTL was sonicated for 15 min in deionised water to remove contaminants and the half-coated membrane was immersed into deionised water for about an hour. Then, the Ti-PTL, the wet half-coated membrane and the PTE were assembled. The membrane electrode assemblies (MEAs) were analysed in a quickCONNECTfixture qCf FC25/100 (LC) frame and a $5 \times 5\,cm^2$ electrolyser cell (baltic FuelCells GmbH). The pressure on the active area is controlled by a pneumatic actuator in the cell and was set to 4.5 bar(g), which corresponds to an approximate clamping pressure of 1.4 MPa.[34] The cell has parallel flow fields with 1.87 mm wide lands and 2.5 mm wide channels on both electrodes. For maintaining a constant cell temperature of 80 °C, the cell was tempered with a circulation thermostat (ministat 230, Huber AG). The cell temperature was monitored by thermal sensors placed closely to the flow fields.

The crossover measurements and electrochemical characterisation were performed at ambient pressure in a teststation (E100, Greenlight Innovation) at 80 °C with deionised water supply of $50\,ml\,min^{-1}$ on the anode side only.

Data acquisition.—For the structural analysis, small parts of the PTEs were fixed on an aluminium SEM specimen stub with conductive carbon pads. The samples were coated with gold (108 Manual Sputter Coater, Cressington) to increase the electric conductivity of the samples. Imaging was done with a focused ion beam scanning electron microscope (FIB-SEM, Crossbeam 540, Zeiss) with a Gemini II column. Surface images were obtained by applying an acceleration voltage of 3 kV and a beam current of 750 pA. Additionally, cross-sectional images of all five samples were taken. For this, a protective platinum layer was deposited on all samples (except the N-doped CNT) via ion beam deposition using a gas injection system (Orsay Physics, MonoGIS). The trenches were cut with a 30 kV and 7 nA ion beam. The cross-sections were polished in two steps (first with 1.30 kV and 700 pA and then with 2.30 kV and 100 pA). Finally, the cross-sectional SEM images were obtained by applying an acceleration voltage of 3 kV and a beam current of 750 pA.

The order of the electrochemical measurements is illustrated in Fig. 1. Prior to the electrochemical testing, the cells were tempered at 80 °C with deionised water with a supply of $50\,ml\,min^{-1}$ on the anode side only. The measurement protocol started with three subsequent measurements of the gas crossover from $0.1\,A\,cm^{-2}$ up to $2\,A\,cm^{-2}$. Each current density step was held until a steady state in the gas mixtures was reached. Only the third data set was used for further analysis, as they were the most stable.

After the crossover measurements, three subsequent polarisation curves were recorded. Only the third data set was used for further analysis as no divergences between the curves were observed. Then, electrochemical impedance spectra were recorded. The catalysts were scraped off the analysed PTEs in order to measure their catalytic activities *ex situ* with linear sweep voltammetry (LSV).

Crossover measurements.—For the gas crossover measurement, the cells were operated galvanostatically with a DC current supply (XG 6–220, Sorensen) from 0.1 A cm^{-2} to 2 A cm^{-2}. The holding time at the investigated current densities was adjusted to the different production rates until a steady state in the measured gas composition was reached. As the gas production rates are low at low current densities, the holding times were longer. For the investigated current densities (0.1, 0.2, 0.4, 0.6, 1, 1.5 and 2 A cm^{-2}), the holding times were set to 7, 5, 3, 2.5, 2, 1.5 and 1 h, respectively. The cathodic product gas was analysed with a gas chromatograph (490 Micro GC System, Agilent). Helium was used as a carrier gas. The gas samples were separated in 5 Å mole sieve columns of 10 m length and were analysed with an integrated thermal conductivity detector. Prior to analysis of the dried cathode product gas, the chromatograph was calibrated with O$_2$ in H$_2$ mixtures in known concentrations.

Polarisation curves.—The polarisation curves were recorded from 0.01 A cm^{-2} to 2 A cm^{-2} with a Solartron ModuLab XM PSTAT with a power booster (6 V/100 A) in logarithmic decimal current density steps. The holding time was approximately 25 s and included the measurement of the high frequency resistance R_{HF} from 10 kHz to 100 Hz with a 10% root mean square (RMS).

Electrochemical impedance spectroscopy.—Full electrochemical impedance spectra at 0.1, 0.5, 1.0, 1.5 and 2.0 A cm^{-2} were recorded in a frequency range of 100 kHz to 100 mHz with 7 points per decade and a 10% RMS using the same hardware as for recording the polarisation curves.

Data evaluation.—*Polarisation curves.*—For an analysis of the cell kinetics, the measured polarisation curves were corrected by the ohmic potential drop (Eq. 1).

$$U_{iR_{HF}-free} = U_{cell} - i \cdot R_{HF} \tag{1}$$

It is assumed that the ohmic cell resistance is equal to the measured high frequency impedance R_{HF} where the imaginary part of the impedance equals zero. These high frequency resistances were obtained by interpolating the respective Nyquist plots at the intercept with the real axis linearly.

For a further analysis of the iR_{HF}-free cell voltage, the standard cell potential at 80 °C ($U_{cell}^{\circ} = 1.18$ V) was subtracted to obtain the remaining overpotentials η (Eq. 2).

$$\eta = U_{iR_{HF}-free} - U_{cell}^{\circ} \tag{2}$$

Quantification of oxygen permeation and oxygen content.—The oxygen volume fraction in cathode product gas $\varphi_{O_2}^{c,out}$ can be expressed by Eq. 3.

$$\varphi_{O_2}^{c,out} = \frac{N_{O_2}^{c,out}}{N_{H_2}^{evolved} - N_{H_2}^{perm} + N_{O_2}^{c,out}} \approx \frac{N_{O_2}^{c,out}}{N_{H_2}^{evolved}} \tag{3}$$

$N_{O_2}^{c,out}$ is the oxygen flux in the dried cathode product gas, $N_{H_2}^{evolved}$ is the amount of evolved hydrogen and $N_{H_2}^{perm}$ equals to the permeated hydrogen to the anode. As the amount of $N_{H_2}^{perm}$ and $N_{O_2}^{c,out}$ are very small compared to the amount of evolved hydrogen, the values can be neglected in the denominator for calculation (errors up to $\approx 2\%$). Then, $N_{O_2}^{c,out}$ can be expressed by Eq. 4.

$$N_{O_2}^{c,out} \approx \varphi_{O_2}^{c,out} \cdot N_{H_2}^{evolved} = \varphi_{O_2}^{c,out} \cdot \frac{i}{2 \cdot F} \tag{4}$$

The permeation of oxygen from the anode through the membrane into the cathodic compartment is assumed to be a result of diffusive and convective transport mechanisms.[23,35] However, the minimum, theoretical flux of oxygen caused purely by diffusion across a Nafion membrane $N_{O_2}^{diff}$ can be calculated according to Eq. 5.[22,36]

$$N_{O_2}^{diff} = P_{O_2} \cdot \frac{\Delta p_{O_2}}{\delta_{mem}} \tag{5}$$

P_{O_2} is the permeability coefficient of oxygen through a wet Nafion membrane ($\approx 2.52 \cdot 10-9$ mo m^{-1} s^{-1} bar^{-1} at 80 °C[22]) and δ_{mem} is the wet membrane thickness (≈ 152 μm[22]). The oxygen partial pressure difference is described by Δp_{O_2}. The partial pressure of oxygen at the cathode is assumed to be negligible, whereas the
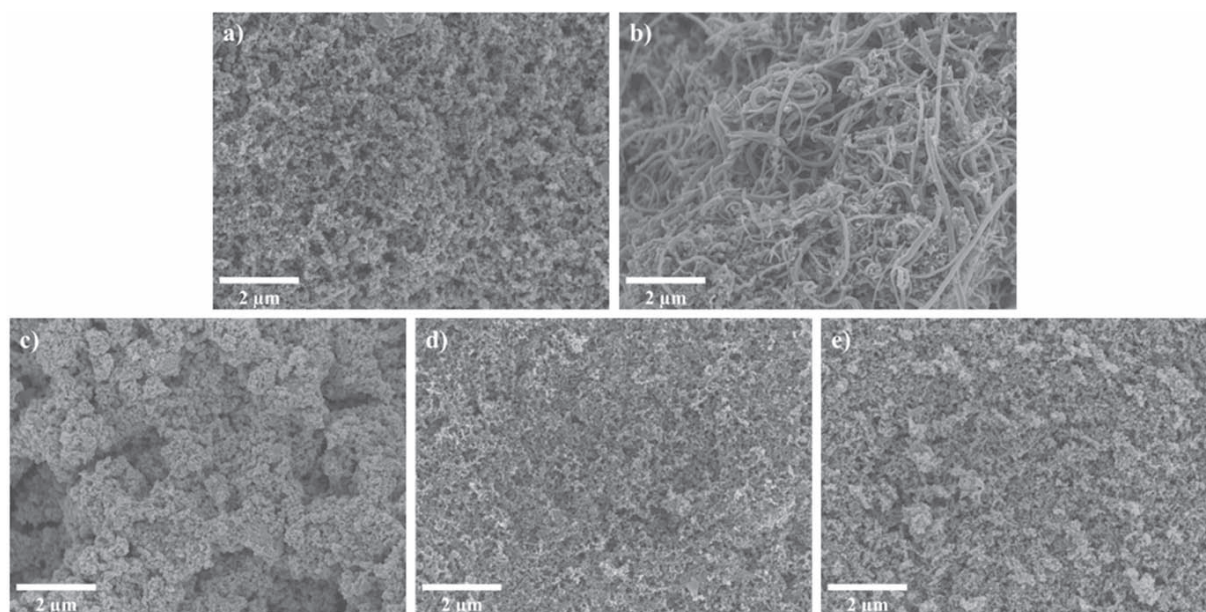

Figure 2. SEM surface images of a) [Mo$_3$S$_{13}$]$^{2-}$@N-CNT, b) N-doped CNT, c) IrO$_2$, d) Magnéli phase and e) Pt/C.
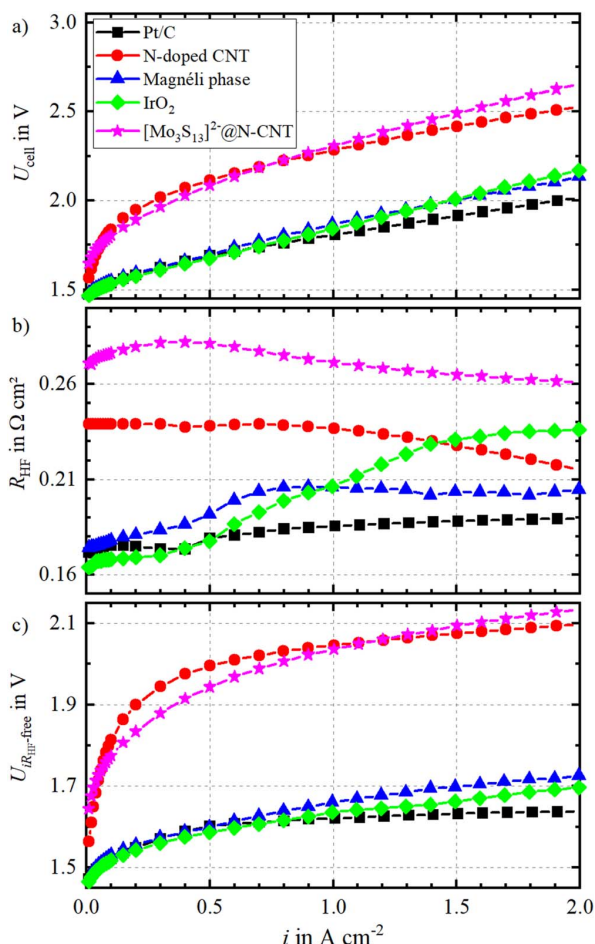
Figure 3. Measured polarisation curves in a), high frequency resistances R_{HF} in b) and iR_{HF}-corrected cell voltages in c) of the five cell configurations, each with another cathode electrocatalyst at 80 °C and ambient pressure.

anodic oxygen partial pressure is equal to the total anodic pressure of 1 bar subtracted by the vapour pressure of water at 80 °C (≈ 0.4737 bar[37]). For these conditions, an oxygen partial pressure difference of $\Delta p_{O_2} = 0.5263$ bar follows. The diffusional oxygen permeation rate is assumed to be constant over the investigated range of current density, as the pressure and temperature can be assumed as almost constant of the applied current density. This yields a diffusive oxygen permeation of $N_{O_2}^{diff} = 0.0087$ mmol m^{-2} s^{-1}.

As explained by Trinke *et al.*,[23] the main reason for the convective oxygen transport could be a result of the electro-osmotic drag of water, which increases with the applied current density.[35] Thus, it can be assumed that the permeation rate of oxygen also shows a current dependency. However, the ratio between the diffusive and convective transport processes cannot be distinguished as it is impossible to measure the convective transport without the diffusive transport as well as an unknown amount of permeated oxygen recombines with hydrogen. Accordingly, we assume that $N_{O_2}^{diff}$ is the minimum oxygen flux within the cathodic compartment, when no convective transport (i.e. at 0 A cm^{-2}) and no recombination takes place.

Results and Discussion

Structural characterisation of the porous transport electrodes.—The surfaces of the PTEs were assessed by scanning electron microscopy (SEM), see Fig. 2. The surfaces imply that

the catalyst layer structures are different from one another. The surfaces of the N-CNTs (Fig. 2b) and IrO$_2$ (Fig. 2c) appear more inhomogeneous than the others. Due to the random positioning of the CNTs, the resulting pore network is inhomogeneous as well. This is also visible in the cross-sectional SEM image of the PTE in Fig. S4 (available online at stacks.iop.org/JES/168/114513/mmedia) within the supplemental information. The CNTs form an inhomogeneous pore network, which is also present when using $[Mo_3S_{13}]^{2-}$@N-CNT. Although its surface appeals a homogeneous structure (Fig. 2a), the cross-section reveals large pore areas and large particle clusters (Fig. S3).

The surface of the PTE with the commercial Magnéli phase catalyst (Fig. 2d) shows a fine particle network, which is also visible in the cross-sectional image (Fig. S1). However, there are also big particles (1–3 μm) present. An energy-dispersive X-ray spectroscopic scan (EDXS) revealed that these clusters consist of titanium and oxygen, which fits to the catalyst description of the manufacturer. To our surprise, the EDXS also revealed the existence of iridium within the catalyst layer. As the iridium containing particle clusters are sparsely distributed and also contain titanium and oxygen, we believe that they are made of a binary transition metal Magnéli phase with Ti and Ir. Despite the existence of iridium, we classify this catalyst as PGM-free, since the electrochemical activity of this material is based on its distinct crystallographic structure (cf. low ORR activity Fig. 9).

The structure of the PTE with Pt/C (Figs. 2e) and S5) prove a homogeneous distribution of the catalyst and a homogeneous pore network. Like the Pt/C and Magnéli phase catalysts, IrO$_2$ was also obtained commercially. The resulting particle-pore network using IrO$_2$ is similar to Pt/C (Fig. S2). However, the surface already implies a rougher surface structure of the catalyst layer. Although the thickness of the other catalyst layers was not determined, the cross-sectional image of the IrO$_2$ PTE shows by far the thinnest catalyst layer (Fig. S2). In this particular cross-section, the thickness is only 2–5 μm.

Polarisation behaviour and kinetics.—The polarisation behaviours of the five investigated cell configurations are shown in Fig. 3a). The five curves can be divided into two groups. The three polarisation curves with the lower cell voltage show a good polarisation behaviour whereas the other two curves with higher cell voltages perform rather poor.

In the group of the well performing cells, the configuration with the state of the art cathode catalyst Pt/C shows the lowest cell voltage over the whole current density range. At low current densities, the polarisation behaviours using IrO$_2$ and the Magnéli phase at the cathode are very close to Pt/C. With increasing current densities, the cell voltages using these two catalyst are approximately 100 mV higher than with Pt/C. When the current density at 2 V is related to the total catalyst mass, the differences become more apparent. When IrO$_2$ and the Magnéli phase are used, mass specific currents of 0.46 A mg^{-1} and 0.48 A mg^{-1}, respectively, are obtained. With Pt/C, the highest current (0.87 A mg^{-1}) is achieved at this voltage.

The cells with the two carbon-based cathode catalysts (N-doped CNT and $[Mo_3S_{13}]^{2-}$@N-CNT) have higher cell voltages over the entire current density range than the well performing configurations. Up to approximately 0.8 A cm^{-2}, the cell with $[Mo_3S_{13}]^{2-}$@N-CNT shows lower cell voltages than with N-doped CNT. Above this value and intensifying with increasing current density, the cell with N-doped CNT performs better. This divergence in the polarisation behaviour of the cells can be partly dedicated to increases in R_{HF}, as shown in Fig. 3b). In their work, Holzapfel *et al.*[32] used the same $[Mo_3S_{13}]^{2-}$@N-CNT cathode catalyst in a full PEM cell setup. A similar cell polarisation behaviour was achieved using a Nafion 115 membrane (ca. 2.1 V at 1 A cm^{-2} vs 2.25 V in this work).

The high frequency resistances show a strong current dependency (Fig. 3b). The curves can be grouped similarly to the polarisation curves in Fig. 3a). At current densities close to zero, the high
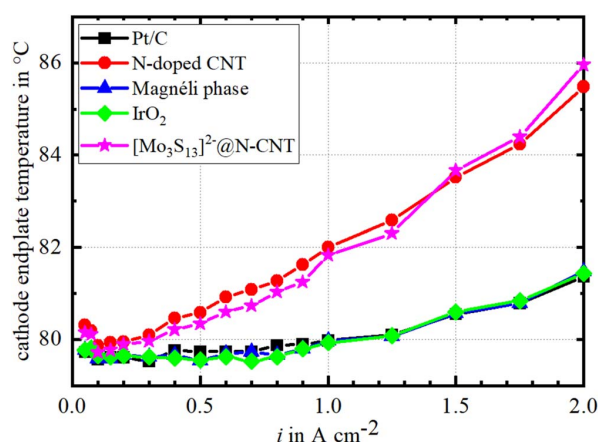
Figure 4. Temperature recorded at the cathodic endplate as a function of the applied current density.
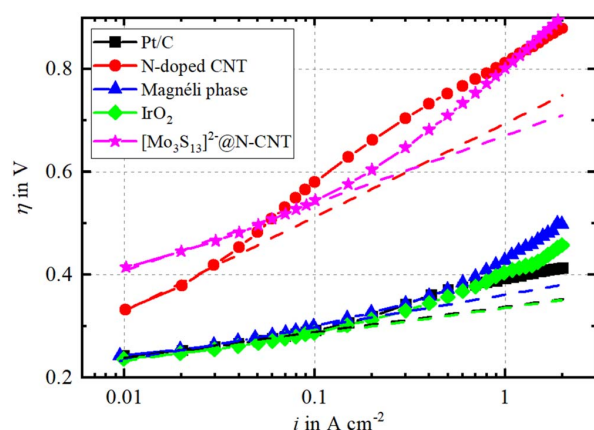

Figure 5. Semi-logarithmic plot of the remaining overpotentials as a function of the current density. The fitted Tafel slopes are extrapolated with dashed lines.

frequency resistances of the good performing catalysts are close to one another. For these three catalysts, R_{HF} increases with increasing current density. However, the absolute increase for Pt/C is very small compared to the other configurations. The increase when using IrO_2 is noticeably steeper and ends at higher R_{HF} values than the N-doped CNT.

The cells using the carbon-based catalysts show significantly higher R_{HF} values compared to the well performing cells. However, the resistances are decreasing with increasing current density. This observation can be explained by the poor polarisation behaviour of these catalysts, which is mainly caused by high overpotentials for the HER. The insufficient cathode kinetics result in more heat production with increasing current density, as shown in Fig. 4. For the two carbon-based catalysts, a temperature increase of approximately 5 K was measured at the cathode endplates, whereas the endplate temperatures of the better performing catalysts remained almost constant over the investigated current range. As the increase in temperature has a positive effect on the ionic conductivity of the membrane, a decrease in R_{HF} can be observed.[38]

Theoretically, the ohmic resistance contains the protonic transport resistance within the membrane, the electric resistance of the PTLs as well as of the metallic bulk material, and interfaces within the cell, and, depending on the location of the reaction zone within the catalyst layer, also protonic and electric losses in the catalyst layer. Normally, the main part of the measured high frequency resistance is related to the protonic losses of the membrane. As the used membrane is identical in all cases, the high frequency resistances should be similar in all cell configurations. For Nafion 115, R_{HF} values between approximately 115 mΩ cm^{-2} [20] and 140 mΩ cm^{-2} [39] were reported. As the measured values in this work (Fig. 3b) lay above the reported values, it can be assumed that more than just the protonic resistances resulting from the membrane were measured. As shown in the previous section, both the surface structure and the catalyst layer structures differ from one another. The catalyst layers with Pt/C, IrO_2 and the Magnéli phase catalyst have a more homogeneous character than the two carbon based catalysts. These differences in structure and the different electronic properties of the catalyst materials also contribute to the measured R_{HF} as stated above. The observed trend in the catalyst layer structures gives hints for possible reasons. As mentioned above, the three well performing catalysts show similar R_{HF} values at low current densities and then increase. The increase for IrO_2 is the highest. The SEM images (cf. surface images in Fig. 2 and cross-sections in Figs. S1 to S5) revealed that this catalyst layer was very thin compared to the others. The different surface structures might have an impact on the resulting contact resistances. The significance of smooth interfaces between the catalyst layer and the membrane for low R_{HF} values was reported previously.[40,41]

A correction of the polarisation curves by iR_{HF} leads to the graphs shown in Fig. 3c). The grouping of the cells remains the same as before. The well performing cathode catalysts are overlapping in the activation regime up to 0.5 A cm^{-2}. From there, the cells containing IrO_2 and the Magnéli phase show additional voltage losses compared to Pt/C. The two curves showing the carbon-based catalysts are barely overlapping in the activation regime and cross each other at 1.2 A cm^{-2}. Since the loading of the state of the art catalyst, Pt/C, is three times lower than that of the other catalysts, the mass specific current was also considered (cf. Fig. S6 in supplemental information). There, the well performing catalysts show the same activation behaviour at small currents. Thus, it can be assumed that the cell kinetics using IrO_2 and the Magnéli phase are still comparable to that of platinum.

The Tafel plot can be obtained from these data when U_{cell}° is subtracted according to Eq. 2 and depicting the abscissa logarithmically. The resulting Fig. 5 contains further indicators for the divergences in the polarisation behaviour, besides increases in R_{HF}. It can be assumed that in the low current density region the overpotentials are dominated by activation processes and that mass transport limitations do not exist until at least a current density of 0.1 A cm^{-2}. One can obtain the Tafel slope by fitting η against the logarithmic current density between 0.01 A cm^{-2} and 0.1 A cm^{-2}. For the N-doped CNTs a fitting interval between 0.01 A cm^{-2} and 0.03 A cm^{-2} was chosen for retaining linearity. From the increasing differences between the extrapolated fits to higher current densities (dashed lines in Fig. 5) and the data sets, other losses such as mass transport resistances and ohmic losses within the catalyst layer can be read.[20,42] In the state of the art cell setup with IrO_2 as anodic catalyst and Pt/C as cathodic catalyst, it is assumed that η_{act} is dominated by the slow oxygen evolution kinetics, whereas the cathodic voltage losses are assumed to be negligible. In this case, the slope in the Tafel representation at low current densities is solely associated to the anode kinetics.

In the present study, this assumption needs to be reassessed. As displayed in Fig. 5, the slopes of the well performing catalysts (Pt/C, IrO_2 and the Magnéli phase) are very close to one another (about 50 to 60 mV dec^{-1}). Assuming that the voltage losses due to the anodic oxygen evolution reaction is the same in all cases and overlap with the hydrogen evolving kinetics, the similar slope indicates similarly fast hydrogen evolution kinetics.

The slopes of the carbon based catalysts are significantly higher compared to the other three catalysts (about 130 mV dec^{-1} for $[Mo_3S_{13}]^{2-}$@N-CNT and 180 mV dec^{-1} for N-doped CNT).

Evidently, the hydrogen evolution kinetics are far slower using these catalysts. In this case, the assumption that the fitted slopes can be assigned completely to the oxygen evolution reaction is not valid anymore. A proper separation of the slope into an anodic and cathodic contribution is not possible as no half-cell potentials were measured.

Further explanations for the different polarisation behaviours of the catalysts can be taken from the electrochemical impedance spectra shown in Fig. 6. The shown impedance spectra were measured at low current densities and represent a kinetically dominated at 100 mA cm^{-2} (Figs. 6a) and 6b) and a resistively dominated region of the cell behaviour at 500 mA cm^{-2} (Figs. 6c) and 6d). The amplitude responses were corrected by R_{HF} in order to allow a more detailed comparison of the catalysts.

The amplitude responses at low frequencies describes the charge transfer resistance R_{CT}. With increasing current density, R_{CT} decreases due to higher reaction rates at the electrodes.[43–45] At both current densities, the amplitude responses of Pt/C, IrO$_2$ and the Magnéli phase catalyst are almost identical. In comparison, the low frequency amplitude of the carbon-based catalysts ([Mo$_3$S$_{13}$]$^{2-}$@N-CNT and N-doped CNT) are higher. At 100 mA cm^{-2}, the amplitude of N-doped CNT is about 1 Ω cm^2 higher than the value for Pt/C whereas the value of [Mo$_3$S$_{13}$]$^{2-}$@N-CNT lays in between. At 500 mA cm^{-2}, the low frequency amplitudes of both carbon-based catalysts approach one another. However, the amplitude of the nanotubes at 0.1 Hz is lower than of [Mo$_3$S$_{13}$]$^{2-}$@N-CNT.

Similar to the preceding analysis of the Tafel plots (Fig. 5), the integral cell impedance cannot be resolved into an anodic and cathodic contribution. Generally, it is assumed that the sluggish oxygen evolution reaction also dominates the cell impedance.[46–48] As the anodes and the respective anodic interfaces are identical in every cell, changes in the impedance spectra can be attributed to the different cathode catalysts, other interface and mass transport characteristics. Thus, it is reasonable to attribute the divergences in the amplitude responses at low current densities to varying charge

transfer and interface resistances at the cathode. These resistances seem to be similar for the PGM catalysts and the Magnéli phase catalyst, whereas the resulting values for the carbon-based catalysts are higher. The lower the charge transfer resistance is, the faster is the kinetics of the respective reaction. In this case, the HER kinetics of the Pt/C, IrO$_2$ and the Magnéli phase catalyst are the fastest, followed by [Mo$_3$S$_{13}$]$^{2-}$@N-CNT. The HER kinetics on N-doped CNT are the slowest.

Figures 6b and 6d show the phase response of the impedance spectra at 100 mA cm^{-2} and 500 mA cm^{-2}, respectively. Usually, positive phase values are neglected during analysis of the impedance data because they are assumed to be caused by inductive effects of the measurement setup (e.g. cables). Therefore, the phase plots only show negative values. Herein, deviations between the catalysts and between the current densities can be observed. At 100 mA cm^{-2} (Fig. 6b), the phase response of all cell configurations, except when using N-doped CNT, are similar. For the PGM catalysts and the Magnéli phase catalyst, only one distinct minimum in the phase shift at approximately 20 Hz can be observed. For [Mo$_3$S$_{13}$]$^{2-}$@N-CNT the minimum at higher frequencies is more pronounced as for the other catalysts. In the phase response of N-doped CNT, there are also two overlapping minima which are shifted to higher frequencies and higher absolute phases compared to the other cell configurations. This is a result of the higher cathodic charge transfer resistance as seen in Fig. 6a and a lower capacitance compared to the other catalysts. A lower capacitance also explains the frequency shift of the intersection with the abscissa to higher frequency values.[45]

The phase responses at 500 mA cm^{-2} (Fig. 6d) generally show lower phase values than at the lower current density. This is a result of lower charge transfer resistances of the electrodes with increasing current density. The cell configurations with Pt/C, IrO$_2$ and the Magnéli phase catalyst again show a qualitatively similar phase response. In contrast to 100 mA cm^{-2}, another phase minimum at frequencies below 1 Hz is present. This might be attributed to
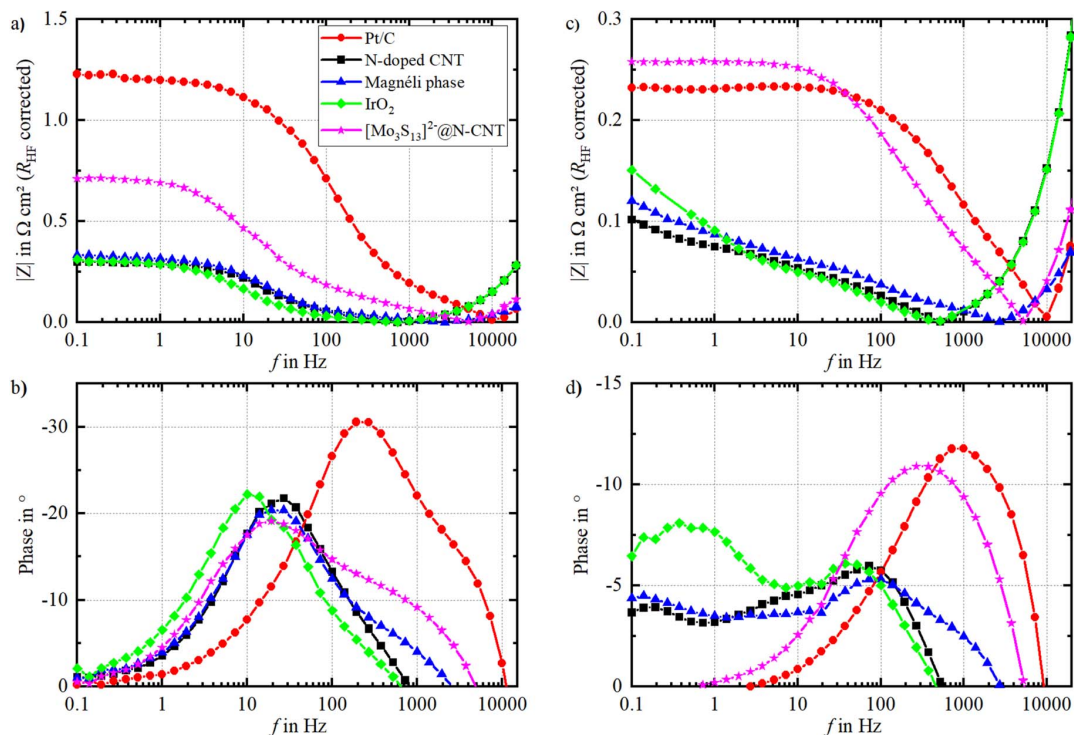
Figure 6. Presentation of the electrochemical impedance data in Bode plots. The R_{HF}-corrected amplitudes |Z| at 100 mA cm^{-2} and 500 mA cm^{-2} are shown in a) and c), respectively. The corresponding phase responses at 100 mA cm^{-2} are displayed in b) and at 500 mA cm^{-2} in d).
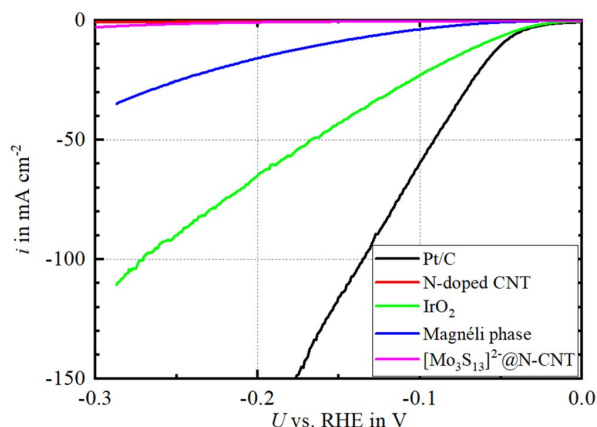
Figure 7. Catalyst-specific hydrogen evolution activity measured with linear sweep voltammetry in N_2-saturated sulfuric acid solution (0.5 M), a rotation speed of 1000 rpm and a sweep rate of 15 mV s^{-1}. The catalysts were collected from the PTEs after full cell experiments.

Figure 9. Catalyst-specific oxygen reduction activity measured by linear sweep voltammetry in O_2-saturated perchloric acid solution (0.1 M), a rotation speed of 1600 rpm and a sweep rate of 5 mV s^{-1}. The catalysts were collected from the PTEs after full cell experiments.
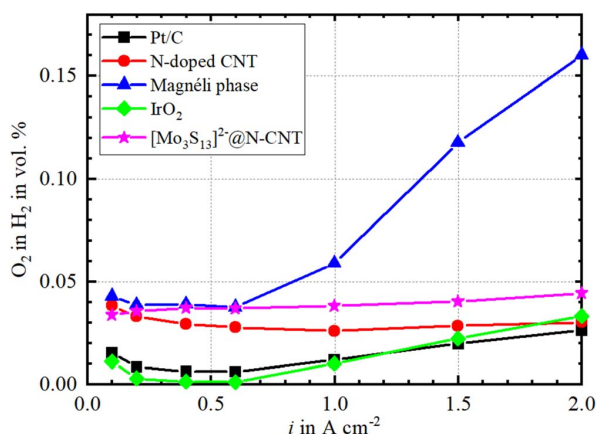

Figure 8. Measured oxygen in hydrogen volume fractions through Nafion 115 at 80 °C and ambient pressure.

changes of the mass transport, possibly caused by different electrode structures. As seen in the SEM images (Fig. 2), the surfaces of these three catalysts were noticeably smoother than of the carbon-based catalysts. The carbon-based catalysts show only one distinct phase minimum at higher frequencies with a higher absolute value. As seen in Fig. 6c), R_{CT} of $[Mo_3S_{13}]^{2-}$@N-CNT is higher than of N-doped CNT. Due to the deposition of the CNTs with $[Mo_3S_{13}]^{2-}$, the surface area of $[Mo_3S_{13}]^{2-}$@N-CNT is assumed to be higher than the surface area of the bare CNTs. As the capacitance correlates with the surface area, a higher capacitance follows for $[Mo_3S_{13}]^{2-}$@N-CNT. This results in a lower frequency for the phase minimum.

These findings could be proven by *ex situ* LSV in a RDE-setup (Fig. 7) in which the activity of the HER was measured. The observed trend in electrocatalytic activity for the HER is similar to the previously described data obtained from the Tafel plots in Fig. 5. Figure 7 clearly shows that Pt/C has the highest activity, followed by IrO$_2$ and the Magnéli phase. Although these three catalysts show different half-cell polarisations, they result in very similar polarisation behaviours in full cells (cf. Fig. 3 and Fig. 5). Apparently, the OER is still the limiting reaction when using these cathode catalysts. In contrast, the carbon-based electrocatalysts need high overpotentials to let the hydrogen evolution reaction occur (Fig. 7). In terms of the full cell polarisation behaviour (cf. Fig. 3), this results in a shift
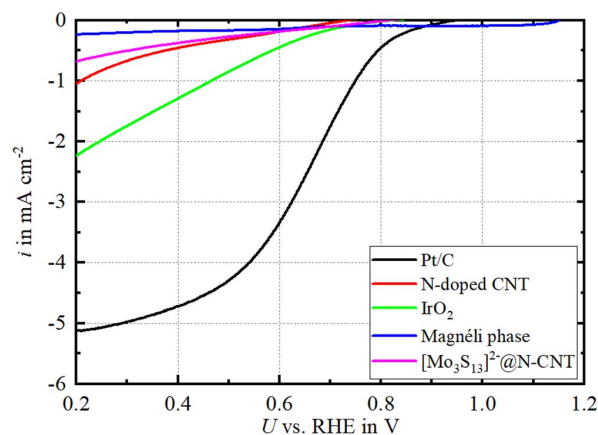
towards higher voltages. In contrast to the work of Holzapfel *et al.*,[32] the activity of $[Mo_3S_{13}]^{2-}$@N-CNT in this work is far lower. They assume that the catalyst passes a structural transformation at current densities higher than 2 A cm^{-2}, which leads to an enhanced electrochemical activity. Therefore, it can be possible that the catalyst in this work was not fully activated which would explain the low activity towards the HER. However, these findings can only give a theoretical indication, since the real performance is only visible in full cell experiments.

***Oxygen crossover.*—**The measured oxygen content in the hydrogen product gas, which was determined by gas chromatography, is shown in Fig. 8. Generally, the cells with PGM cathode catalysts show lower oxygen in hydrogen contents than the PGM-free configurations. For the well performing cell configurations (Pt/C, IrO$_2$ and Magnéli phase) the oxygen in hydrogen content is increasing with increasing current density. The measured oxygen contents for the two carbon-based catalysts remains almost constant over the investigated current range.

The cells using the PGM catalysts (Pt/C and IrO$_2$) show the lowest oxygen content. Additionally, the lowest cell voltages were obtained with these catalysts (cf. Fig. 3). It was expected that the oxygen volume fraction using Pt/C is low, because platinum is a good catalyst for the recombination of hydrogen and oxygen to water. Consequently, the major part of permeated oxygen recombines with evolving hydrogen. Below 1 A cm^{-2}, the measured oxygen fraction using IrO$_2$ is lower than with Pt/C. An explanation could be the catalyst loading of IrO$_2$, which is three times higher than the loading of Pt/C. It can be assumed that the surface area and thus, the number of active recombination sites, is higher. This eventually leads to a lower oxygen in hydrogen fraction at low current densities.

The measured oxygen content using N-doped CNT is higher than with the PGM catalysts. They approach similar contents at 2 A cm^{-2}. Compared to the bare nanotubes, the values using $[Mo_3S_{13}]^{2-}$@N-CNT are shifted to slightly higher oxygen in hydrogen volume fractions. Up to approximately 0.6 A cm^{-2}, the cells with the Magnéli phase catalyst and $[Mo_3S_{13}]^{2-}$@N-CNT show similar oxygen contents. A further increase of the current density results in a significant increase of the oxygen content when using the Magnéli phase catalyst. At 2 A cm^{-2}, the measured oxygen content in hydrogen with this catalyst is more than the fivefold value of Pt/C. From these results the recombination properties of the catalysts can be estimated qualitatively. The Magnéli phase catalyst appears to have the lowest activity, whereas the PGM catalysts (Pt/C
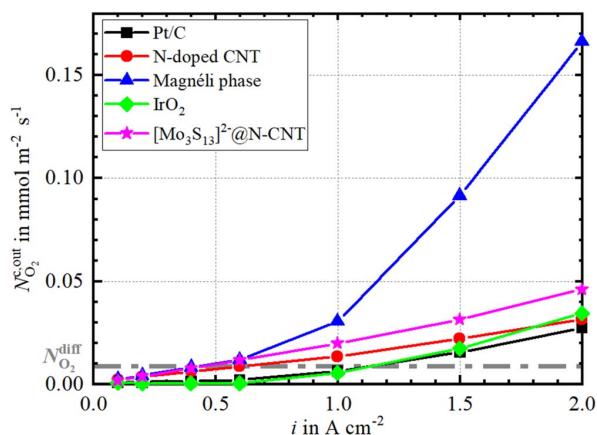
Figure 10. Cathodic oxygen flux through Nafion 115 at the cathode cell outlet using the different cathode electrocatalysts at 80 °C and ambient pressure.

and IrO$_2$) have a high recombination activity. The recombination activities of the two carbon-based catalysts should be somewhere in between.

This trend in recombination activity is supported by *ex situ* measurements, in which the ORR activity was determined by LSV (Fig. 9). The recombination of hydrogen and oxygen can occur via an electrochemical or a chemical pathway. In the used full cell setup, probably both pathways occur simultaneously. On electrically isolated particles, only the chemical pathway proceeds. We have tried to measure the chemical recombination rate by flushing the cathode side of the unpolarised cell with an O$_2$ in H$_2$ mixture of known concentration. Unfortunately, our setup was either not sensitive enough to measure changes in the gas composition or this approach was unable to mimic the experimental conditions in the cell during electrolysis.

As seen, the measurement of the pure chemical recombination rate is quite difficult and needs special experimental setups. Therefore, the activity for the oxygen reduction reaction of each catalyst will be used as a measure for their recombination activities.

According to Sabatier's principle, the interaction between a catalyst and the reactants should be neither too strong nor too weak. Platinum fulfils this requirement for hydrogen and oxygen. Consequently, it is the state of the art catalyst for hydrogen evolution, hydrogen oxidation and oxygen reduction.[4,49,50] Therefore, we assume that catalysts which show a high activity for the ORR also show high activities for the chemical recombination of hydrogen and oxygen.

The kinetics for the oxygen reduction reaction were determined similarly to the determination of the hydrogen evolution activity in the previous section (cf. Fig. 7). The results of the LSV measurements are displayed in Fig. 9. In general, the measured currents are significantly lower compared to the hydrogen evolution. This is caused by the complex, sluggish oxygen reduction kinetics which are accompanied by higher overpotentials. The state of the art cathode catalyst (Pt/C) shows the highest onset potential for the oxygen reduction reaction. IrO$_2$, N-doped CNT and [Mo$_3$S$_{13}$]$^{2-}$@N-CNT have a poorer activity for the ORR compared to platinum. The Magnéli phase catalyst shows almost no activity for the reaction, although a small amount of the mixed Ti-Ir phase exists alongside the pure Ti Magnéli phase. Thus, the electrocatalytic activity for the ORR according to the LSV measurements decreases in this order: Pt/C > IrO$_2$ > N-doped CNT > [Mo$_3$S$_{13}$]$^{2-}$@N-CNT > Magnéli phase. This qualitative trend in ORR activities fits well to the results in Fig. 8.

As already mentioned, the measured oxygen in hydrogen fraction using IrO$_2$ is lower than using Pt/C, although the ORR activity of Pt/C is higher. However, it has been reported elsewhere[4,51] that the activity of metallic Ir and IrO$_2$ regarding the oxygen reduction cannot compete with platinum. This explains the differences of the two PGM catalysts in Fig. 9 and at current densities above 1 A cm^{-2} in Fig. 8. Nonetheless, IrO$_2$ is a quite good HER catalyst as shown in the previous section. This is explained by a high affinity of the oxide surface to hydrogen, which is even higher compared to platinum.[24–26]

In contrast to the HER activity, the bare CNT catalyse the ORR better than the [Mo$_3$S$_{13}$]$^{2-}$@N-CNT. The role of doped carbon catalysts as a noble metal free alternative for the oxygen reduction reaction is of high interest in the field of PEM fuel cell research. In theirs review of using such catalysts in PEM fuel cells, Klingele *et al.*[52] and Liu *et al.*[53] explain the enhanced ORR activity of doped carbon materials with the polarisation of bonds. Introducing heteroatoms such as nitrogen into the graphitic structure results in a polarisation of the bonds neighbouring the dopant atom. It is assumed that the adsorption at such polarised carbon atoms facilitates oxygen adsorption, which leads to an enhanced ORR activity. As the application of the [Mo$_3$S$_{13}$]$^{2-}$–clusters onto the CNTs may block some of the active sites for oxygen adsorption, the decreased ORR activity in comparison to the bare CNTs can be explained. The catalytic activity of graphitic carbons for the recombination of hydrogen and oxygen is known in literature.[54,55]

Figure 10 shows the measured cathodic oxygen flux $N_{O_2}^{c,out}$ calculated from the data displayed in Fig. 8 according to Eq. 4. The measured oxygen fluxes increase with increasing current density. This phenomenon was measured and explained in previous works by Trinke *et al.* for both hydrogen and oxygen crossover.[5,19,23] The higher the aforementioned recombination activity of the used cathode catalyst is, the lower is the value of $N_{O_2}^{c,out}$. In a previous work, Trinke *et al.*[23] demonstrated the current dependency of oxygen crossover using Pt and a Pt-free cathode catalyst. The results show the same qualitative trend as in this work: The measured oxygen crossover flux with Pt-free catalysts is higher than with Pt.

Further, the diffusional oxygen flux $N_{O_2}^{diff}$ from anode and cathode, as defined in Eq. 5, is shown in Fig. 10 (dashed line). As mentioned previously, the permeation of oxygen not only proceeds by diffusive transport but also by convection. However, the ratio of both transport mechanisms during water electrolysis operation cannot be distinguished, since both occur simultaneously and additionally, the amount of recombined oxygen in unknown. Therefore, $N_{O_2}^{diff}$ should be measured at minimum when no permeated oxygen recombines with hydrogen. However, this is not the case no matter which catalyst was used. Consequently, the difference between $N_{O_2}^{diff}$ and the actually measured oxygen flux corresponds to the minimum amount of recombined oxygen. The more active a cathode catalyst was determined for the recombination reaction, the longer the curve falls below this theoretical minimum value. For Pt/C and IrO$_2$, 1 A cm^{-2} needs to be exceeded in order to measure higher values than $N_{O_2}^{diff}$. Using the Magnéli phase as a catalyst, 0.4 A cm^{-2} suffices to cross the theoretical value. Although the Magnéli phase catalyst barely showed an activity for the oxygen reduction reaction (cf. Fig. 9), the remaining catalytic activity seems to be high enough to let the permeated oxygen recombine almost completely at low current densities.

Further reasons for the current dependency of measured oxygen crossover can be found in the rate law for the chemical recombination reaction. If a rate law according to Eq. 6 is assumed for the recombination, then the recombination rate r_{rec} can be influenced by the concentration of hydrogen c_{H_2} or by the concentration of oxygen
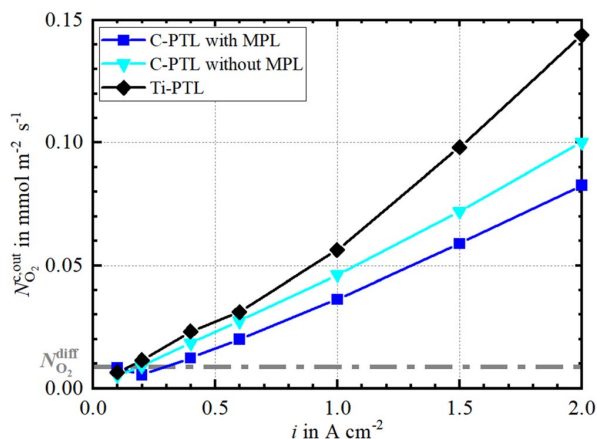
Figure 11. Cathodic oxygen flux through Nafion 115 using the Magnéli phase catalyst and different gas transport layers at the cathode at 80 °C and ambient pressure.

c_{O_2}. Both concentrations are influenced by the current density. As the concentration of hydrogen at the cathode can be assumed as overstoichiometrically high, the reaction rate solely depends on c_{O_2}.

$$r_{rec} = k_{rec} \cdot c_{H_2}^x \cdot c_{O_2}^y \qquad [6]$$

The high hydrogen flux at high current densities leads to a shorter residence time of permeated oxygen in the cathodic compartment. Hence, the time for recombination is higher at lower current densities. Further, the increasing reaction rate for the hydrogen evolution with higher current densities leads to an occupation of more catalytically active sites. The recombination reaction is suppressed by the ongoing adsorption of hydrogen. From the electrochemical point of view, it can be possible that the cathodic potentials may differ when comparing the different catalysts, as the hydrogen evolutions kinetics differ as well. There might be a dependency of the recombination and the cathodic potential.

Up to this point, it can be concluded that both N-doped CNT and $[Mo_3S_{13}]^{2-}$@N-CNTs show far slower hydrogen evolution kinetics, but the recombination activities remain high enough to let permeated oxygen recombine with hydrogen. The Magnéli phase catalyst is the only PGM-free catalyst showing similar HER kinetics as Pt, while its recombination activity is the lowest of all investigated catalysts. In order to evaluate the amount of permeated oxygen from the anode to the cathode during electrolysis, a cathode catalyst with a low or no recombination activity has to be used. Up to this point, only the Magnéli phase catalyst seems to be a proper catalyst for measuring the oxygen crossover during electrolysis while maintaining a good cell polarisation. However, the real amount of permeated oxygen is probably far higher than the results indicate.

Recombination properties of carbon-based porous transport layers.—As seen in the previous section, the two carbon-based catalysts showed quite good recombination properties, as their onset potentials for the ORR (Fig. 9) was only slightly lower than of IrO₂ and Pt/C and the measurable oxygen crossover was lower than the minimum diffusional crossover through a Nafion membrane (Fig. 10). As CNTs consist of graphitic carbon and as the state of the art PTLs for the cathode usually are made out of conductive, graphitic carbon, we wondered if the PTL material itself also shows a measurable catalytic activity for the recombination of oxygen and hydrogen to water.

For this study, the Magnéli phase catalyst was applied on the uncoated side of the half-coated CCM to obtain a "normal" catalyst coated membrane. The catalyst was chosen as it showed the lowest activity for the recombination reaction. For the characterisation of

the recombination properties of the PTL, the PTL material was varied: a carbon PTL with MPL (high surface area), the same PTL without MPL and a PTL made out of Ti-fibres. We assume that the titanium substrate will not catalyse the recombination reaction as the adsorption energy of hydrogen on titanium is too high.[4]

The measurement of oxygen in hydrogen content followed the same procedure as with the PTEs. The resulting oxygen fluxes at the cathode cell outlet are displayed in Fig. 11. In comparison to the measured oxygen flux with the Magnéli phase PTE in Fig. 10, the qualitative trend using the CCMs is rather linear with current density. The discrepancies between the PTE and CCM data is probably caused by different structures of the catalyst layer due to the manufacturing process.

As expected, the carbon-based PTLs show lower oxygen fluxes than the Ti-PTL and thus, we can assume that carbon-based PTLs have a noticeable catalytic activity for the recombination reaction. Moreover, it can be assumed that the higher the surface area of the PTL is, the more recombination sites exist. As the surface area of the PTL with MPL is higher than without the MPL, the lower oxygen flux when using the PTL with MPL can be explained. However, the diffusional oxygen flux at low current densities is again not reached. This is another indicator that the recombination properties of the used Magnéli phase catalyst are high enough to let the permeated oxygen recombine with hydrogen at low current densities.

Conclusions

In this work, two PGM and three PGM-free cathode catalysts for PEMWE were characterised regarding their electrochemical polarisation behaviour and their catalytic properties towards the hydrogen-oxygen recombination reaction. The investigated PGM catalysts (Pt/C and IrO₂) have shown the lowest cell voltages over the investigated current density range, whereas the usage of the two carbon-based PGM-free electrocatalysts (N-doped CNT and $[Mo_3S_{13}]^{2-}$@N-CNT) resulted in the highest cell voltages. Interestingly, the cell polarisation of the third PGM-free catalyst, namely Magnéli phase, was comparable to the PGM catalysts. The analysis of the cell voltage implied that the HER kinetics on the carbon-based catalyst have to be slower compared to the PGM catalysts. Further, the integral cell impedance spectra and *ex situ* LSV measurements for determining the HER activity prove the assumption of different HER kinetics.

The recombination properties of the five cathode catalysts were investigated by measuring the amount of permeated oxygen from the anode to the cathode by gas chromatography and by *ex situ* LSV measurements for determining the ORR activity. It was shown that catalysts with high ORR activities are better recombination catalysts as the measured oxygen in hydrogen content was lower than with using poor recombination catalysts. Using the Magnéli phase catalyst showed the highest oxygen in hydrogen fraction and concurrently the lowest ORR activity.

The relatively low measured oxygen contents when using the carbon-based catalysts raised the question if the commonly used carbon-based PTLs at the cathode also are catalytically active for the recombination of hydrogen and oxygen. For this additional study, CCMs with the Magnéli phase as cathodic catalyst were fabricated. The measured oxygen flux in the cathodic product gas showed lower fluxes with carbon PTLs than with a Ti-PTL. Further, it was shown that C-PTLs with larger surfaces (e.g. with MPL coating) exhibit more recombination sites than without a MPL.

However, the theoretical minimum oxygen flux caused by diffusion could not be reached in any configuration at current densities close to zero. This implies that even poor recombination catalysts, such as the Magnéli phase, are active enough to let an unknown amount of permeated oxygen recombine with hydrogen. The real amount of permeated oxygen is probably far higher than the results indicate. For a deeper understanding of the real oxygen crossover in PEM water electrolysis, an even more inactive catalyst

and an inactive PTL need to be used. Finding proper materials for this kind of study will be challenging.

In summary, it can be concluded that PGM-free cathode catalysts that can compete with the polarisation behaviour and HER kinetics of platinum, already exist. The recombination of permeated oxygen with evolving hydrogen will be reduced, which will lead to unpure hydrogen and inevitable processing of the product. However, the produced hydrogen gas is purified in the most cases anyway. Further, the long term stability of PGM-free catalysts needs to be assessed in future studies. An investigation of the mechanism of the recombination reaction on these catalysts is also of interest, as radical intermediates might be formed. The formation of reactive intermediates is undesirable, as they lead to a chemical degradation of the ionomer. Consequently, the possible advantage of the reduced radical formation needs to be investigated further in order to find alternative and cheap PGM-free cathode catalysts (e.g. Magnéli phase) to eventually replace platinum.

Acknowledgments

ORCID

Agate Martin https://orcid.org/0000-0003-4673-1135
Patrick Trinke https://orcid.org/0000-0002-0935-532
Chuyen Van Pham https://orcid.org/0000-0002-0284-8430
Melanie Bühler https://orcid.org/0000-0002-8764-4428
Markus Bierling https://orcid.org/0000-0002-4992-2095
Boris Bensmann https://orcid.org/0000-0001-8685-7192
Simon Thiele https://orcid.org/0000-0002-4248-2752
Richard Hanke-Rauschenbach https://orcid.org/0000-0002-1958-307X

References

1. K. Ayers, N. Danilovic, R. Ouimet, M. Carmo, B. Pivovar, and M. Bornstein, *Annu. Rev. Chem. Biomol. Eng.*, **10**, 219 (2019).
2. M. Carmo, D. L. Fritz, J. Mergel, and D. Stolten, *Int. J. Hydrog. Energy*, **38**, 4901 (2013).
3. O. T. Holton and J. W. Stevenson, *Platin Met. Rev.*, **57**, 259 (2013).
4. P. Quaino, F. Juarez, E. Santos, and W. Schmickler, *Beilstein J. Nanotechnol.*, **5**, 846 (2014).
5. P. Trinke, B. Bensmann, S. Reichstein, R. Hanke-Rauschenbach, and K. Sundmacher, *J. Electrochem. Soc.*, **163**, F3164 (2016).
6. C. V. Pham, A. Zana, M. Arenz, and S. Thiele, *ChemElectroChem*, **5**, 2672 (2018).
7. J. Deng, P. Ren, D. Deng, L. Yu, F. Yang, and X. Bao, *Energy Environ. Sci.*, **7**, 1919 (2014).
8. B. Hinnemann, P. G. Moses, J. Bonde, K. P. Jørgensen, J. H. Nielsen, S. Horch, I. Chorkendorff, and J. K. Nørskov, *J. Am. Chem. Soc.*, **127**, 5308 (2005).
9. A. B. Laursen, S. Kegnæs, S. Dahl, and I. Chorkendorff, *Energy Environ. Sci.*, **5**, 5577 (2012).
10. Q. Feng, X. Yuan, G. Liu, B. Wei, Z. Zhang, H. Li, and H. Wang, *J. Power Sources*, **366**, 33 (2017).
11. T. Jahnke et al., *J. Power Sources*, **304**, 207 (2016).
12. T. Sugawara, N. Kawashima, and T. N. Murakami, *J. Power Sources*, **196**, 2615 (2011).
13. A. Laconti, H. Liu, C. Mittelsteadt, and R. McDonald, *ECS Trans.*, **1**, 199 (2006).
14. V. Schröder, B. Emonts, H. Janßen, and H.-P. Schulze, *Chem. Eng. Technol.*, **27**, 847 (2004).
15. M. Zatoń, J. Rozière, and D. J. Jones, *Sustain. Energ. Fuels*, **1**, 409 (2017).
16. M. Chandesris, V. Médeau, N. Guillet, S. Chelghoum, D. Thoby, and F. Fouda-Onana, *Int. J. Hydrogen Energy*, **40**, 1353 (2015).
17. F. Fouda-Onana, M. Chandesris, V. Médeau, S. Chelghoum, D. Thoby, and N. Guillet, *Int. J. Hydrogen Energy*, **41**, 16627 (2016).
18. S. A. Grigoriev, K. A. Dzhus, D. G. Bessarabov, and P. Millet, *Int. J. Hydrogen Energy*, **39**, 20440 (2014).
19. P. Trinke, P. Haug, J. Brauns, B. Bensmann, R. Hanke-Rauschenbach, and T. Turek, *J. Electrochem. Soc.*, **165**, F502 (2018).
20. P. Trinke, G. P. Keeley, M. Carmo, B. Bensmann, and R. Hanke-Rauschenbach, *J. Electrochem. Soc.*, **166**, F465 (2019).
21. H. Ito, N. Miyazaki, M. Ishida, and A. Nakano, *Int. J. Hydrog. Energy*, **41**, 20439 (2016).
22. M. Schalenbach, T. Hoefner, P. Paciok, M. Carmo, W. Lueke, and D. Stolten, *J. Phys. Chem. C*, **119**, 25145 (2015).
23. P. Trinke, B. Bensmann, and R. Hanke-Rauschenbach, *Electrochem. Commun.*, **82**, 98 (2017).
24. C. Chabanier and D. Guay, *J. Electroanal. Chem.*, **570**, 13 (2004).
25. Y. Cho, A. Yu, C. Lee, M. H. Kim, and Y. Lee, *ACS Appl. Mater. Interfaces*, **10**, 541 (2018).
26. M. Blouin and D. Guay, *J. Electrochem. Soc.*, **144**, 573 (1997).
27. T. Röpke and S. Möller, *Katalysatoren für die elektrochemische Wasserstoffentwicklung* (DE 10 2009 002 326 A1 2010.10.14) (2010), https://patentimages.storage.googleapis.com/ae/63/e4/e0a7e26d824035/DE102009002326A1.pdf.
28. J. Zeng, Z. Chen, X. Zhao, W. Yu, S. Wu, J. Lu, K. P. Loh, and J. Wu, *ACS Appl. Nano Mater.*, **2**, 7969 (2019).
29. J. Ekspong, T. Sharifi, A. Shchukarev, A. Klechikov, T. Wågberg, and E. Gracia-Espino, *Adv. Funct. Mater.*, **26**, 6766 (2016).
30. T. F. Jaramillo, K. P. Jorgensen, J. Bonde, J. H. Nielsen, S. Horch, and I. Chorkendorff,, *Science*, **317** (2007).
31. K. Zhang, Y. Zhao, S. Zhang, H. Yu, Y. Chen, P. Gao, and C. Zhu, *J. Mater. Chem. A*, **2**, 18715 (2014).
32. P. Holzapfel, M. Bühler, D. Escalera-López, M. Bierling, F. Speck, K. Mayrhofer, S. Cherevko, C. V. Pham, and S. Thiele, *Small*, **16**, 2003161 (2020).
33. M. Bühler, F. Hegge, P. Holzapfel, M. Bierling, M. Suermann, S. Vierrath, and S. Thiele, *J. Mater. Chem. A*, **7**, 26984 (2019).
34. C. Klose, P. Trinke, T. Böhm, B. Bensmann, S. Vierrath, R. Hanke-Rauschenbach, and S. Thiele, *J. Electrochem. Soc.*, **165**, F1271 (2018).
35. S. A. Grigoriev, A. A. Kalinnikov, P. Millet, V. I. Porembsky, and V. N. Fateev, *J. Appl. Electrochem.*, **40**, 921 (2010).
36. H. Ito, T. Maeda, A. Nakano, and H. Takenaka, *Int. J. Hydrog. Energy*, **36**, 10527 (2011).
37. L. Haar, J. S. Gallagher, and G. S. Kell, *NBS/NRC Steam Tables* (Hemisphere Publ. Corporation, Washington) (1984).
38. T. Schuler, T. J. Schmidt, and F. N. Büchi, *J. Electrochem. Soc.*, **166**, F555 (2019).
39. F. Hegge, R. Moroni, P. Trinke, B. Bensmann, R. Hanke-Rauschenbach, S. Thiele, and S. Vierrath, *J. Power Sources*, **393**, 62 (2018).
40. C.-H. Lin, *Appl. Energy*, **104**, 898 (2013).
41. S. H. Frensch, A. C. Olesen, S. S. Araya, and S. K. Kær, *Electrochim. Acta*, **263**, 228 (2018).
42. M. Suermann, T. J. Schmidt, and F. N. Büchi, *Electrochim. Acta*, **211**, 989 (2016).
43. E. Barsoukov and J. R. Macdonald, *Impedance Spectroscopy: Theory, Experiment, and Applications* (Wiley, Hoboken NJ) (2018).
44. P. Chulkin and P. Data, *J. Vis. Exp.*, **140**, e56611 (2018).
45. M. R. Schuster, *Mechanistische Untersuchung und Modellierung der Anodenreaktion in der Karbonat-Brennstoffzelle* (University of Ulm, Ulm, Germany) (2010).
46. C. Rozain and P. Millet, *Electrochim. Acta*, **131**, 160 (2014).
47. S. Siracusano, N. van Dijk, E. Payne-Johnson, V. Baglio, and A. S. Aricò, *Appl. Catal. B*, **164**, 488 (2015).
48. S. Siracusano, S. Trocino, N. Briguglio, V. Baglio, and A. S. Aricò, *Materials (Basel, Switzerland)*, **11**, 1368 (2018).
49. A. Kulkarni, S. Siahrostami, A. Patel, and J. K. Nørskov, *Chem. Rev.*, **118**, 2302 (2018).
50. Z. W. Seh, J. Kibsgaard, C. F. Dickens, I. Chorkendorff, J. K. Nørskov, and T. F. Jaramillo, *Science (New York, N.Y.)*, **355** (2017).
51. E. Antolini, *ACS Catal.*, **4**, 1426 (2014).
52. M. Klingele, C. V. Pham, A. Fischer, and S. Thiele, *Fuel Cells*, **16**, 522 (2016).
53. X. Liu and L. Dai, *Nat. Rev. Mater.*, **1**, 760 (2016).
54. H. Dietz, L. Dittmar, D. Ohms, M. Radwan, and K. Wiesener, *J. Power Sources*, **40**, 175 (1992).
55. K. Waki, R. A. Wong, H. S. Oktaviano, T. Fujio, T. Nagai, K. Kimoto, and K. Yamada, *Energy Environ. Sci.*, **7**, 1950 (2014).

6 Optimized Recombination Interlayer for Lower Anodic Hydrogen Contents

In section 2.2.4, several mitigation strategies for reduced gas crossover were presented. One known and well-working strategy is the implementation of a recombination catalyst, such as platinum, as an interlayer in the membrane. In a previous work of Klose *et al.*[125], the authors gave a theoretical examination of the impact of the interlayer position in the membrane on the resulting hydrogen in oxygen content. The assessment predicted that depending on the desired operating conditions (e. g. symmetric or asymmetric pressure), the position of the interlayer must be well chosen in order to achieve the greatest reduction of the hydrogen content. This conclusion raised the last research question, dealing with the optimized design of a recombination interlayer.

Research Question 5: What is important for the design of a recombination interlayer within the polymer electrolyte membrane?

The research question is investigated in a peer-reviewed short communication entitled "Proving the Importance of Pt-Interlayer Position in PEM-WE Membranes for the Effective Reduction of the Anodic Hydrogen Content" (*J. Electrochem. Soc.* 168(9):094509, 2021). The original article follows behind these introductory and summarizing paragraphs on the concept and key findings of the article.

Based on the theoretical examination of Klose *et al.*[125], the impact of the platinum interlayer position on the resulting anodic hydrogen content is investigated experimentally in this contribution. For this, three CCMs with interlayers at different positions (close to the cathode, in the middle, close to the anode) and a reference CCM without interlayer are fabricated. Then, the CCMs are analysed with regard to their electrical performance and their hydrogen crossover characteristics at various asymmetric pressure conditions.

The analysis of the obtained polarisation curves reveals that the implementation of a platinum interlayer results in a comparable performance, without a noticeable impact on the membrane resistance. Even at the maximum current density of $3.6\,\mathrm{A\,cm^{-2}}$, a cell voltage of $2\,\mathrm{V}$ is not exceeded. This is an important property to be competitive with membranes without an interlayer. Moreover, the measurement of the anodic gas composition at ambient pressure conditions reveals that any CCM with an interlayer reduces the anodic hydrogen content compared to the CCM without interlayer. At increased cathode

pressures, the impact of the interlayer position is pronounced clearly. The CCM with an interlayer close to the cathode barely achieves a significant reduction of the hydrogen content, whereas the content is cut in half with the interlayer in the middle. The greatest reduction to almost zero percent hydrogen in oxygen is achieved with the interlayer positioned closely to the anode. This is explained with the gradient in the oxygen concentration in the membrane, decreasing from anode to cathode. Therefore, less oxygen is present for the recombination reaction at the interlayer close to the cathode.

Moreover, it is shown that the available oxygen concentration for the recombination cannot only be controlled by the interlayer position, but also by increasing the anode pressure. Higher anode pressures result in a higher overall oxygen concentration within the membrane, which makes the recombination reaction more effective at every interlayer position. Hence, the anodic hydrogen content is reduced even further, especially at low current densities.

With regard to the research question, it is summarized that the position of a recombination catalyst interlayer in the membrane has a significant impact on the effectiveness of the recombination reaction. An interlayer positioned closely to the anode achieves the greatest reduction of the anodic hydrogen content at asymmetric pressure conditions (cathode pressure is higher than anode pressure), which is valuable for keeping safe gas mixtures.

Communication—Proving the Importance of Pt-Interlayer Position in PEMWE Membranes for the Effective Reduction of the Anodic Hydrogen Content

Agate Martin,[1,=] Dunia Abbas,[2,3,=] Patrick Trinke,[1] Thomas Böhm,[2] Markus Bierling,[2,3] Boris Bensmann,[1,z] Simon Thiele,[2,3] and Richard Hanke-Rauschenbach[1]

[1]*Leibniz University Hannover, Institute of Electric Power Systems, 30167 Hannover, Germany*
[2]*Forschungszentrum Jülich GmbH, Helmholtz Institute Erlangen-Nürnberg for Renewable Energy (IEK-11), 91058 Erlangen, Germany*
[3]*Department of Chemical and Biological Engineering, Friedrich-Alexander-Universität Erlangen-Nürnberg, 91058 Erlangen, Germany*

Gas crossover through the membrane poses a significant challenge to proton exchange membrane water electrolysers. This work investigates the influence of the position of platinum-based recombination interlayers integrated in the membrane on the anodic hydrogen in oxygen content. The results show that all interlayer positions reduce the anodic hydrogen content without performance losses compared to the reference without interlayer. However, an interlayer positioned closer to the anode is more effective than closer to the cathode. Further, the effect of the interlayer is more pronounced with increasing anode pressure.

Proton exchange membrane water electrolysis (PEMWE) is an emerging technology for the production of green hydrogen. Major technology goals are improved system reliability especially in dynamic operation, the operation at elevated cathode pressure, and the reduction of membrane thickness.[1–3] However, with increasing operating pressure as well as with decreasing membrane thickness, hydrogen crossover from cathode to anode through the membrane increases[4–6] and results in the formation of explosive gas mixtures for H_2 in O_2 contents above 4 vol.%.[7] Therefore, PEM electrolysers are typically operated up to a safety limit around 2 vol.% H_2 in O_2.[1,3,7,8] Research activities have focused on different strategies to limit the H_2 in O_2 content in PEM electrolysers,[6] e.g. by integrating recombination catalysts i) in the gas separator,[8] ii) directly on the anode[9] or iii) inside the membrane.[10] The latter work has shown that a platinum interlayer reduced the anodic H_2 in O_2 content significantly. It also provided a theoretical assessment of the ideal position of a recombination layer for the reduction of both, hydrogen and oxygen gas fluxes across the membrane.

The present work studies the influence of the Pt-interlayer position on the H_2 in O_2 content experimentally. Catalyst coated membranes (CCMs) with recombination interlayers (IL) close to the anode (IL_an), in the middle (IL_mid), close to the cathode (IL_cat) and a reference without interlayer (no_IL) were fabricated and examined regarding their polarisation behaviour and hydrogen crossover properties at different pressure conditions.

Materials and Methods

Catalyst Coated Membranes.— *Spray-Coating of Membranes.—*A spray coater (Sono-Tek) was used to fabricate Nafion membranes onto a PTFE substrate. A dispersion of Nafion D2021 (FuelCellStore) and isopropanol in a weight ratio of 3.34/10 was mixed. For the Pt-interlayers, a mixture of Pt-nanoparticles (Sigma-Aldrich, particle size < 50 nm), Nafion D2020 (FuelCellStore) and isopropanol in a weight ratio of 0.0043/1.43/10 was stirred for 48 h. Nafion layers were sprayed with a flow rate of 0.9 ml min^{-1} and a nozzle speed of 100 mm s^{-1} at 65 °C to ensure complete solvent evaporation. For no_IL, 36 consecutive spray runs were conducted. For IL_an and

IL_cat, 30 spray runs were performed, while 17 runs were required for IL_mid. Subsequently, the Pt-interlayer was deposited in 22 runs with a flow rate of 0.3 ml min^{-1} and a nozzle speed of 140 mm s^{-1}. A second Nafion layer was then deposited on top of the membranes (IL_an and IL_cat in 4 runs; IL_mid in 17 runs). The Pt-loading was determined based on the weight gain as 0.01 mg$_{Pt}$ cm^{-2}. The final membrane thickness in the dry state yielded 110 ± 5 μm.

*Electrode Fabrication.—*Decal electrodes with loadings of 0.16 ± 0.05 mg$_{Pt}$ cm^{-2} (with I/C = 0.65) for the cathode and 2 ± 0.3 mg$_{Ir}$ cm^{-2} (with I/C = 0.13) for the anode were fabricated using Nafion D2021 (FuelCellStore) as binder, TEC10V40E (Tanaka) as cathode catalyst and Elyst Ir75 (Umicore) as anode catalyst. CCMs were fabricated by hot pressing 4 cm^2 electrodes onto the membranes at 160 °C at a pressure of 2 MPa for 5 min.

Test Setup.— *Cell Assembly.—*The used 4 cm^2 cell, designed by Fraunhofer ISE,[11] is comprised of gold-coated titanium blocks and is equipped with PEEK isolation frames and flat sealings (60FC-FKM200, 0.8 mm, Freudenberg). The contact force was monitored with a load cell (K-14, GM77, Lorenz Messtechnik GmbH).

On the cathode, a carbon porous transport layer (PTL, H23I2, 210 μm, Freudenberg) and on the anode a titanium PTL (1 mm, grade 1, 2GDL40–1.00, Bekaert) were used. The CCMs were assembled in dry state in the cell.

*Testing Periphery.—*The measurements were performed with an E100 test station (Greenlight Innovation). A BCS815 potentiostat (BioLogic) was used as current source. The analysis of the dried anodic product gas with a gas chromatograph (GC, 490 μGC System, Agilent) is described in Refs. 6, 10 and 12.

As high hydrogen contents were expected at low current densities and high cathode pressures, the anode product gas was diluted with an additional flow of oxygen (0.04 g min^{-1} or $N_{O_2}^{dil} = 2.167 \cdot 10^{-5}$ mol s^{-1}) applied with a mass flow controller (EL-FLOW Prestige, Bronkhorst) directly behind the anode outlet.

Measurement Protocol.—After cell assembly, the cell was mounted into the test station and was conditioned thermally for 1 h at the measurement temperature of 80 °C. Then, the compression force of 4 kN was applied.

[=]These authors contributed equally to this work.
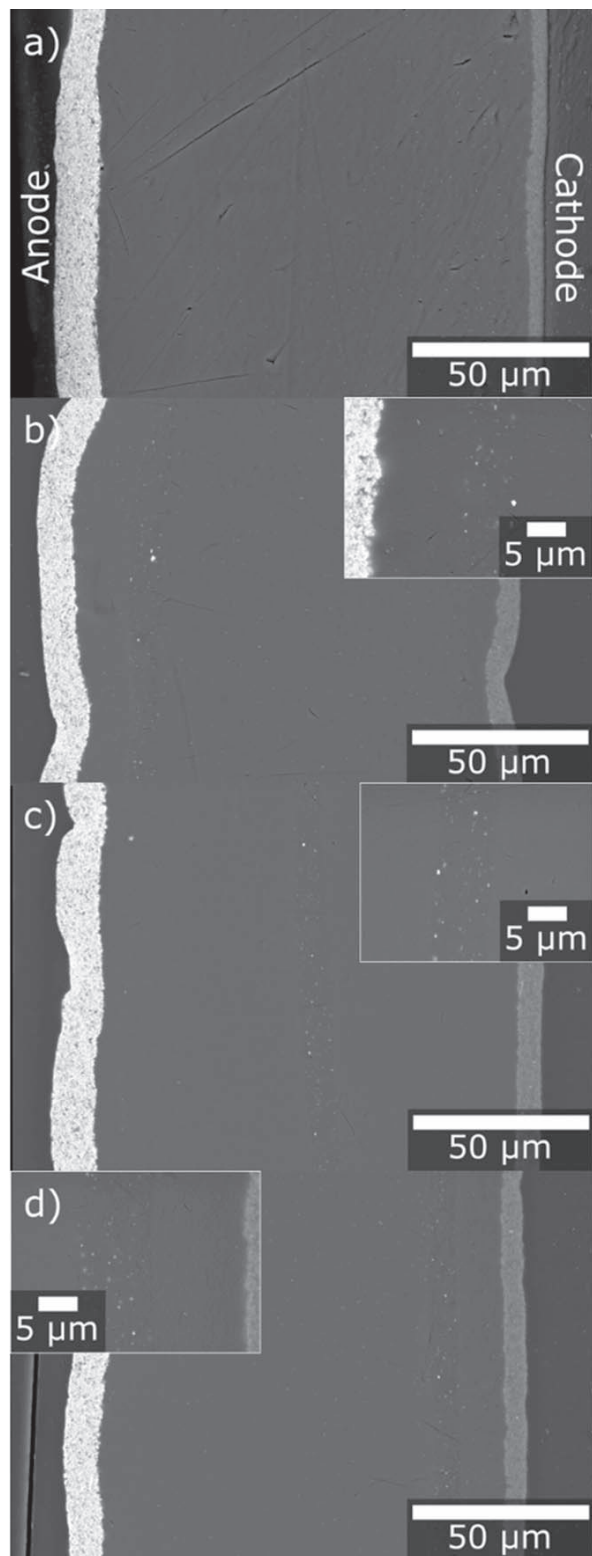[z]E-mail: boris.bensmann@ifes.uni-hannover.de

Figure 1. Cross-sections of (a) no_IL, (b) IL_an, (c) IL_mid, and (d) IL_cat after electrochemical characterisation. Additional insets with higher magnification for a representation of the Pt-interlayers are provided.
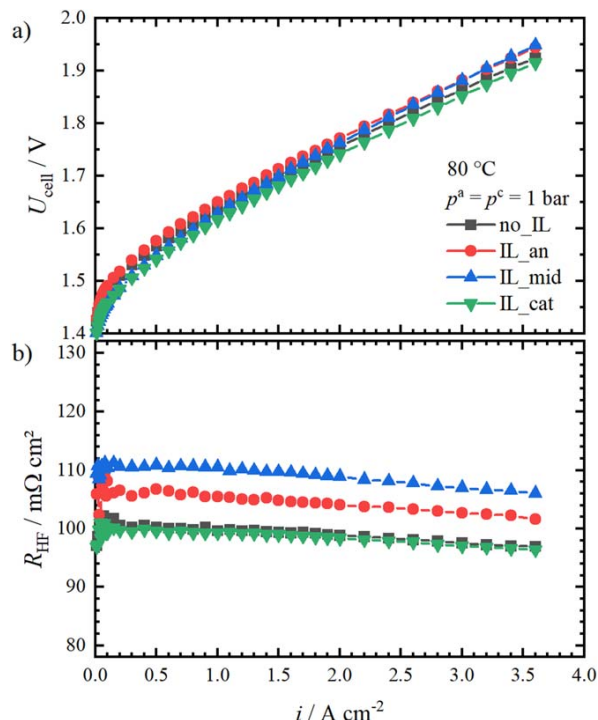

Figure 2. Polarisation behaviour of all investigated CCMs in (a) and their R_{HF} in (b).

Hydrogen Crossover.—A galvanostatic step profile of eight current density steps from 0.1 A cm^{-2} to 3.5 A cm^{-2} was used for monitoring the H_2 in O_2 content via GC. Each current density was held until a constant GC-signal was reached.

This procedure was repeated for three absolute pressure combinations ($p^c = 1$ bar and $p^a = 1$ bar, $p^c = 10$ bar and $p^a = 1$ bar, $p^c = 10$ bar and $p^a = 5$ bar). At ambient pressure, two cycles were performed in order to purge the test station.

Polarisation Behaviour.—After the crossover measurements, polarisation curves were recorded from 0.01 A cm^{-2} to 3.6 A cm^{-2} in logarithmic steps until 2 A cm^{-2} and then with steps of 0.2 A cm^{-2}. The holding time was 10 s per step. For the determination of the high frequency resistance R_{HF}, each current step was followed by an electrochemical impedance measurement between 10 kHz and 100 Hz and a current amplitude of 10%. R_{HF} was obtained by interpolating the Nyquist plots at the intercept with the real axis. The measurement was repeated three times and the third cycle was used for evaluation.

SEM Cross-Sections.—Cross-sections of *post mortem* CCMs were prepared by embedding the samples in epoxy resin, followed by grinding and polishing of the embedded samples. The cross-sections were imaged by SEM (Zeiss Crossbeam 540, BSD detector) after Au-sputtering.

Results and Discussion

SEM Cross-Sections.—Figure 1 shows cross-sections of the tested CCMs after disassembly of the cells. The overall membrane thicknesses range from 110 to 120 μm. The Pt-interlayers show thicknesses of approximately 7 to 12 μm close to the anode (Fig. 1b), in the middle (Fig. 1c), and close to the cathode (Fig. 1d).
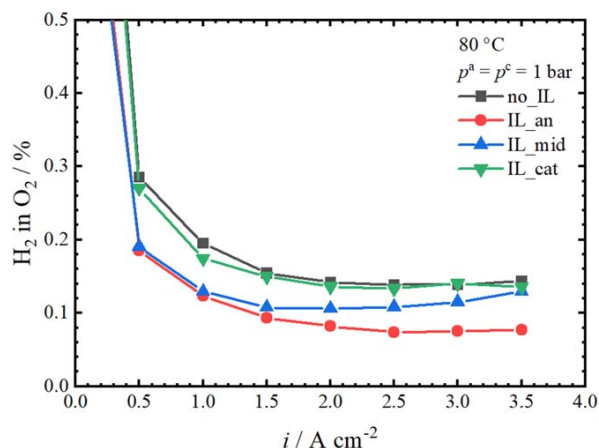
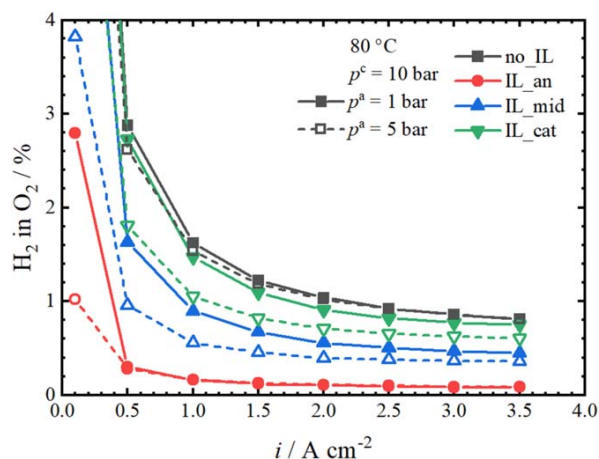**Figure 3.** H_2 in O_2 contents of the investigated CCMs at ambient pressure.

Figure 4. H_2 in O_2 contents at elevated cathode pressure $p^c = 10$ bar and different anode pressures: $p^a = 1$ bar (filled symbols) and $p^a = 5$ bar (hollow symbols).

Polarisation Behaviour.—The measured cell polarisation behaviour at 80 °C and ambient pressure is shown in Fig. 2. All CCMs show similar and good electrochemical performance with voltages below 2 V even at high current densities (Fig. 2a). The maximum voltage deviation at 3.6 A cm^{-2} is 33 mV.

The ohmic resistance of the interlayer membranes are approximated with the measured high frequency resistance R_{HF}. As displayed in Fig. 2b), R_{HF} decreases slightly with current density. This temperature effect was already explained previously.[13,14] IL_mid shows the highest R_{HF} (110 mΩ cm^2 at 1 A cm^{-2}), whereas IL_cat shows the lowest value (99 mΩ cm^2 at 1 A cm^{-2}). The differences between the R_{HF} values might be attributed to slight deviations in membrane thicknesses or tolerances due to cell assembly. Nonetheless, all measured R_{HF} values comply with literature values for slightly thicker commercial Nafion membranes (~110 mΩ cm^2 for N115).[12,15] Hence, the incorporation of the Pt-interlayer into the membrane has no apparent effect on R_{HF}. This is in contrast to the previous work of Klose *et al.*[10] and may result from the reduced loading or an improved manufacturing process.

In summary, these results show that the integration and the position of a Pt-interlayer into the membrane does not significantly affect the electrochemical polarisation behaviour. The minor deviations provide a good base for evaluation of the CCMs with regards to their crossover properties.

Hydrogen crossover.—The Pt-interlayers in the membranes are intended to function as a recombination layer for permeating product gases. For the evaluation of their recombination abilities, the anodic hydrogen content is used as a measure. Since the anodic product gas was diluted with an additional oxygen flux $N_{O_2}^{dil}$, the measured hydrogen content at the GC $\phi_{H_2}^{GC}$ is described by Eq. 1, where the evolved oxygen flux equals $N_{O_2}^{evo} = \frac{i}{4 \cdot F}$ and $N_{H_2}^{cross}$ is the hydrogen crossover flux.

$$\phi_{H_2}^{GC} = \frac{N_{H_2}^{cross}}{N_{O_2}^{evo} + N_{O_2}^{dil} + N_{H_2}^{cross}} \qquad [1]$$

The real hydrogen content $\phi_{H_2}^{real}$ can be determined by converting Eq. 1 to $N_{H_2}^{cross}$ and inserting it then into Eq. 2.

$$\phi_{H_2}^{real} = \frac{N_{H_2}^{cross}}{N_{O_2}^{evo} + N_{H_2}^{cross}} = \frac{\phi_{H_2}^{GC} \cdot (N_{O_2}^{evo} + N_{O_2}^{dil})}{N_{O_2}^{evo} + \phi_{H_2}^{GC} \cdot N_{O_2}^{dil}} \qquad [2]$$

Figure 3 shows the resulting H_2 in O_2 content for ambient pressure operation. The hydrogen content follows the expected qualitative course for all four experiments. As expected, the highest hydrogen contents are obtained with no_IL. Using IL_cat leads to contents in a similar range. With the other two samples (IL_an and IL_mid), noticeably lower hydrogen contents are obtained. The lowest values are obtained with IL_an. At 3 A cm^{-2}, a reduction of 43% (from 0.14% to 0.08%) was achieved with this CCM. Since hydrogen is still detected on the anode, the loading of the recombination catalysts, and thus the available catalyst surface area, might be too small or the oxygen crossover is not high enough for a complete recombination of hydrogen at the Pt-interlayer.

The impact of the interlayer positioning on the anodic hydrogen content is more pronounced at an elevated cathode pressure of 10 bar combined with atmospheric anode pressure, as seen in Fig. 4. Here, the content remains the highest when no interlayer is used.

The differences in hydrogen content between the CCMs with and without interlayer result from the fact that the amount of available oxygen and hydrogen at the interlayer depends on the interlayer position. Generally, the total amount of oxygen available by permeation through the membrane is less than that of hydrogen. First, the produced amount of oxygen is only half of that of hydrogen. Second, considering that most of the gas permeates in the aqueous phase of the membrane, less oxygen than hydrogen permeates, since the diffusivity of oxygen in water is lower than of hydrogen.[4,16,17] Therefore, it can be assumed that more hydrogen recombines in the vicinity of the anode due to the higher oxygen concentration.

Up to this point, it can be summarized that for electrolysis operation under ambient anode conditions, an interlayer near the anode achieves the greatest impact regarding the reduction of the anodic H_2 in O_2 content. Consequently, the available oxygen amount at the recombination interlayer is identified as a crucial factor for the recombination reaction.

In a further experiment, it was therefore investigated how an increase of the oxygen concentration affects the recombination efficiency of the different interlayer positions. This was achieved by elevating the anode pressure from ambient to 5 bar, whereas the cathode was kept at 10 bar. The resulting hydrogen contents at the anode are shown in Fig. 4.

The general trend remains: the closer the interlayer is positioned to the anode, the lower is the resulting H_2 in O_2 content. Regarding the reference case without interlayer, the elevation of anode pressure has only a minor effect, leading to nearly identical hydrogen contents.

The incorporation of any interlayer leads to a noticeable reduction of the hydrogen content, especially at low current densities up to 0.5 A cm^{-2}. Regarding IL_cat, the enhancement of oxygen

pressure reduces the hydrogen content by 34% at 0.5 A cm^{-2} compared to the atmospheric anode operation (from 2.73% to 1.81%). For IL_mid, the enhanced anode pressure even leads to a reduction of 41% (from 1.63% to 0.96%). It can be assumed that a further increase in anode pressure will lead to a further reduction of the anodic hydrogen content if the interlayer is positioned in the center or closer towards the cathode.

For IL_an, a further reduction of the H$_2$ in O$_2$ content cannot be observed for higher current densities. Therefore, it can be assumed that the oxygen concentration at ambient anode pressure is already sufficiently high for the recombination at high current densities for this interlayer position. Consequently, at an anode pressure of 5 bar, there should be sufficient oxygen for a full hydrogen recombination. This finding emphasizes that the employed Pt-loading in this work is not high enough for a complete recombination of the permeating hydrogen flux in comparison to the previous work of Klose *et al.*[10] who used twice the Pt-loading.

Summary

This contribution provides experimental proof for the importance and the effect of the position of recombination catalyst layers within PEMWE membranes for the reduction of the anodic hydrogen content. It was shown that the polarisation behaviour is not significantly affected by the Pt-interlayers and their positions. Furthermore, each CCM with interlayer reduced the measurable anodic hydrogen content in comparison to the reference CCM without interlayer. As expected from the theoretical assessment of Klose *et al.*[10] the strongest reduction was observed with the interlayer close to the anode. This can be explained by the available amount of dissolved oxygen in the membrane, which decreases towards the cathode and leads to a higher recombination rate of hydrogen and oxygen closer to the anode. The aforementioned theoretical assessment and the experimental results in this work suggest that a recombination interlayer close to the anode is recommended, if the hydrogen crossover should be minimized for maintaining a safe anodic gas composition.

As the available amount of oxygen at the interlayer seems to be the limiting factor for the recombination reaction, two optimisation strategies are possible for a PEM electrolyser with recombination catalysts within the membrane: i) positioning the interlayer close to the anode, or ii) elevating the anode pressure, to maximize the available concentration of oxygen at the interlayer. In order to improve the recombination effect at minimal costs, the position of the interlayer, the catalyst loading and the operating conditions need to be optimized.

In summary, the results of this study confirm that Pt-interlayers are a suitable strategy to reduce the H$_2$ in O$_2$ content in PEMWE, especially for thin membranes and elevated cathode pressures. This improvement can help to reduce safety issues and consolidate PEMWE as a key technology for hydrogen generation.

ORCID

Agate Martin https://orcid.org/0000-0003-4673-1135
Dunia Abbas https://orcid.org/0000-0002-3938-0026
Patrick Trinke https://orcid.org/0000-0002-0935-5321
Thomas Böhm https://orcid.org/0000-0003-2036-2159
Markus Bierling https://orcid.org/0000-0002-4992-2095
Boris Bensmann https://orcid.org/0000-0001-8685-7192
Simon Thiele https://orcid.org/0000-0002-4248-2752
Richard Hanke-Rauschenbach https://orcid.org/0000-0002-1958-307X

References

1. M. Schalenbach, M. Carmo, D. L. Fritz, J. Mergel, and D. Stolten, *Int. J. Hydrog. Energy*, **38**, 14921 (2013).
2. K. Ayers, N. Danilovic, R. Ouimet, M. Carmo, B. Pivovar, and M. Bornstein, *Annu. Rev. Chem. Biomol. Eng.*, **10**, 219 (2019).
3. M. Schalenbach, *Int. J. Hydrog. Energy*, **41**, 729 (2016).
4. M. Schalenbach, T. Hoefner, P. Paciok, M. Carmo, W. Lueke, and D. Stolten, *J. Phys. Chem. C*, **119**, 25145 (2015).
5. M. Bernt, J. Schröter, M. Möckl, and H. A. Gasteiger, *J. Electrochem. Soc.*, **167**, 124502 (2020).
6. P. Trinke, P. Haug, J. Brauns, B. Bensmann, R. Hanke-Rauschenbach, and T. Turek, *J. Electrochem. Soc.*, **165**, F502 (2018).
7. H. Janssen, J. C. Bringmann, B. Emonts, and V. Schroeder, *Int. J. Hydrog. Energy*, **29**, 759 (2004).
8. S. A. Grigoriev, P. Millet, S. V. Korobtsev, V. I. Porembskiy, M. Pepic, C. Etievant, C. Puyenchet, and V. N. Fateev, *Int. J. Hydrog. Energy*, **34**, 5986 (2009).
9. N. Briguglio, S. Siracusano, G. Bonura, D. Sebastián, and A. S. Aricò, *Appl. Catal. B*, **246**, 254 (2019).
10. C. Klose, P. Trinke, T. Böhm, B. Bensmann, S. Vierrath, R. Hanke-Rauschenbach, and S. Thiele, *J. Electrochem. Soc.*, **165**, F1271 (2018).
11. Fraunhofer Institute for Solar Energy Systems ISE, *Fraunhofer ISE—Annual Report 2020/2021* (Freiburg, Germany) (2021).
12. P. Trinke, G. P. Keeley, M. Carmo, B. Bensmann, and R. Hanke-Rauschenbach, *J. Electrochem. Soc.*, **166**, F465 (2019).
13. T. Schuler, T. J. Schmidt, and F. N. Büchi, *J. Electrochem. Soc.*, **166**, F555 (2019).
14. M. Suermann, T. J. Schmidt, and F. N. Büchi, *Electrochim. Acta*, **211**, 989 (2016).
15. B. Pivovar and Y. S. Kim, *J. Electrochem. Soc.*, **154**, B739 (2007).
16. T. Sakai, H. Takenaka, and E. Torikai, *J. Electrochem. Soc.*, **133**, 88 (1986).
17. H. Ito, T. Maeda, A. Nakano, and H. Takenaka, *Int. J. Hydrog. Energy*, **36**, 10527 (2011).

7 Summary, Conclusion and Outlook

In this chapter, the collected findings are arranged in the context of this work. The purpose of this thesis is to contribute knowledge on hydrogen and oxygen crossover in PEM water electrolysis, being a promising technology for the production of green hydrogen. The consideration of gas crossover is important because it is identified to be a crucial mass transport phenomenon affecting several development goals for the technology, such as the material durability, the efficiency and the safe operation of the electrolyzer.

The scientific contribution of this work is structured in five research questions. First, experimental investigations dealing with the impact of operating variables and design variables on hydrogen crossover are presented (research questions 1 to 3). Then, approaches towards the precise measurement of the oxygen crossover during electrolysis operation are provided (research question 4). Lastly, a study on the optimized design of recombination interlayers for mitigated gas crossover in PEM water electrolysis is shown (research question 5). Below, each research question is answered explicitely, by briefly summarizing and concluding the main results with respect to gas crossover, followed by an outlook.

Research Question 1: How does cell compression affect hydrogen crossover?

Summary: This question was examined in section 4.1, using a typical material combination for PEM-WE cells (carbon PTL at cathode, CCM based on Nafion™ 212 and titanium PTL at anode) at different compressed states.

The results for this particular system at ambient pressure show that the hydrogen crossover flux is not affected by the cathode compression at low current densities up to $1\,\mathrm{A\,cm^{-2}}$. At this operating point, a hydrogen crossover flux of $0.1\,\mathrm{mmol\,s^{-1}\,m^{-2}}$ is observed for all compression levels. Above this current density, the hydrogen crossover flux increases with compression. More precisely, it is observed that an increase of the cathode compression by $75\,\mathrm{\mu m}$ results in a more than doubled hydrogen crossover flux (from $0.25\,\mathrm{mmol\,s^{-1}\,m^{-2}}$ to $0.6\,\mathrm{mmol\,s^{-1}\,m^{-2}}$) at $3\,\mathrm{A\,cm^{-2}}$.

Conclusion: The findings are explained with a decreasing porosity of the cathode catalyst layer with increasing compression. Especially at the lands of the flow field, where the contact pressure is the highest throughout the geometric cell area, a significant reduction of the pore space and the interface between the pore space and ionomer, is expected. This restricted transfer of dissolved hydrogen into the gaseous state is increasingly hindered at higher compression levels. Consequently, the dissolved hydrogen concentration increases

with the current density and the compression, resulting in higher hydrogen crossover fluxes.

Outlook: The same qualitative relationship between compression and hydrogen crossover is expected for other material configurations. For thicker membranes, which are still commonly used at industrial and laboratory scale, it is expected that the compression effect on hydrogen crossover should become noticeable at a higher current density than reported here ($1\,\mathrm{A\,cm^{-2}}$), because the initial driving force for crossover is lower. Moreover, it is expected that carbon PTLs of higher strength should lead to a different compression profile of the cathode catalyst layer, which may reduce hydrogen crossover.

Research Question 2: How do high current densities above $5\,\mathrm{A\,cm^{-2}}$ affect hydrogen crossover?

Summary: For the investigation of this question, a typical PEM-WE cell setup based on commercially available materials (carbon PTL at cathode, commercial CCM based on Nafion™ 212 and titanium PTL at anode) is used in section 4.2.

The analysis reveals a general increase of hydrogen crossover over current density at ambient pressure. However, a transition between various slopes is observed. The expected linear to stronger than linear increase of the hydrogen crossover flux is observed in the low to moderate current density region. Here, the hydrogen crossover flux increases by $1\,\mathrm{mmol\,s^{-1}\,m^{-2}}$ between $0.25\,\mathrm{A\,cm^{-2}}$ and $5\,\mathrm{A\,cm^{-2}}$, which is comparable to the hydrogen crossover flux of a rather highly compressed cell as examined in section 4.1.

In the high current density region above $5\,\mathrm{A\,cm^{-2}}$, a flattening of the flux is observed, which so far has been unknown. Doubling the current density from $5\,\mathrm{A\,cm^{-2}}$ to $10\,\mathrm{A\,cm^{-2}}$ only leads to an increase of the crossover flux of $0.8\,\mathrm{mmol\,s^{-1}\,m^{-2}}$.

Conclusion: One potential explanation for the impact of high current densities on hydrogen crossover is that the conventional diffusive model approach for explaining the current dependency of hydrogen crossover is insufficient at the applied operating parameters. Hence, it is reasonable that other transport mechanisms, perhaps of convective nature, become dominating in the high current regime. At least, an estimating calculation reveals that the electro-osmotically dragged amount of dissolved hydrogen is in the same order of magnitude as the experimental results.

Outlook: To validate the impact of convectively transported dissolved gas, a one-dimensional model should be set up to simulate the hydrogen crossover flux with and without the electro-osmotic drag at high current densities for various material properties. Moreover, the further investigation of the oxygen crossover at high current densities could be instructive as well. If the impact of the electro-osmotic drag on the gas transport from anode to cathode really increases with current density, it should amplify the oxygen crossover. Thus, different functional relationships between the crossover flux and the applied current density should result for oxygen and hydrogen.

Research Question 3: What is the impact of increased cathode pressures on hydrogen crossover, in addition to the cell compression and high current densities?

Summary: This question was adressed in chapter 4, additionally to the effect of cell compression and high current densities on hydrogen crossover.

Generally, it is found that higher cathode pressures result in higher hydrogen crossover fluxes. In terms of the cell compression, the findings show that the observed compression effect on hydrogen crossover is amplified with increasing cathode pressures. For the material system discussed in the context of research question 1, this means that the difference in the hydrogen crossover flux between the lowest and highest compression level at $3\,\mathrm{A\,cm^{-2}}$ increases from $0.3\,\mathrm{mmol\,s^{-1}\,m^{-2}}$ at $1\,\mathrm{bar}$ to $1.6\,\mathrm{mmol\,s^{-1}\,m^{-2}}$ at $15\,\mathrm{bar}$.

The main finding of studying hydrogen crossover at high current densities is the flattening of the hydrogen crossover flux from a stronger than linear increasing slope to an again linear increasing slope. Besides the generally higher crossover fluxes at elevated cathode pressures, the total hydrogen crossover increase over the investigated current density range from $0.25\,\mathrm{A\,cm^{-2}}$ to $10\,\mathrm{A\,cm^{-2}}$ increased from $1.78\,\mathrm{mmol\,s^{-1}\,m^{-2}}$ at $1\,\mathrm{bar}$ to $1.91\,\mathrm{mmol\,s^{-1}\,m^{-2}}$ at $10\,\mathrm{bar}$.

Conclusion: The observations from both studies can be explained by the pressure dependence of gas crossover. Generally, elevated cathode pressures lead to a higher dissolved hydrogen concentration at the cathode and thus, to a higher initial driving force for hydrogen crossover. The impact of the cell compression and high applied current density observed at ambient pressure then adds up onto the increased basic hydrogen crossover flux at higher cathode pressures.

Outlook: These findings are in line with other literature, also reporting on the cathode pressure dependence of the hydrogen crossover flux. For this reason, there is no further need for the examination of the effect of increase cathode pressures on hydrogen crossover, but the consideration remains interesting for industrial applications and should be revised regularly.

Research Question 4: How can the oxygen crossover be measured precisely by changing the cathode catalyst?

Summary: This question was the focus of chapter 5. It was investigated by analysing the oxygen in hydrogen content with five different cathode catalyst materials, while the membrane (Nafion™ 115) and the anode remained the same throughout the investigation.

The various material combinations reveal that with a platinum group metal free catalyst, more oxygen was detected in the cathode product stream than with a precious metal, such as platinum or iridium. The oxygen crossover flux with platinum, which is the most active recombination catalyst under investigation, is $0.03\,\mathrm{mmol\,s^{-1}\,m^{-2}}$ at $2\,\mathrm{A\,cm^{-2}}$. In contrast, with the least active material (Magnéli phase based on a titanium suboxide) an oxygen flux of $0.17\,\mathrm{mmol\,s^{-1}\,m^{-2}}$ was identified. However, the oxygen crossover flux at low current densities close to zero was lower than the expected minimum value. With

platinum, the measured oxygen crossover flux equals to the minimum expected flux at $1\,A\,cm^{-2}$, whereas with the Magnéli phase the value is already reached at $0.4\,A\,cm^{-2}$.

Conclusion: With regard to the investigated cathode catalysts, the findings indicate that even those catalysts exposing a low recombination activity, are still active for the recombination reaction of hydrogen and oxygen to water. Further measurements indicate that besides the catalyst, at least the carbon PTLs used on the cathode, participate in the recombination reaction as well. Both findings are consistent with the fact that the minimum expected oxygen crossover flux cannot be measured with the selected material combinations.

Outlook: With the chosen materials in this contribution, the impact of the cathode's recombination activity on the oxygen in hydrogen content is elucidated. However, the actual oxygen crossover entering the cathode compartment is most probably underestimated. For this reason, it is suggested to increase the research on recombination inactive materials, which also work for the hydrogen evolution reaction. Another approach might be to use some type of oxygen sensor or oxygen consuming material between the cathode catalyst layer and the membrane, with which the oxygen crossover flux entering the cathode compartment during electrolysis conditions can be re-calculated.

Research Question 5: What is important for the design of a recombination interlayer within the polymer electrolyte membrane?

Summary: This research question was adressed in chapter 6, by comparing the anodic hydrogen content resulting from self-sprayed CCMs with platinum interlayers at various positions in the membrane to a reference CCM without interlayer.

The analysis of the anodic gas composition reveals that the position of the recombination interlayer affects the resulting hydrogen in oxygen content, especially at enhanced cathode pressure. The closer the interlayer is positioned towards the anode, the higher is the recombination rate and hence, the lower is the hydrogen content. More precisely, it is shown that compared to the reference CCM without interlayer, the hydrogen content is cut in half with an interlayer positioned in the middle at $10\,bar$ and $1\,A\,cm^{-2}$. In contrast, with the interlayer close to the cathode, the hydrogen content is only reduced by a tenth at the same operating point. The most effective reduction to a tenth of the reference value was achieved with the interlayer close to the anode.

Conclusion: The recombination effectiveness of the interlayer close to the anode at the used operating conditions is explained with the available amount of oxygen at the interlayer. Since the oxygen concentration in the membrane decreases from anode to cathode, the recombination reaction becomes more effective, the further the interlayer is positioned towards the anode. Moreover, the recombination effectiveness is increased by elevated anode pressures, increasing the the oxygen amount in the membrane.

Outlook: More generally speaking, the findings once again prove that the integration of a recombination catalyst in the polymer electrolyte membrane helps to reduce the

anodic hydrogen content and to circumvent the formation of explosive gas mixtures. As the proper positioning of the interlayer in the membrane affects the recombination effectiveness, the particle density or the catalyst loading is expected to have an impact as well. Considering the same particle size and the same interlayer thickness, a higher loading leads to a higher platinum density and hence, to a higher surface area. In this way, more meeting points for the permeated hydrogen and oxygen are generated, which presumably should increase the recombination rate and reduce the hydrogen content even further.

Another aspect to be considered is the impact of the recombination interlayer on the material durability. Since radicals are formed during the recombination of hydrogen and oxygen, it must be investigated if recombination interlayers induce a faster material degradation.

Finally, it can be concluded that all research questions provided in this work have been studied extensively. With respect to the hydrogen crossover, further studies can be designed with the help of the revealed dependencies on important design and operating variables. The quantitative measurement of oxygen crossover remains to be challenging and needs to be revised in order to give reasonable predictions regarding the durability. Moreover, it is proven that the proper design of a platinum interlayer in the membrane makes the recombination of permeated gases quite efficient, allowing a safe operation of PEM electrolyzers equipped with thin membranes at enhanced cathode pressures. These findings and the subsequent studies contribute to characterize and to understand gas crossover, in order to further advance the PEM water electrolysis technology for hydrogen production.

References

[1] K. Ayers. The potential of proton exchange membrane–based electrolysis technology. *Curr. Opin. Electrochem.*, 18:9–15, 2019.

[2] R. Ouimet, J. R. Glenn, D. de Porcellinis, A. R. Motz, M. Carmo, and K. Ayers. The Role of Electrocatalysts in the Development of Gigawatt-Scale PEM Electrolyzers. *ACS Catal.*, 12: 6159–6171, 2022.

[3] R. Neugebauer. Der Stoff, aus dem die Zukunft ist. In R. Neugebauer, editor, *Wasserstofftechnologien*, pages 1–5. Springer Vieweg, Wiesbaden, 2022.

[4] S. Harst, B. Aßmus, A. Hackner, and A. Haslinger. In der Wasserstoffwirtschaft liegen viele Chancen. In R. Neugebauer, editor, *Wasserstofftechnologien*, pages 7–19. Springer Vieweg, Wiesbaden, 2022.

[5] M. Wietschel, E. Dütschke, M. Neuwirth, A. Scherrer, L. Zheng, N. Gerhard, S. Herkel, M. Jahn, A. Lozanovski, B. Pfluger, N. Pieton, M. Ragwitz, and F. Schnabel. Potenziale einer Wasserstoffwirtschaft aus wirtschaftlicher und gesellschaftlicher Perspektive. In R. Neugebauer, editor, *Wasserstofftechnologien*, pages 21–52. Springer Vieweg, Wiesbaden, 2022.

[6] M. Yue, H. Lambert, E. Pahon, R. Roche, S. Jemei, and D. Hissel. Hydrogen energy systems: A critical review of technologies, applications, trends and challenges. *Renew. Sustain. Energy Rev.*, 146:111180, 2021.

[7] M. Jahn, G. Herz, G. Deerberg, C. Glasner, A. Kraft, A. Menne, T. Müller, U. Seifert, E. Stahl, K. Ilse, W. Spohn, S. Schattauer, and M. Tümmler. Einsatz von Wasserstofftechnologien in der Industrie. In R. Neugebauer, editor, *Wasserstofftechnologien*, pages 83–121. Springer Vieweg, Wiesbaden, 2022.

[8] S. A. Grigoriev, V. N. Fateev, D. Bessarabov, and P. Millet. Current status, research trends, and challenges in water electrolysis science and technology. *Int. J. Hydrogen Energ.*, 45(49): 26036–26058, 2020.

[9] P. Horng, M. Kalis, and Institut für Klimaschutz, Energie und Mobilität. Wasserstoff - Farbenlehre: Rechtswissenschaftliche und rechtspolitische Kurzstudie, 2020.

[10] S. Groll (Heinrich-Böll-Stiftung). Energie für die klimaneutrale Zukunft: 15 Fakten über Wasserstoff, 2021.

[11] Bundesministerium für Wirtschaft und Energie. Die Nationale Wasserstoffstrategie, 2020.

[12] P. Schneider. Die Farben des Wasserstoffs Eine Übersicht EWE AG. URL https://www.ewe.com/de/zukunft-gestalten/wasserstoff/die-farben-des-wasserstoffs.

[13] S. Metz, T. Smolinka, C. I. Bernäcker, S. Loos, T. Rauscher, L. Röntzsch, M. Arnold, A. L. Görne, M. Jahn, G. Kolb, U.-P. Apfel, and C. Doetsch. Wasserstofferzeugung durch Elektrolyse und weitere Verfahren. In R. Neugebauer, editor, *Wasserstofftechnologien*. Springer Vieweg, Wiesbaden, 2022.

[14] Metrolregion Bremen-Oldenburg im Nordwesten e. V. Wasserstoffstrategie Metrolregion Nordwest, 2021.

[15] K. Ayers, N. Danilovic, R. Ouimet, M. Carmo, B. Pivovar, and M. Bornstein. Perspectives on Low-Temperature Electrolysis and Potential for Renewable Hydrogen at Scale. *Annu. Rev. Chem. Biomol. Eng.*, 10:219–239, 2019.

[16] M. Carmo, D. L. Fritz, J. Mergel, and D. Stolten. A comprehensive review on PEM water electrolysis. *Int. J. Hydrogen Energ.*, 38(12):4901–4934, 2013.

[17] A. Godula-Jopek and P. Millet. Outlook and Summary. In A. Godula-Jopek, editor, *Hydrogen Production*, pages 383–394. Wiley-VCH Verlag GmbH & Co. KGaA, Weinheim, 2016.

[18] K. Ayers, E. B. Anderson, C. Capuano, B. Carter, L. Dalton, G. Hanlon, J. Manco, and M. Niedzwiecki. Research Advances towards Low Cost, High Efficiency PEM Electrolysis. *ECS Trans.*, 33(1):3–15, 2010.

[19] K. Ayers, N. Danilovic, K. Harrison, and H. Xu. PEM Electrolysis, a Forerunner for Clean Hydrogen. *Electrochem. Soc. Interface*, 30:67–71, 2021.

[20] H. A. Miller, K. Bouzek, J. Hnat, S. Loos, C. I. Bernäcker, T. Weißgärber, L. Röntzsch, and J. Meier-Haack. Green hydrogen from anion exchange membrane water electrolysis: a review of recent developments in critical materials and operating conditions. *Sustain. Energ. Fuels*, 4 (5):2114–2133, 2020.

[21] I. Vincent and D. Bessarabov. Low cost hydrogen production by anion exchange membrane electrolysis: A review. *Renew. Sustain. Energy Rev.*, 81:1690–1704, 2018.

[22] U. Babic, M. Suermann, F. N. Büchi, L. Gubler, and T. J. Schmidt. Critical Review—Identifying Critical Gaps for Polymer Electrolyte Water Electrolysis Development. *J. Electrochem. Soc.*, 164(4):F387–F399, 2017.

[23] P. Trinke. *Experimental and Model-based Investigations on Gas Crossover in Polymer Electrolyte Membrane Water Electrolyzers*. PhD thesis, Leibniz University Hannover, Hannover, Germany, 2021.

[24] A. Kamaroddin, M. Fadhzir, N. Sabli, T. A. Tuan Abdullah, S. I. Siajam, L. C. Abdullah, A. Abdul Jalil, and A. Ahmad. Membrane-Based Electrolysis for Hydrogen Production: A Review. *Membranes*, 11(11), 2021.

[25] A. Goñi-Urtiaga, D. Presvytes, and K. Scott. Solid acids as electrolyte materials for proton exchange membrane (PEM) electrolysis: Review. *Int. J. Hydrogen Energ.*, 37(4):3358–3372, 2012.

[26] H. Ito. Membranes. In D. Bessarabov, editor, *PEM Electrolysis for Hydrogen Production*, pages 119–134. Taylor & Francis Group, Boca Raton, 2015.

[27] T. Sakai, H. Takenaka, and E. Torikai. Gas Diffusion in the Dried and Hydrated Nafions. *J. Electrochem. Soc.*, 133(1):88–92, 1986.

[28] T. Sakai, H. Takenaka, N. Wakabayashi, Y. Kawami, and E. Torikai. Gas Permeation Properties of Solid Polymer Electrolyte (SPE) Membranes. *J. Electrochem. Soc.*, 132(6):1328–1332, 1985.

[29] H. Ito, T. Maeda, A. Nakano, and H. Takenaka. Properties of Nafion membranes under PEM water electrolysis conditions. *Int. J. Hydrogen Energ.*, 36(17):10527–10540, 2011.

[30] P. Millet. PEM Water Electrolysis. In A. Godula-Jopek, editor, *Hydrogen Production*, pages 63–116. Wiley-VCH Verlag GmbH & Co. KGaA, Weinheim, 2016.

[31] M. Bass, A. Berman, A. Singh, O. Konovalov, and V. Freger. Surface structure of Nafion in vapor and liquid. *J. Phys. Chem. B*, 114(11):3784–3790, 2010.

[32] M. B. Satterfield and J. B. Benziger. Viscoelastic properties of Nafion at elevated temperature and humidity. *J. Polym. Sci. B Polym. Phys.*, 47(1):11–24, 2009.

[33] G. A. Ludueña, T. D. Kühne, and D. Sebastiani. Mixed Grotthuss and Vehicle Transport Mechanism in Proton Conducting Polymers from Ab initio Molecular Dynamics Simulations. *Chem. Mater.*, 23(6):1424–1429, 2011.

[34] K.-D. Kreuer. Proton Conductivity: Materials and Applications. *Chem. Mater.*, 8(3):610–641, 1996.

[35] K.-D. Kreuer. Fast proton conductivity: A phenomenon between the solid and the liquid state? *Solid State Ion.*, 94:55–62, 1997.

[36] Chemours. Nafion 115, 117, 1110: Product Bulletin P-12, 2016.

[37] Chemours. Nafion NR211 and NR212: Product Bulletin P-11, 2017.

[38] M. Carmo, W. Lueke, and D. Stolten. Electrocatalysts for the Hydrogen Evolution Reaction. In D. Bessarabov, editor, *PEM Electrolysis for Hydrogen Production*, pages 65–86. Taylor & Francis Group, Boca Raton, 2015.

[39] M. A. Khan, H. Zhao, W. Zou, Z. Chen, W. Cao, J. Fang, J. Xu, L. Zhang, and J. Zhang. Recent Progresses in Electrocatalysts for Water Electrolysis. *Electrochem. Energ. Rev.*, 1(4):483–530, 2018.

[40] F. N. Khatib, T. Wilberforce, O. Ijaodola, E. Ogungbemi, Z. El-Hassan, A. Durrant, J. Thompson, and A. G. Olabi. Material degradation of components in polymer electrolyte membrane (PEM) electrolytic cell and mitigation mechanisms: A review. *Renew. Sustain. Energy Rev.*, 111:1–14, 2019.

[41] M. Chatenet, B. G. Pollet, D. R. Dekel, F. Dionigi, J. Deseure, P. Millet, R. D. Braatz, M. Z. Bazant, M. Eikerling, I. Staffell, P. Balcombe, Y. Shao-Horn, and H. Schäfer. Water electrolysis: from textbook knowledge to the latest scientific strategies and industrial developments. *Chem. Soc. Rev.*, 2022.

[42] J. P. Hughes, J. Clipsham, H. Chavushoglu, S. J. Rowley-Neale, and C. E. Banks. Polymer electrolyte electrolysis: A review of the activity and stability of non-precious metal hydrogen evolution reaction and oxygen evolution reaction catalysts. *Renew. Sustain. Energy Rev.*, 139: 110709, 2021.

[43] M. Thomassen and S. Sunde. Electrocatalysts for Oxygen Evolution Reaction (OER). In D. Bessarabov, editor, *PEM Electrolysis for Hydrogen Production*, pages 35–64. Taylor & Francis Group, Boca Raton, 2015.

[44] M. Bernt, A. Hartig-Weiß, M. F. Tovini, H. A. El-Sayed, C. Schramm, J. Schröter, C. Gebauer, and H. A. Gasteiger. Current Challenges in Catalyst Development for PEM Water Electrolyzers. *Chem. Ing. Tech.*, 92(1-2):31–39, 2020.

[45] S. Cherevko, S. Geiger, O. Kasian, A. Mingers, and K. J. Mayrhofer. Oxygen evolution activity and stability of iridium in acidic media. Part 1. – Metallic iridium. *J. Electroanal. Chem.*, 773: 69–78, 2016.

[46] S. Cherevko, S. Geiger, O. Kasian, A. Mingers, and K. J. Mayrhofer. Oxygen evolution activity and stability of iridium in acidic media. Part 2. – Electrochemically grown hydrous iridium oxide. *J. Electroanal. Chem.*, 774:102–110, 2016.

[47] A. Lasia. Mechanism and kinetics of the hydrogen evolution reaction. *Int. J. Hydrogen Energ.*, 44(36):19484–19518, 2019.

[48] C. V. Pham, D. Escalera-López, K. Mayrhofer, S. Cherevko, and S. Thiele. Essentials of High Performance Water Electrolyzers – From Catalyst Layer Materials to Electrode Engineering. *Adv. Energy Mater.*, 11(44):2101998, 2021.

[49] S. M. Alia. Current research in low temperature proton exchange membrane-based electrolysis and a necessary shift in focus. *Curr. Opin. Chem. Eng.*, 33:100703, 2021.

[50] M. Suermann, K. Takanohashi, A. Lamibrac, T. J. Schmidt, and F. N. Büchi. Influence of Operating Conditions and Material Properties on the Mass Transport Losses of Polymer Electrolyte Water Electrolysis. *J. Electrochem. Soc.*, 164(9):F973–F980, 2017.

[51] C. C. Weber, T. Schuler, R. de Bruycker, L. Gubler, F. N. Büchi, and S. de Angelis. On the role of porous transport layer thickness in polymer electrolyte water electrolysis. *J. Power Sources Adv.*, 15:100095, 2022.

[52] T. Schuler, T. J. Schmidt, and F. N. Büchi. Polymer Electrolyte Water Electrolysis: Correlating Performance and Porous Transport Layer Structure: Part II. Electrochemical Performance Analysis. *J. Electrochem. Soc.*, 166(10):F555–F565, 2019.

[53] T. Schuler, R. de Bruycker, T. J. Schmidt, and F. N. Büchi. Polymer Electrolyte Water Electrolysis: Correlating Porous Transport Layer Structural Properties and Performance: Part I. Tomographic Analysis of Morphology and Topology. *J. Electrochem. Soc.*, 166(4):F270–F281, 2019.

[54] Z. Kang, S. M. Alia, J. L. Young, and G. Bender. Effects of various parameters of different porous transport layers in proton exchange membrane water electrolysis. *Electrochim. Acta*, 354:136641, 2020.

[55] T. Lickert, M. L. Kiermaier, K. Bromberger, J. Ghinaiya, S. Metz, A. Fallisch, and T. Smolinka. On the influence of the anodic porous transport layer on PEM electrolysis performance at high current densities. *Int. J. Hydrogen Energ.*, 45(11):6047–6058, 2020.

[56] H. Ito. Current Collectors (GDL) and Materials. In D. Bessarabov, editor, *PEM Electrolysis for Hydrogen Production*, pages 147–156. Taylor & Francis Group, Boca Raton, 2015.

[57] C. Liu, M. Carmo, G. Bender, A. Everwand, T. Lickert, J. L. Young, T. Smolinka, D. Stolten, and W. Lehnert. Performance enhancement of PEM electrolyzers through iridium-coated titanium porous transport layers. *Electrochem. Commun.*, 97:96–99, 2018.

[58] C. Liu, M. Shviro, A. S. Gago, S. F. Zaccarine, G. Bender, P. Gazdzicki, T. Morawietz, I. Biswas, M. Rasinski, A. Everwand, R. Schierholz, J. Pfeilsticker, M. Müller, P. P. Lopes, R.-A. Eichel, B. Pivovar, S. Pylypenko, K. A. Friedrich, W. Lehnert, and M. Carmo. Exploring the Interface of Skin–Layered Titanium Fibers for Electrochemical Water Splitting. *Adv. Energy Mater.*, 11 (8):2002926, 2021.

[59] S. Toghyani, E. Afshari, E. Baniasadi, and S. A. Atyabi. Thermal and electrochemical analysis of different flow field patterns in a PEM electrolyzer. *Electrochim. Acta*, 267:234–245, 2018.

[60] T. Smolinka, E. T. Ojong, and T. Lickert. Fundementals of PEM Water Electrolysis. In D. Bessarabov, editor, *PEM Electrolysis for Hydrogen Production*, pages 11–34. Taylor & Francis Group, Boca Raton, 2015.

[61] M. Maier, K. Smith, J. Dodwell, G. Hinds, P. R. Shearing, and D. Brett. Mass transport in PEM water electrolysers: A review. *Int. J. Hydrogen Energ.*, 47(1):30–56, 2022.

[62] C. Wang. Bipolar Plates and Plate Materials. In D. Bessarabov, editor, *PEM Electrolysis for Hydrogen Production*, pages 135–146. Taylor & Francis Group, Boca Raton, 2015.

[63] P. Millet. Characterization Tools for Polymer Electrolyte Membrane (PEM) Water Electrolyzers. In D. Bessarabov, editor, *PEM Electrolysis for Hydrogen Production*, pages 179–218. Taylor & Francis Group, Boca Raton, 2015.

[64] M. Suermann, T. J. Schmidt, and F. N. Büchi. Cell Performance Determining Parameters in High Pressure Water Electrolysis. *Electrochim. Acta*, 211:989–997, 2016.

[65] P. Millet. Fundamentals of Water Electrolysis. In A. Godula-Jopek, editor, *Hydrogen Production*, pages 33–62. Wiley-VCH Verlag GmbH & Co. KGaA, Weinheim, 2016.

[66] M. E. Orazem and B. Tribollet. *Electrochemical Impedance Spectroscopy*. John Wiley & Sons, Hoboken, New Jersey, 2008.

[67] A. Martin, P. Trinke, M. Stähler, A. Stähler, F. Scheepers, B. Bensmann, M. Carmo, W. Lehnert, and R. Hanke-Rauschenbach. The Effect of Cell Compression and Cathode Pressure on Hydrogen Crossover in PEM Water Electrolysis. *J. Electrochem. Soc.*, 169(1):014502, 2022.

[68] P. Trinke, G. P. Keeley, M. Carmo, B. Bensmann, and R. Hanke-Rauschenbach. Elucidating the Effect of Mass Transport Resistances on Hydrogen Crossover and Cell Performance in PEM Water Electrolyzers by Varying the Cathode Ionomer Content. *J. Electrochem. Soc.*, 166 (8):F465–F471, 2019.

[69] W. Vielstich and W. Schmickler. *Elektrochemie II: Kinetik elektrochemischer Systeme*, volume Band VI of *Grundzüge der Physikalischen Chemie*. Dr. Dietrich Steinkopff Verlag, Darmstadt, 1976.

[70] M. Bernt and H. A. Gasteiger. Influence of Ionomer Content in IrO 2 /TiO 2 Electrodes on PEM Water Electrolyzer Performance. *J. Electrochem. Soc.*, 163(11):F3179–F3189, 2016.

[71] M. Stähler, A. Stähler, F. Scheepers, M. Carmo, W. Lehnert, and D. Stolten. Impact of porous transport layer compression on hydrogen permeation in PEM water electrolysis. *Int. J. Hydrogen Energ.*, 45(7):4008–4014, 2020.

[72] C. H. Lee, R. Banerjee, F. Arbabi, J. Hinebaugh, and A. Bazylak. Porous Transport Layer Related Mass Transport Losses in Polymer Electrolyte Membrane Electrolysis: A Review. In *ASME 2016 14th International Conference on Nanochannels, Microchannels, and Minichannels*. American Society of Mechanical Engineers, 2016.

[73] S. A. Grigoriev, P. Millet, S. V. Korobtsev, V. I. Porembsky, M. Pepic, C. Etievant, C. Puyenchet, and V. N. Fateev. Hydrogen safety aspects related to high-pressure polymer electrolyte membrane water electrolysis. *Int. J. Hydrogen Energ.*, 34(14):5986–5991, 2009.

[74] S. A. Grigoriev, V. I. Porembskiy, S. V. Korobtsev, V. N. Fateev, F. Auprêtre, and P. Millet. High-pressure PEM water electrolysis and corresponding safety issues. *Int. J. Hydrogen Energ.*, 36(3):2721–2728, 2011.

[75] M. Schalenbach, M. Carmo, D. L. Fritz, J. Mergel, and D. Stolten. Pressurized PEM water electrolysis: Efficiency and gas crossover. *Int. J. Hydrogen Energ.*, 38(35):14921–14933, 2013.

[76] M. Schalenbach, T. Hoefner, P. Paciok, M. Carmo, W. Lueke, and D. Stolten. Gas Permeation through Nafion. Part 1: Measurements. *J. Phys. Chem. C*, 119(45):25145–25155, 2015.

[77] M. Chandesris, V. Médeau, N. Guillet, S. Chelghoum, D. Thoby, and F. Fouda-Onana. Membrane degradation in PEM water electrolyzer: Numerical modeling and experimental evidence of the influence of temperature and current density. *Int. J. Hydrogen Energ.*, 40(3): 1353–1366, 2015.

[78] S. H. Frensch, G. Serre, F. Fouda-Onana, H. C. Jensen, M. L. Christensen, S. S. Araya, and S. K. Kær. Impact of iron and hydrogen peroxide on membrane degradation for polymer electrolyte membrane water electrolysis: Computational and experimental investigation on fluoride emission. *J. Power Sources*, 420:54–62, 2019.

[79] P. Trinke, P. Haug, J. Brauns, B. Bensmann, R. Hanke-Rauschenbach, and T. Turek. Hydrogen Crossover in PEM and Alkaline Water Electrolysis: Mechanisms, Direct Comparison and Mitigation Strategies. *J. Electrochem. Soc.*, 165(7):F502–F513, 2018.

[80] M. Bernt, J. Schröter, M. Möckl, and H. A. Gasteiger. Analysis of Gas Permeation Phenomena in a PEM Water Electrolyzer Operated at High Pressure and High Current Density. *J. Electrochem. Soc.*, 167(12):124502, 2020.

[81] S. A. Grigoriev, A. A. Kalinnikov, P. Millet, V. I. Porembsky, and V. N. Fateev. Mathematical modeling of high-pressure PEM water electrolysis. *J. Appl. Electrochem.*, 40(5):921–932, 2010.

[82] P. Medina and M. Santarelli. Analysis of water transport in a high pressure PEM electrolyzer. *Int. J. Hydrogen Energ.*, 35(11):5173–5186, 2010.

[83] L. Haar, J. S. Gallagher, and G. S. Kell. *NBS/NRC Steam Tables*. CRC Press, 1984.

[84] M. Lindstrom and B. Wetton. A comparison of Fick and Maxwell–Stefan diffusion formulations in PEMFC gas diffusion layers. *Heat Mass Transf.*, 53(1):205–212, 2017.

[85] G. L. Standart, R. Taylor, and R. Krishna. The Maxwell-Stefan Formulation of Irreversible Thermodynamics for Simultaneous Heat and Mass Transfer. *Chem. Eng. Commun.*, 3(4-5):277–289, 1979.

[86] S. Whitaker. Derivation and Application of the Stefan-Maxwell Equations. *Rev. Mex. Ing. Quim.*, 8(3), 2009.

[87] M. Schalenbach and D. Stolten. High-pressure water electrolysis: Electrochemical mitigation of product gas crossover. *Electrochim. Acta*, 156:321–327, 2015.

[88] Z. Abdin, C. J. Webb, and E. Gray. Modelling and simulation of a proton exchange membrane (PEM) electrolyser cell. *Int. J. Hydrogen Energ.*, 40(39):13243–13257, 2015.

[89] F. Marangio, M. Santarelli, and M. Cali. Theoretical model and experimental analysis of a high pressure PEM water electrolyser for hydrogen production. *Int. J. Hydrogen Energ.*, 34(3):1143–1158, 2009.

[90] C. E. Evans, R. D. Noble, S. Nazeri-Thompson, B. Nazeri, and C. A. Koval. Role of conditioning on water uptake and hydraulic permeability of Nafion® membranes. *J. Membr. Sci.*, 279 (1-2):521–528, 2006.

[91] Q. Duan, H. Wang, and J. Benziger. Transport of liquid water through Nafion membranes. *J. Membr. Sci.*, 392-393:88–94, 2012.

[92] P. Trinke, B. Bensmann, S. Reichstein, R. Hanke-Rauschenbach, and K. Sundmacher. Hydrogen Permeation in PEM Electrolyzer Cells Operated at Asymmetric Pressure Conditions. *J. Electrochem. Soc.*, 163(11):F3164–F3170, 2016.

[93] D. Bessarabov, A. Kruger, S. M. Luopa, J. Park, A. A. Molnar, and K. A. Lewinski. Gas Crossover Mitigation in PEM Water Electrolysis: Hydrogen Crossover Benchmark Study of 3M's Ir-NSTF Based Electrolysis Catalyst-Coated Membranes. *ECS Trans.*, 75(14):1165–1173, 2016.

[94] D. S. Falcão and Pinto, A. M. F. R. A review on PEM electrolyzer modelling: Guidelines for beginners. *J. Clean. Prod.*, 261:121184, 2020.

[95] M. Schalenbach. Corrigendum to "Pressurized PEM water electrolysis: Efficiency and gas crossover" [Int J Hydrogen Energy 38 (2013) 14921–14933]. *Int. J. Hydrogen Energ.*, 41(1):729–732, 2016.

[96] F. Barbir. PEM electrolysis for production of hydrogen from renewable energy sources. *Sol. Energy*, 78(5):661–669, 2005.

[97] P. Trinke, B. Bensmann, and R. Hanke-Rauschenbach. Current density effect on hydrogen permeation in PEM water electrolyzers. *Int. J. Hydrogen Energ.*, 42(21):14355–14366, 2017.

[98] P. Trinke, B. Bensmann, and R. Hanke-Rauschenbach. Experimental evidence of increasing oxygen crossover with increasing current density during PEM water electrolysis. *Electrochem. Commun.*, 82:98–102, 2017.

[99] A. Martin, P. Trinke, C. V. Pham, M. Bühler, M. Bierling, P. K. R. Holzapfel, B. Bensmann, S. Thiele, and R. Hanke-Rauschenbach. On the Correlation between the Oxygen in Hydrogen Content and the Catalytic Activity of Cathode Catalysts in PEM Water Electrolysis. *J. Electrochem. Soc.*, 168(11):114513, 2021.

[100] K. Watanabe, K. Wakuda, K. Wani, T. Araki, K. Nagasawa, and S. Mitsushima. Existence of Dissolved Oxygen near Anode Catalyst in Proton Exchange Membrane Water Electrolyzers. *J. Electrochem. Soc.*, 169(4):044515, 2022.

[101] H. Matsushima, D. Kiuchi, and Y. Fukunaka. Measurement of dissolved hydrogen supersaturation during water electrolysis in a magnetic field. *Electrochim. Acta*, 54(24):5858–5862, 2009.

[102] H. Vogt. Mechanisms of mass transfer of dissolved gas from a gas-evolving electrode and their effect on mass transfer coefficient and concentration overpotential. *J. Appl. Electrochem.*, 19(5):713–719, 1989.

[103] Y. Tanaka, K. Kikuchi, Y. Saihara, and Z. Ogumi. Bubble visualization and electrolyte dependency of dissolving hydrogen in electrolyzed water using Solid-Polymer-Electrolyte. *Electrochim. Acta*, 50(25-26):5229–5236, 2005.

[104] S. Shibata. The Concentration of Molecular Hydrogen on the Platinum Cathode. *Bull. Chem. Soc. Jpn.*, 36(1):53–57, 1963.

[105] A. Albert, A. O. Barnett, M. Thomassen, T. J. Schmidt, and L. Gubler. Radiation-Grafted Polymer Electrolyte Membranes for Water Electrolysis Cells: Evaluation of Key Membrane Properties. *ACS Appl. Mater. Interfaces*, 7(40):22203–22212, 2015.

[106] A. Albert, T. Lochner, T. J. Schmidt, and L. Gubler. Stability and Degradation Mechanisms of Radiation-Grafted Polymer Electrolyte Membranes for Water Electrolysis. *ACS Appl. Mater. Interfaces*, 8(24):15297–15306, 2016.

[107] C. Klose, T. Saatkamp, A. Münchinger, L. Bohn, G. Titvinidze, M. Breitwieser, K.-D. Kreuer, and S. Vierrath. All–Hydrocarbon MEA for PEM Water Electrolysis Combining Low Hydrogen Crossover and High Efficiency. *Adv. Energy Mater.*, 10(14):1903995, 2020.

[108] J. Bender, B. Mayerhöfer, P. Trinke, B. Bensmann, R. Hanke-Rauschenbach, K. Krajinovic, S. Thiele, and J. Kerres. H+-Conducting Aromatic Multiblock Copolymer and Blend Membranes and Their Application in PEM Electrolysis. *Polymers*, 13(20), 2021.

[109] A. Kusoglu, A. Hexemer, R. Jiang, C. S. Gittleman, and A. Z. Weber. Effect of compression on PFSA-ionomer morphology and predicted conductivity changes. *J. Membr. Sci.*, 421-422:283–291, 2012.

[110] A. Kusoglu, M. Calabrese, and A. Z. Weber. Effect of Mechanical Compression on Chemical Degradation of Nafion Membranes. *ECS Electrochem. Lett.*, 3(5):F33–F36, 2014.

[111] B. Bensmann, R. Hanke-Rauschenbach, and K. Sundmacher. In-situ measurement of hydrogen crossover in polymer electrolyte membrane water electrolysis. *Int. J. Hydrogen Energ.*, 39(1):49–53, 2014.

[112] P. Pei, Z. Wu, Y. Li, X. Jia, D. Chen, and S. Huang. Improved methods to measure hydrogen crossover current in proton exchange membrane fuel cell. *Appl. Energy*, 215:338–347, 2018.

[113] Z. Kang, M. Pak, and G. Bender. Introducing a novel technique for measuring hydrogen crossover in membrane-based electrochemical cells. *Int. J. Hydrogen Energ.*, 46(29):15161–15167, 2021.

References

[114] A. Martin, D. Abbas, P. Trinke, T. Böhm, M. Bierling, B. Bensmann, S. Thiele, and R. Hanke-Rauschenbach. Communication—Proving the Importance of Pt-Interlayer Position in PEMWE Membranes for the Effective Reduction of the Anodic Hydrogen Content. *J. Electrochem. Soc.*, 168(9):094509, 2021.

[115] H. Janssen, J. C. Bringmann, B. Emonts, and V. Schroeder. Safety-related studies on hydrogen production in high-pressure electrolysers. *Int. J. Hydrogen Energ.*, 29(7):759–770, 2004.

[116] S. Garbe, J. Futter, A. Agarwal, M. Tarik, A. A. Mularczyk, T. J. Schmidt, and L. Gubler. Understanding Degradation Effects of Elevated Temperature Operating Conditions in Polymer Electrolyte Water Electrolyzers. *J. Electrochem. Soc.*, 168(4):044515, 2021.

[117] F. Fouda-Onana, M. Chandesris, V. Médeau, S. Chelghoum, D. Thoby, and N. Guillet. Investigation on the degradation of MEAs for PEM water electrolysers part I: Effects of testing conditions on MEA performances and membrane properties. *Int. J. Hydrogen Energ.*, 41(38):16627–16636, 2016.

[118] S. A. Grigoriev, K. A. Dzhus, D. Bessarabov, and P. Millet. Failure of PEM water electrolysis cells: Case study involving anode dissolution and membrane thinning. *Int. J. Hydrogen Energ.*, 39(35):20440–20446, 2014.

[119] Q. Feng, X.-Z. Yuan, G. Liu, B. Wei, Z. Zhang, H. Li, and H. Wang. A review of proton exchange membrane water electrolysis on degradation mechanisms and mitigation strategies. *J. Power Sources*, 366:33–55, 2017.

[120] P. Millet. Degradation Processes and Failure Mechanisms in PEM Water Electrolyzers. In D. Bessarabov, editor, *PEM Electrolysis for Hydrogen Production*, pages 219–242. Taylor & Francis Group, Boca Raton, 2015.

[121] T. Jahnke, G. Futter, A. Latz, T. Malkow, G. Papakonstantinou, G. Tsotridis, P. Schott, M. Gérard, M. Quinaud, M. Quiroga, A. A. Franco, K. Malek, F. Calle-Vallejo, R. Ferreira de Morais, T. Kerber, P. Sautet, D. Loffreda, S. Strahl, M. Serra, P. Polverino, C. Pianese, M. Mayur, W. G. Bessler, and C. Kompis. Performance and degradation of Proton Exchange Membrane Fuel Cells: State of the art in modeling from atomistic to system scale. *J. Power Sources*, 304:207–233, 2016.

[122] S. Bukola, K. Beard, C. Korzeniewski, J. M. Harris, and S. E. Creager. Single-Layer Graphene Sandwiched between Proton-Exchange Membranes for Selective Proton Transmission. *ACS Appl. Nano Mater.*, 2(2):964–974, 2019.

[123] M. Breitwieser, T. Bayer, A. Büchler, R. Zengerle, S. M. Lyth, and S. Thiele. A fully spray-coated fuel cell membrane electrode assembly using Aquivion ionomer with a graphene oxide/cerium oxide interlayer. *J. Power Sources*, 351:145–150, 2017.

[124] T. Kim, Y. Sihn, I.-H. Yoon, S. J. Yoon, K. Lee, J. H. Yang, S. So, and C. W. Park. Monolayer Hexagonal Boron Nitride Nanosheets as Proton-Conductive Gas Barriers for Polymer Electrolyte Membrane Water Electrolysis. *ACS Appl. Nano Mater.*, 4(9):9104–9112, 2021.

[125] C. Klose, P. Trinke, T. Böhm, B. Bensmann, S. Vierrath, R. Hanke-Rauschenbach, and S. Thiele. Membrane Interlayer with Pt Recombination Particles for Reduction of the Anodic Hydrogen Content in PEM Water Electrolysis. *J. Electrochem. Soc.*, 165(16):F1271–F1277, 2018.

[126] S. Garbe, E. Samulesson, T. J. Schmidt, and L. Gubler. Comparison of Pt-Doped Membranes for Gas Crossover Suppression in Polymer Electrolyte Water Electrolysis. *J. Electrochem. Soc.*, 168(10):104502, 2021.

[127] A. Stähler, M. Stähler, F. Scheepers, W. Lehnert, and M. Carmo. Scalable Implementation of Recombination Catalyst Layers to Mitigate Gas Crossover in PEM Water Electrolyzers. *J. Electrochem. Soc.*, 169(3):034522, 2022.

[128] S. Garbe, U. Babic, E. Nilsson, T. J. Schmidt, and L. Gubler. Communication—Pt-Doped Thin Membranes for Gas Crossover Suppression in Polymer Electrolyte Water Electrolysis. *J. Electrochem. Soc.*, 166(13):F873–F875, 2019.

[129] A. Martin, D. Abed El Hafez, P. Trinke, T. Böhm, B. Bensmann, S. Thiele, and R. Hanke-Rauschenbach. Ideal Positioning of a Pt-Interlayer for H2-O2-Recombination in Polymer Electrolyte Membrane Water Electrolysis. *ECS Meet. Abstr.*, MA2021-02(41):1250, 2021.

[130] J. A. Wrubel, J. Zack, A. Dizon, A. Z. Weber, A. M. Park, and G. Bender. In-Operando Measurement of Hydrogen Crossover in Proton Exchange Membrane Electrolysis Cells at Differential Pressures. *ECS Meet. Abstr.*, MA2021-02(41):1247, 2021.

Appendix A

The following sections serve as supplemental information referenced in the publication used in section 4.1 (Martin *et al.*, *J. Electrochem. Soc.* 169(1):014502, 2022). The additional figures contain the Tafel plots (fig. S1) and the cell voltage analysis for compression levels c_1 (fig. S2), c_2 (fig. S3) and c_3 (fig. S4). Moreover, the effect of compression and pressure on the energy demand for hydrogen production is evaluated.
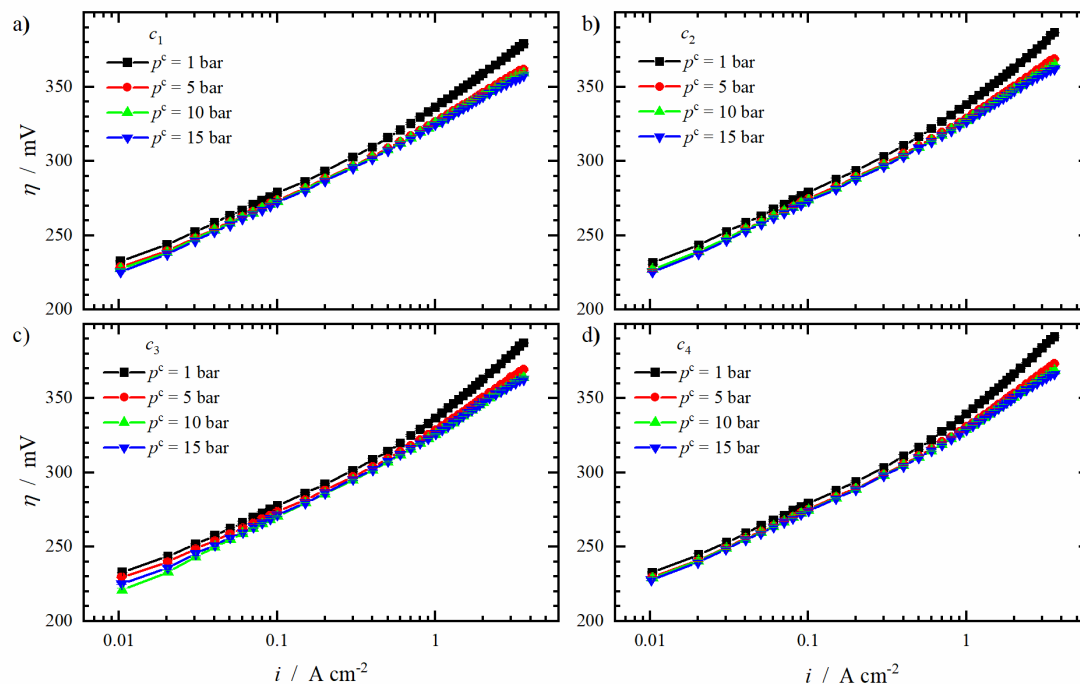
Additional Figures

Figure S1: Tafel plots of the investigated compression levels (c_1 in a), c_2 in b), c_3 in c) and c_4 in d)) at different cathode pressures.
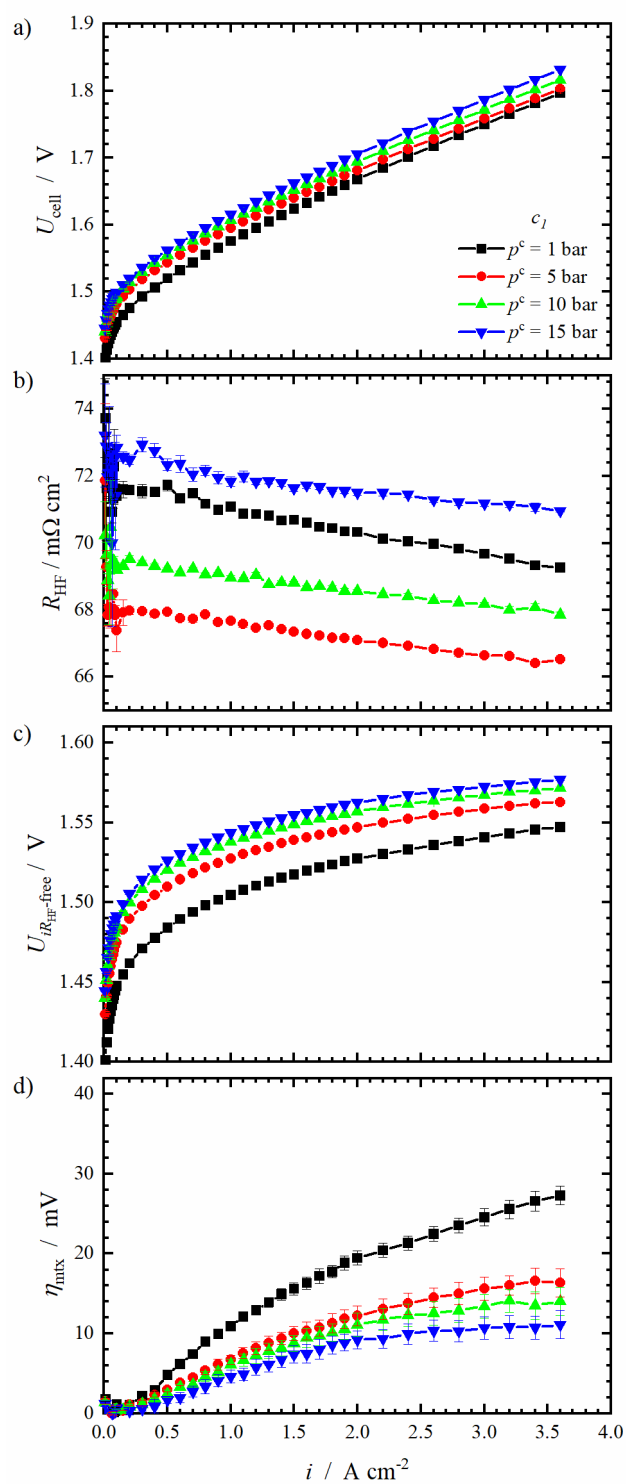
Figure S2: Deconvolution of the measured cell voltage at $p^c = 1\,\text{bar}$, $5\,\text{bar}$, $10\,\text{bar}$ and $15\,\text{bar}$ for compression level c_1. The integral cell voltage is shown in a), b) shows the respective R_{HF}, c) shows the resulting iR_{HF}-corrected cell voltages and d) shows η_{mtx}.
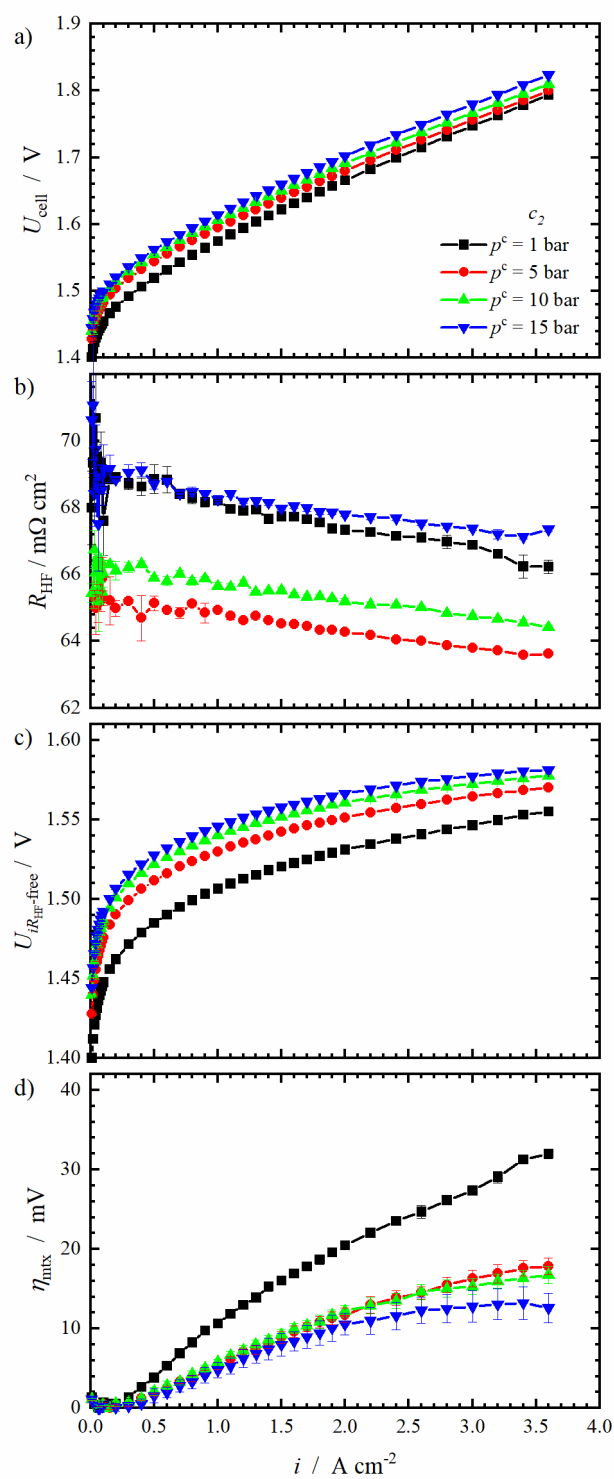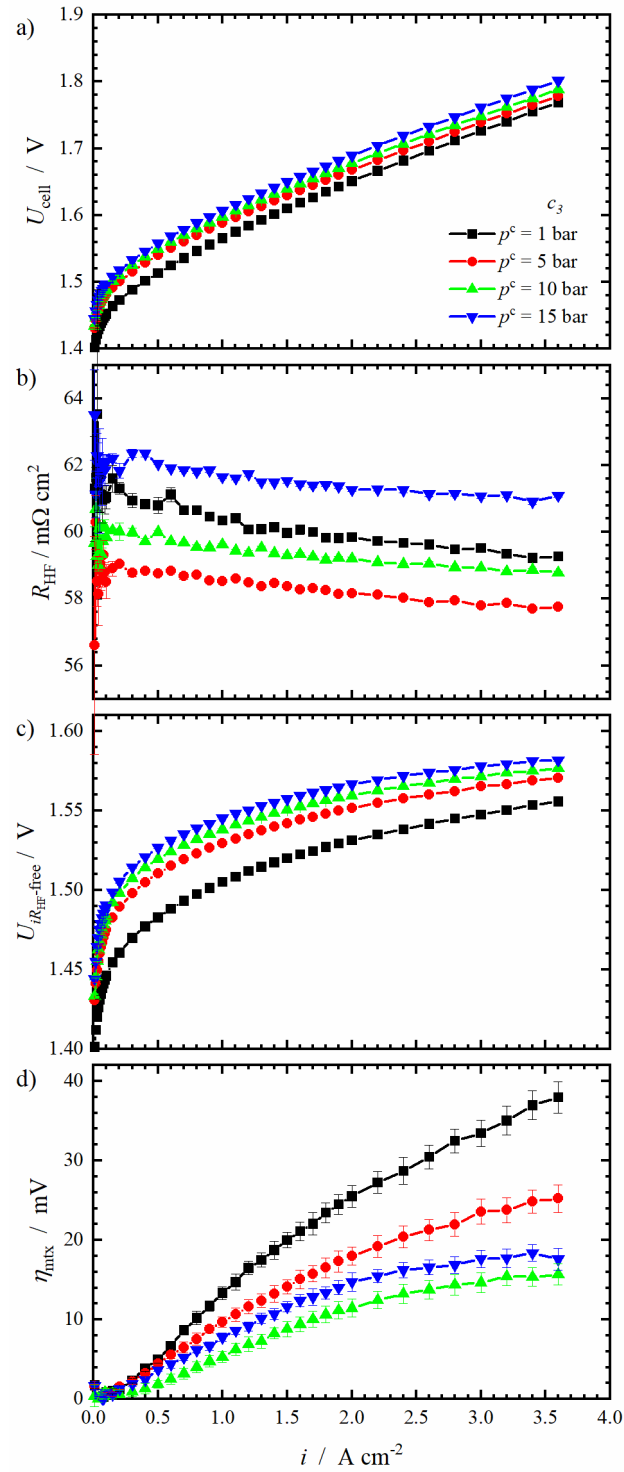
Figure S3: Deconvolution of the measured cell voltage at $p^c = 1\,\text{bar}$, $5\,\text{bar}$, $10\,\text{bar}$ and $15\,\text{bar}$ for compression level c_2. The integral cell voltage is shown in a), b) shows the respective R_{HF}, c) shows the resulting iR_{HF}-corrected cell voltages and d) shows η_{mtx}.

Figure S4: Deconvolution of the measured cell voltage at $p^c = 1\,\text{bar}$, $5\,\text{bar}$, $10\,\text{bar}$ and $15\,\text{bar}$ for compression level c_3. The integral cell voltage is shown in a), b) shows the respective R_{HF}, c) shows the resulting iR_{HF}-corrected cell voltages and d) shows η_{mtx}.

Energy Demand for Hydrogen Production

The presented study has shown the influence of cathode compression and cathode pressure on the cell voltage and on hydrogen crossover in PEM water electrolysis cells. The results reveal that high compressions lead to low cell voltages but also to increased hydrogen crossover, and that elevated pressures are increasing both, cell voltage and hydrogen crossover. This raises the question whether an optimal combination of cell compression and operating pressure exists. In order to answer this question, the overall specific energy demand for hydrogen production $w_{H_2}^{el}$ is viewed at.

For the determination of the specific energy demand $w_{H_2}^{el}$, the polarisation behaviour of an electrolysis cell and its faradaic efficiency $\eta_{faraday}$ need to be combined according to equation S1.

$$w_{H_2}^{el} = \frac{2 \cdot F \cdot U_{cell}}{\eta_{faraday}} \cdot \frac{1}{3600} \cdot \frac{1}{M_{H_2}} / \text{kWh kg}^{-1} \tag{S1}$$

Where $M_{H_2} = 2 \, \text{g mol}^{-1}$ is the molar mass of hydrogen. The faradaic efficiency $\eta_{faraday}$ is calculated by equation S2, where the remaining product gas is set in relation to the quantity evolved $\left(N_{H_2}^{evo} = \frac{i}{2 \cdot F} \right)$.

$$\eta_{faraday} = \frac{N_{H_2}^{evo} - N_{H_2}^{cross}}{N_{H_2}^{evo}} \tag{S2}$$

Particularly for the commercial usage of PEM water electrolyzerss for the generation of hydrogen, the specific energy demand is a vital parameter for a profitable system design. For the realization of high hydrogen outputs, a low voltage with the highest possible operating current is desired. In this context, the usage of thin membranes results in low ohmic voltage losses caused by the proton transport resistance through the membrane, which is a major advantage compared to thicker membranes.[1, 2, 3] The low membrane thickness is, however, also a capital disadvantage as shown in the results of this work: the hydrogen crossover increases and results in a lower faradaic efficiency especially at low current densities.[4]

For evaluation, $w_{H_2}^{el}$ should be shown against the specific hydrogen production rate G_{H_2} instead of simply using the current density. G_{H_2} is calculated by equation S3 and describes the real hydrogen output, since it takes into account that some of the produced hydrogen is lost due to crossover to the anode.

$$G_{H_2} = N_{H_2}^{evo} \cdot 3.6 \cdot 10^4 \cdot M_{H_2} \cdot \eta_{faraday} / \text{kg h}^{-1}\text{m}^{-2} \tag{S3}$$

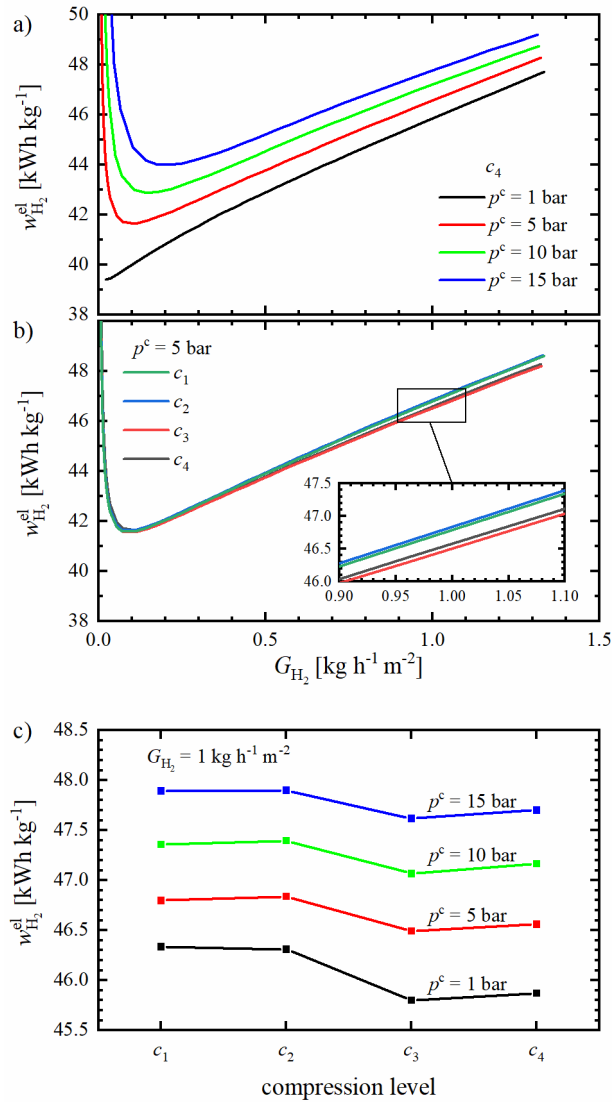**Figure S5:** Specific energy input for hydrogen generation $w_{H_2}^{el}$ for compression level c_4 at all cathode pressures in a), for all compression levels at $p^c = 5$ bar in b). In c), $w_{H_2}^{el}$ for a specific hydrogen production rate of $G_{H_2} = 1$ kg h^{-1} m^{-2} is shown. Specific energy input for hydrogen generation $w_{H_2}^{el}$ for compression level c_4 at all cathode pressures in a), for all compression levels at $p^c = 5$ bar in b). In c), $w_{H_2}^{el}$ for a specific hydrogen production rate of $G_{H_2} = 1$ kg h^{-1} m^{-2} is shown.

In fig. S5a), the specific energy demand $w_{H_2}^{el}$ is shown exemplarily for compression level c_4 for all investigated cathode pressures. The shape and order of the curves for the other compression levels are nearly identical, which is why the figure only includes one compression level. The respective figures for the other three compression levels are shown in fig. S6 for the sake of completeness. The operation at elevated cathode pressures generally yields a higher energy demand, and a minimum becomes visible. For very low amounts of hydrogen output, the specific energy demand is quite high, since a relatively large amount of produced hydrogen is lost due to crossover. With increasing cathode pressure, the minimum shifts to higher G_{H_2}. Then, the energy demand rises with the

hydrogen production rate. These trends are a result of lower η_{faraday} and higher U_{cell} when the cathode pressure is increased, and can be confirmed by literature.[5]

As already mentioned, the curve shape of $w_{\text{H}_2}^{\text{el}}$ using the investigated compression levels at each pressure are very close to one another. In order to evaluate the influence of compression, $w_{\text{H}_2}^{\text{el}}$ of all compression levels are displayed at $p^c = 5\,\text{bar}$ as an example in fig. S5b). The overlapping curves indicate that the impact of compression on $w_{\text{H}_2}^{\text{el}}$ is of minor priority for the system design. At higher hydrogen outputs, the curves diverge to some extent. The zoom within fig. S5b) shows that $w_{\text{H}_2}^{\text{el}}$ is the lowest with c_3 and the highest with c_2. The deviation in $w_{\text{H}_2}^{\text{el}}$ at $G_{\text{H}_2} = 1\,\text{kg}\,\text{h}^{-1}\,\text{m}^{-2}$ between these two compression levels is only $0.34\,\text{kW}\,\text{h}\,\text{kg}^{-1}$.

Lastly, the influence of compression and cathode pressure on the specific energy demand is compared. For this, $w_{\text{H}_2}^{\text{el}}$ at $G_{\text{H}_2} = 1\,\text{kg}\,\text{h}^{-1}\,\text{m}^{-2}$ is shown as a function of the compression level in fig. S5c). The figure summarizes the previous observation that $w_{\text{H}_2}^{\text{el}}$ rises with the applied cathode pressure at every compression level. Further, it can be seen that the deviations between the compression levels at one pressure are quite small. However, using c_3 results in the lowest $w_{\text{H}_2}^{\text{el}}$ at every investigated pressure. This is a consequence of the compression impact on the two measured variables. A higher compression leads to lower Ucell, which is favourable for the operation. But it also results in lower η_{faraday} which leads, however, to an increase of $w_{\text{H}_2}^{\text{el}}$. Since $w_{\text{H}_2}^{\text{el}}$ is a function of both values, c_3 appears to have the best trade-off between cell voltage and hydrogen crossover.

It can be summarized that the operating cathode pressure has a stronger impact on the specific energy demand of a PEM water electrolysis cell than the compression. However, the compression should not be neglected. The analysed pressure range and hydrogen output range in this work are small compared to the targeted values. When applying too high compression forces, lower faradaic efficiencies will be achieved as a result of enhanced hydrogen crossover, which must be compensated by a higher energy input. If a PEM water electrolyzers system is designed for only one particular pressure, the compression leaves room for the optimization of the specific energy demand.

To conclude, the influence of only the compression at different cathode pressures was investigated in this study. The main result is that an increase in compression leads to reduced ohmic losses but also to increased transport losses. If the latter can be reduced by e. g. better PTL design, the effect of high compression on the specific energy demand can be significantly higher.
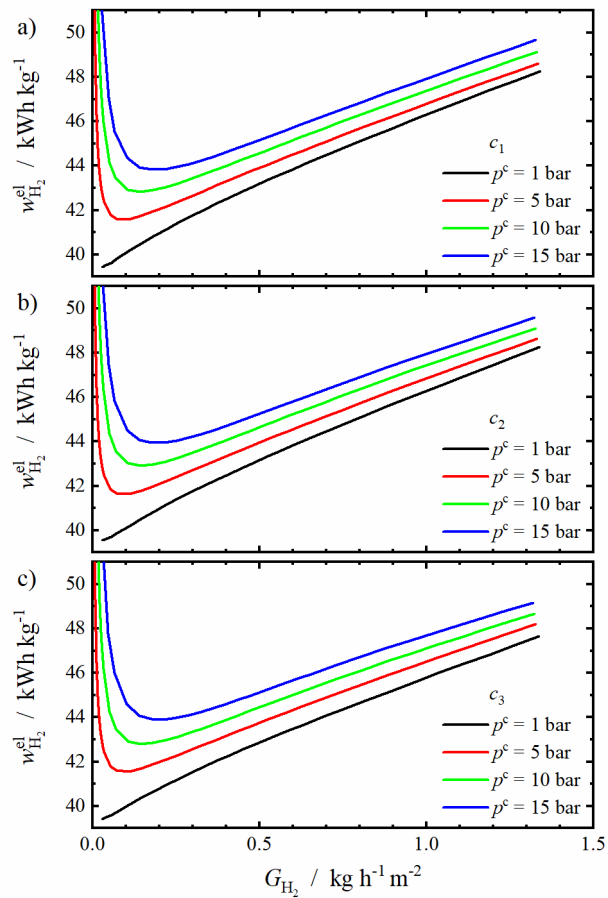
Figure S6: Specific energy demand for hydrogen generation of compression levels c_1 (a)), c_2 (b)) and c_3 (c)).

References

[1] K. E. Ayers, E. B. Anderson, C. Capuano, B. Carter, L. Dalton, G. Hanlon, J. Manco and M. Niedzwiecki, *ECS Trans.*, 33(1), 3–15, 2010.

[2] M. Bernt, J. Schröter, M. Möckl and H. A. Gasteiger, *J. Electrochem. Soc.*, 167(12), 124502, 2020.

[3] M. Carmo, D. L. Fritz, J. Mergel and D. Stolten, *Int. J. Hydrog. Energ.*, 38(12), 4901–4934, 2013.

[4] F. Scheepers, M. Stähler, A. Stähler, E. Rauls, M. Müller, M. Carmo and W. Lehnert, *Energies*, 13(3), 612, 2020.

[5] C. Mittelsteadt, T. Norman, M. Rich and J. Willey. in *Electrochemical Energy Storage for Renewable Sources and Grid Balancing,* pages 159–181, Elsevier, 2015.

Appendix B

The following SEM cross-sections of the catalyst-layers (figures S1 to S5) investigated in the publication reprinted in chapter 5 (Martin *et al.*, *J. Electrochem. Soc.* 168(11):114513, 2021) serve as supplemental information, in order to give insight into the structure of the catalyst layers of the fabricated PTEs. The imaging procedure is described in the experimental section of the manuscript.
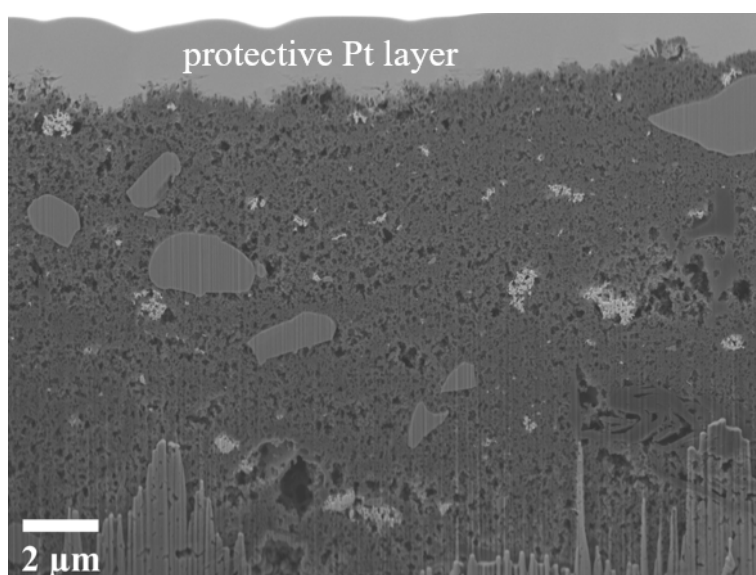

Figure S1: SEM cross-section of Magnéli phase PTE. For obtaining the cross-sectional image, a protective Pt-layer was deposited on top of the PTE-surface. In the homogeneous region of the PTE, fine Magnéli phase particles are distributed with Nafion™. Larger particles are made of Ti suboxides. The brighter spots also contain Ir.
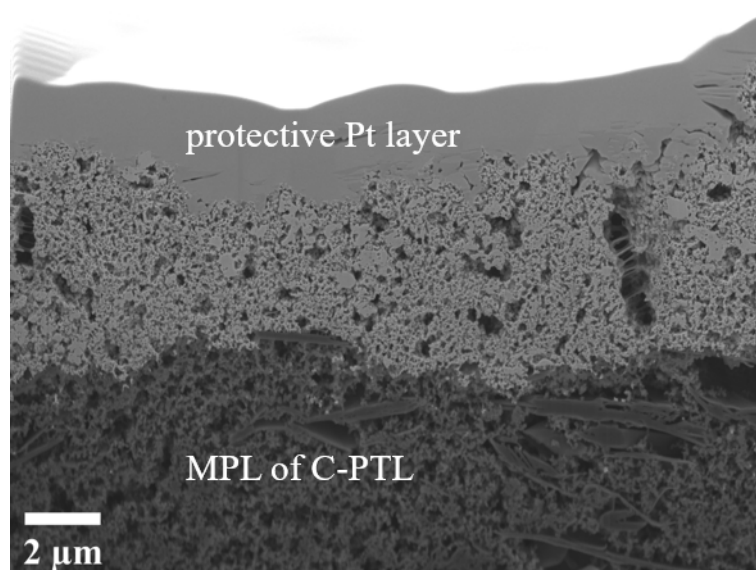
Figure S2: SEM cross-section of IrO_2 PTE. For obtaining the cross-sectional image, a protective Pt-layer was deposited on top of the PTE-surface.
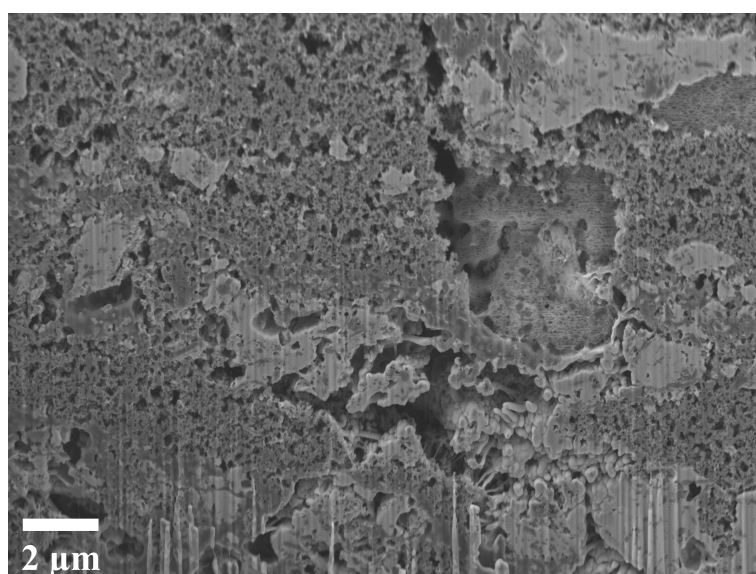

Figure S3: SEM cross-section of $[Mo_3S_{13}]^{2-}$@N-CNT PTE. Areas with low porosity consist mainly of $[Mo_3S_{13}]^{2-}$ covered CNTs. The particle clusters are made of molybdenum sulfide.
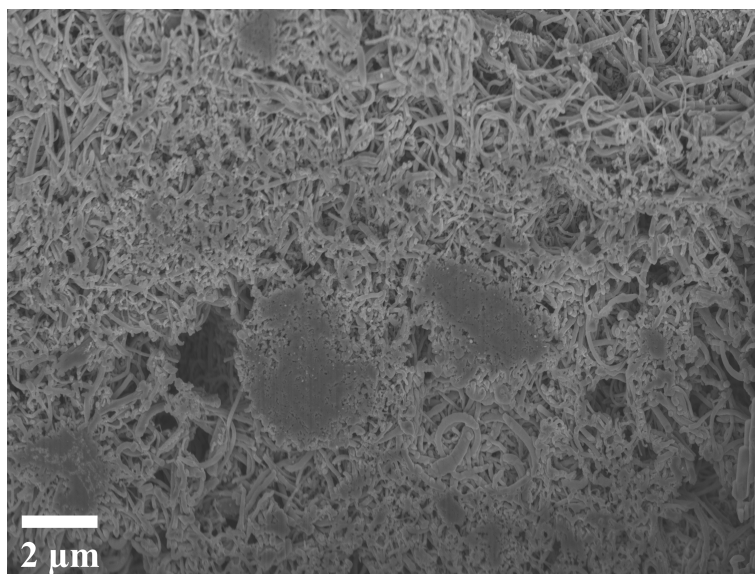
Figure S4: SEM cross-section of N-doped CNTs. The density of CNTs is quite low in some areas, which results in higher local pore volumes. The darker spots are clustered CNTs.
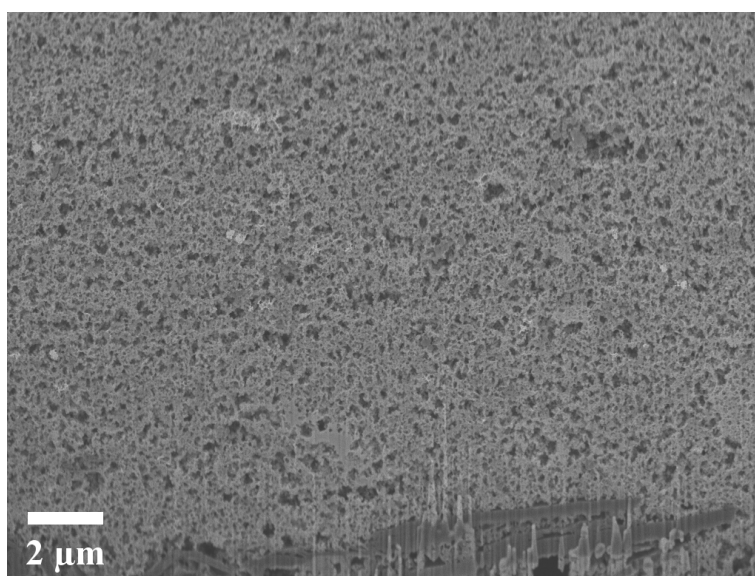

Figure S5: SEM cross-section of Pt/C PTE. The catalyst layer has a homogeneous structure.

Scientific Contributions

Peer-reviewed Journal Publications

The main author is <u>underlined</u>.

Publications used within this thesis:

- <u>A. Martin</u>, P. Trinke, B. Bensmann and R. Hanke-Rauschenbach: Hydrogen Crossover in PEM Water Electrolysis at Current Densities up to $10\,\mathrm{A\,cm^{-2}}$. *J. Electrochem. Soc.* 169(09):094507, 2022, `https://doi.org/10.1149/1945-7111/ac908c`

  The first author's contributions were to design the study, to perform the experimental measurements (polarisation behaviour and gas crossover), to analyze the data and to write the manuscript. The co-authors supported to design the study, to evaluate the data, and to review the manuscript.

- <u>A. Martin</u>, P. Trinke, M. Stähler, A. Stähler, F. Scheepers, B. Bensmann, M. Carmo, W. Lehnert and R. Hanke-Rauschenbach: The Effect of Cell Compression and Cathode Pressure on Hydrogen Crossover in PEM Water Electrolysis. *J. Electrochem. Soc.* 169(1):014502, 2022, `https://doi.org/10.1149/1945-7111/ac4459`

  The first author's contributions were to contribute to the design of study, to perform the experimental measurements (contact pressure, polarisation behaviour and gas crossover), to analyze the data and to write the manuscript. The co-authors designed the study, provided the materials, carried out the evaluation of the pressure measurement films, helped to evaluate further experimental results, provided individual paragraphs of the manuscript and reviewed the manuscript.

- <u>A. Martin</u>, P. Trinke, C. V. Pham, M. Bühler, M. Bierling, P. K. R. Holzapfel, B. Bensmann, S. Thiele and R. Hanke-Rauschenbach: On the Correlation between the Oxygen in Hydrogen Content and the Catalytic Activity of Cathode Catalysts in PEM Water Electrolysis. *J. Electrochem. Soc.* 168(11):114513, 2021, `https://doi.org/10.1149/1945-7111/ac38f6`

  The first author's contributions were to perform the full cell measurements (polarisation behaviour and gas crossover), to analyze the data and to write the manuscript. The co-authors designed the study, provided the materials, carried out the *ex situ*

analyses (half cell measurements and SEM imaging), provided individual paragraphs of the manuscript, helped during the writing process and reviewed the manuscript.

- A. Martin, D. Abbas, P. Trinke, T. Böhm, M. Bierling, B. Bensmann, S. Thiele and R. Hanke-Rauschenbach: Proving the Importance of Pt-Interlayer Position in PEMWE Membranes for the Effective Reduction of the Anodic Hydrogen Content. *J. Electrochem. Soc.* 168(9):094509, 2021, https://doi.org/10.1149/1945-7111/ac275b

  A. Martin and D. Abbas contributed equally to this work. A. Martin's contributions were to design the study, to perform the full cell experiments (polarisation behaviour and gas crossover), to analyze the data and to write the parts of the manuscript focussing on the full cell experiments. D. Abbas supported to design the study, manufactured the material and wrote the parts of the manuscript focussing on the material preparation and material characterisation. The remaining co-authors supported to design the study, carried out the *ex situ* analyses (SEM imaging), helped during the writing process and reviewed the work.

Publications and manuscripts not used within this thesis:

- D. Abbas, A. Martin, P. Trinke, M. Bierling, B. Bensmann, S. Thiele, R. Hanke-Rauschenbach and T. Böhm: Effect of Recombination Catalyst Loading in PEMWE Membranes on Anodic Hydrogen Content Reduction. Manuscript was accepted by *J. Electrochem. Soc.* on November 28, 2022, https://doi.org/10.1149/1945-7111/aca6a0

- B. Epding, A. Broda, B. Rumberg, H. Jahnke and A. Kwade: Development of Durable 3-Electrode Lithium-Ion Pouch Cells with LTO Reference Mesh: Aging and Performance Studies. *J. Electrochem. Soc.* 166(8):A1550, 2019, https://doi.org/10.1149/2.0851908jes

Oral Presentations

The presenter is underlined.

- A. Martin, P. Trinke, L. Bühre, D. Abbas, T. Böhm, B. Bensmann, S. Thiele and R. Hanke-Rauschenbach: Optimal Design of a Pt Recombination Interlayer for the Safe Hydrogen Production with PEM Water Electrolyzers, 3rd International Conference on Electrolysis (ICE 2021) 2022, Golden (CO), USA

- P. Trinke, A. Martin, D. Abbas, T. Böhm, B. Bensmann, S. Thiele and R. Hanke-Rauschenbach: Optimal Catalyst Loading of Recombination Interlayers for PEM Water Electrolysis, 18th Symposium on Modeling and Experimental Validation of Electrochemical Energy Technologies (ModVal) 2022, Hohenkammer, Germany

- A. Martin, P. Trinke, C. V. Pham, M. Bühler, M. Bierling, P. K. R. Holzapfel, B. Bensmann, S. Thiele and R. Hanke-Rauschenbach: On the Correlation between the Oxygen in Hydrogen Content and the Catalytic Activity of Cathode Catalysts in PEM Water Electrolysis, 240th ECS Meeting 2021, Orlando (FL), USA (digital) https://doi.org/10.1149/MA2021-02411248mtgabs

- A. Martin, D. Abbas, P. Trinke, T. Böhm, M. Bierling, B. Bensmann, S. Thiele and R. Hanke-Rauschenbach: Ideal Positioning of a Pt-Interlayer for H_2-O_2-Recombination in Polymer Electrolyte Membrane Water Electrolysis, 240th ECS Meeting 2021, Orlando (FL), USA (digital) https://doi.org/10.1149/MA2021-02411250mtgabs

- B. Bensmann, M. Suermann, P. Trinke, C. Immerz, A. Broda and R. Hanke-Rauschenbach: Electrolysis Cell Performance and Durability - a Contradiction in Terms?, 236th ECS Meeting 2019, Atlanta (GA), USA https://doi.org/10.1149/MA2019-02/37/1717

Poster Contributions

The presenter is underlined.

- L. Stein, H. Borg, A. Martin, P. Trinke, B. Bensmann, D. Dorfs, N. Bigall and R. Hanke-Rauschenbach: Platinum cryoaerogel catalyst layer in PEM water electrolysis cells, NanoDay 2022, Hannover, Germany

- J. Brandt, A. Martin, P. Trinke, A. Rex, L. Stein, B. Bensmann and R. Hanke-Rauschenbach: H_2-Forschung am Institut für Elektrische Energiesysteme (LUH), Workshop der Norddeutschen Themengruppe Wasserstoff 2022, Hannover, Germany

- J. Brandt, A. Martin, P. Trinke, A. Rex, L. Stein, B. Bensmann and R. Hanke-Rauschenbach: H_2-Forschung am Institut für Elektrische Energiesysteme (LUH), 3. Jahrestreffen des EFZN-Forschungsverbundes Wasserstoff Niedersachsen 2022, Goslar, Germany

- A. Martin, P. Trinke, B. Bensmann and R. Hanke-Rauschenbach: Elucidating the Effect of Electro-Osmotic Drag on H_2-Crossover at High Current Densities in PEM Water Electrolysis, 18th Symposium on Modeling and Experimental Validation of Electrochemical Energy Technologies (ModVal) 2022, Hohenkammer, Germany

Curriculum Vitæ

Personal Information

Name:	Agate Martin, née Broda
Date of Birth:	30.08.1993
Place of Birth:	Hannover, Germany

Education

08.2018 - 12.2022 **Doctoral Studies** at Institute of Electric Power Systems
Leibniz University Hannover, Germany

10.2016 - 07.2018 **Master's degree** in Material Chemistry and Nanochemistry (M. Sc.)
Leibniz University Hannover, Germany

10.2013 - 08.2016 **Bachelor's degree** in Chemistry (B. Sc.)
Leibniz University Hannover, Germany

07.2013 **International Baccalaureate Diploma**
Schillerschule, Hannover, Germany

07.2013 **Abitur**
Schillerschule, Hannover, Germany